

DARK MATTER FROM THE TOP
SIMPLIFIED MODELS OF FLAVOURED DARK MATTER
IN
DARK MINIMAL FLAVOUR VIOLATION

Zur Erlangung des akademischen Grades eines

DOKTORS DER NATURWISSENSCHAFTEN

von der Fakultät für Physik des
Karlsruher Instituts für Technologie (KIT)

genehmigte

DISSERTATION

von

M.Sc. Simon Florian Kast
aus Gengenbach

Tag der mündlichen Prüfung: 17.11.2017

Referent: Prof. Dr. Ulrich Nierste (Karlsruhe)
Korreferent: Prof. Dr. Matthias Steinhauser (Karlsruhe)
Betreuende Wissenschaftlerin: Dr. Monika Blanke (Karlsruhe)

**To my parents,
for always supporting me.**

Abstract

The mystery of dark matter is one of the biggest—if not the biggest—open questions in modern day physics. Dark matter (DM), connecting elements of particle physics and cosmology, poses a diverse, challenging and interesting field of research. In this thesis, we study the phenomenology of simplified models of flavoured dark matter (FDM) beyond Minimal Flavour Violation (MFV). For the first time, two models, coupling a dark matter flavour triplet to the Standard Model (SM) up-quark flavour triplet and to the SM left-handed quark-doublets respectively, are studied in the framework of Dark Minimal Flavour Violation (DMFV). The concept of DMFV has been introduced recently, allowing for a DM-quark coupling matrix of generic flavour structure. Hence, in this framework, the DM-quark coupling matrix constitutes a new source of both flavour and CP violation. We impose constraints from flavour experiments, the observed relic abundance, direct detection searches and new physics searches at colliders on the models, finding a rich phenomenology with an interesting interplay of effects. Among the multitude of effects, we especially want to emphasize the observed lower bound on the dark matter mass, resulting from the combined constraints. This lower bound significantly increases in light of future direct detection experiments, raising the chances to discover dark matter. This analysis hence constitutes a strong motivation for ongoing direct detection searches. Overall, we find that the combined analysis favours the scenario of top-flavoured dark matter, i.e. a DM relic which couples primarily to the SM top-quark. Furthermore, we identify areas of valid parameter space which are far different from the valid parameter space in the MFV limit. In conclusion, going beyond MFV is found to be well motivated, with DMFV as an excellent guidance.

Acknowledgements

First of all I want to thank my adviser Monika Blanke for suggesting the topic, as well as for her continuous support, advice and all the interesting discussions we had throughout my PhD. I am grateful to Uli Nierste for supervising my PhD thesis and all his input on the topic and feedback on the thesis. I also want to thank Matthias Steinhauser for agreeing to be the second examiner and his feedback on the thesis. Regarding the thesis, I am grateful to Marta Moscati, Pascal Nagel and Thomas Keck for proofreading parts of the thesis and providing me with helpful suggestions. Special thanks go to Monika Blanke for proofreading the entire thesis and providing me with invaluable feedback. In addition, I am very grateful to José Zurita, Thomas Luthe, Martin Spinrath and Robert Ziegler for the fruitful discussions regarding my research. I am also very thankful to Christoph Wiegand for his help concerning MATHEMATICA and other programs. Furthermore, I want to thank José Zurita for suggesting the title of my thesis.

I am very thankful for the nice and welcoming atmosphere created by the members of the TTP and ITP and all members of KSETA. It was a pleasure to have many fruitful discussions both at the university and at multiple workshops. I want to especially thank my friends and office mates Christoph Wiegand and Marta Moscati for all the good time and interesting discussions—about physics and many other things. Special thanks go to our TTP secretary Martina Schorn, the secretary of KSETA Barbara Lepold, the Business Manager of KSETA Irmgard Langbein and all the admins of TTP and ITP for always being friendly, helpful and providing a functioning infrastructure.

My thanks go to the LGF Baden-Württemberg and the DFG-funded Doctoral School KSETA for providing the funding for my research as well as travels to summer school, workshops and conferences. Furthermore, I acknowledge the DAAD “Kongressreisenprogramm“ funding, which supported my travels to the TeVPA 2017 conference. I want to especially thank Fady Bishara, Yuval Grossman, Wolfgang Altmannshofer and Roni Harnik for giving me the opportunity to present my research in seminar talks at their respective groups at Oxford, Cornell, Cincinnati and Fermilab. I am grateful to my supervisors for supporting me in pursuing these opportunities.

I want to thank KHYS for enabling Satrajit Das to join our group for ten weeks within the scope of the “Internship Grant“ in the summer of 2017. I want to express my special thanks to Satrajit Das for our fruitful collaboration on the quark-doublet DMFV model, which started during his internship. The internship has led to an ongoing collaboration, which will soon result in a publication.

My gratitude goes to my fellow KSETA fellow representatives Aswathi Balagopal, Nick Karcher and Radek Podskubka. I want to thank them for the successful collaboration in organizing the KSETA PhD workshop and many other things.

I am thankful to Susanne Westhoff, José Zurita and Monika Blanke, for offering me the chance to join their HEIKA research team for the upcoming months. I am looking forward to

the collaboration on the interesting topic of collider searches for dark matter in association with the Higgs boson.

A special thanks goes to my friends, colleagues and fellow boulderers Pascal Nagel, Kumar Gosh, Genessis Perez, Radek Podskubka, Will Painter, Thomas Luthe, Marta Moscati and many more for the nice time in the bouldering hall, on trips and vacations and also for the interesting discussions on physics we shared. Of course I do not want to forget to thank all the other friends who joined for many funny game nights both at the TTP and at other places.

I also want to thank all my friends from school, Bachelor, Master, PhD and elsewhere for their lasting support throughout the years and the nice times we continue to share.

I am very lucky to have a loving and patient family. I want to thank my parents, Barbara and Ralf, and my brother Johannes from the bottom of my heart for their unshakeable support throughout my entire life. Without their assistance I would never have made it this far. I owe it all to them.

I have a lot of things to be grateful for and a lot of people to be thankful to, so I want to end by thanking all those I did not mention in person.

Contents

1	Introduction	1
2	Flavour and CP Violation in the Standard Model	5
2.1	Flavour Symmetry and Yukawa Couplings in the Standard Model	5
2.2	CKM Matrix and CP Violation	7
3	Simplified Models of Flavoured Dark Matter	10
3.1	Coupling Flavoured Dark Matter to the Right-Handed Up-Quark Triplet . .	10
3.2	Coupling Matrix in Dark Minimal Flavour Violation	12
3.3	Dark Matter Stability	14
3.4	Mass Spectrum of the Dark Sector	15
3.5	Minimal Flavour Violation Limit	16
4	Constraints from Direct Searches at the LHC	18
4.1	Detection Signatures at Particle Colliders	19
4.2	Processes and Signatures of the Model	20
4.3	Constraints and Safe Parameter Space	24
4.3.1	Methodology	24
4.3.2	$t\bar{t}$ + MET Final State	25
4.3.3	Jets + MET Final State	27
4.4	Effects of Flavour Mixing Angles	30
4.5	Summary of Collider Constraints Results	31
5	Constraints from Flavour Precision Experiments	33
5.1	Contributions to Neutral Meson Mixing	33

5.2	Phenomenological Analysis	36
5.3	Remarks on Potential Effects from Rare Decays	38
5.4	Summary of Effects from Flavour Constraints	38
6	Constraint from Relic Abundance of Dark Matter	40
6.1	Measurements of Relic Abundance	40
6.2	Thermal Freeze-Out	41
6.3	Scenarios and Limits	43
6.3.1	Quasi-degenerate Freeze-Out	45
6.3.2	Single Flavour Freeze-Out	46
6.4	Remarks on Constraints from Indirect Detection	50
6.5	Summary of Effects from Relic Abundance Constraint	51
7	Constraints from Direct Detection Experiments	52
7.1	Direct Detection Experiments	52
7.2	WIMP-Nucleon Scattering	53
7.3	Phenomenology	55
7.3.1	Cancellation Pattern of Contributions	55
7.3.2	Consequences of Natural Xenon	59
7.3.3	Effects from Future Bounds	60
7.4	Summary of Effects from Direct Detection Constraint	60
8	Combined Analysis of Constraints	62
8.1	Phenomenological Analysis	62
8.1.1	Methodology	62
8.1.2	Superposition and Interference of Effects in Combined Analysis	63
8.1.3	Dark Matter Mass Bounds in Combined Analysis	65
8.2	Summary of Constraints	68
9	Coupling Flavoured Dark Matter to the Left-Handed Quark-Doublet	70
9.1	Simplified Model	70
9.2	LHC Constraints	72
9.3	Flavour Constraints	73
9.4	Relic Abundance Constraint	76

9.5	Direct Detection Constraint	78
9.6	Combined Analysis	81
9.6.1	Summary of Constraints	83
10	Conclusion and Outlook	85
A	Phenomenology of Couplings Beyond 2.0	88
B	Phenomenology of Flexible η	90
C	Constraints on Large Masses	93
	Bibliography	95

CHAPTER 1

Introduction

“There is nothing new to be discovered in physics now. All that remains is more and more precise measurement.”

*William Thomson, 1st Baron Kelvin,
In an address to an assemblage of
physicists at the British Association for
the advancement of Science (1900)*

“The most beautiful thing we can experience is the mysterious.”

*Albert Einstein, Living Philosophies
(1931)*

Fortunately, history proved Kelvin’s statement wrong, while Einstein’s remains true. In the past 117 years physicists discovered many mysterious new effects and phenomena, changing the very foundation of our physical comprehension of the world. Special and general relativity as well as quantum mechanics and quantum field theory, with their many facets and peculiarities, have redefined our understanding. Those new fundamental theories shed light on both the behaviour of elementary particles and processes on subatomic scales as well as the cosmic structures and evolution of our Universe.

Nowadays, our most trusted knowledge of the physical world is summarized in general relativity, with our established cosmological model, and the Standard Model (SM) of particle physics. General relativity constitutes our best understanding of the fundamental force of

gravity as the curvature of space-time. The Standard Model on the other hand incorporates the remaining three fundamental forces—electromagnetic, strong and weak force—described as gauge interactions in the framework of quantum field theory.

Despite the extraordinary success of the Standard Model in explaining the world with remarkable precision, physicists agree that many mysteries remain. It is commonly believed that on the most fundamental level the world should be understood by only one theory. This is in conflict with the current state of two different frameworks of general relativity and quantum field theory. A simple understanding of gravity as a quantum field theory fails due to its non-renormalizability. Yet attempts to solve these issues (e.g. string theory) might prove to be valid in the future. In addition, the neutrinos have been proven to be massive. This can only be added to the Standard Model as soon as there is sufficient evidence for either the Dirac or Majorana nature of the neutrinos.

Apart from these most obvious flaws of the Standard Model, there are also open questions such as the baryon asymmetry as well as aesthetic mysteries such as the Hierarchy problem and the strong CP problem. Further questions involve the seemingly arbitrary number of generations, the unsatisfying number of 19 fundamental parameters and their specific values as well as the number of fundamental forces. Some of these problems of fine-tuning might be solved by a many-worlds interpretation, although this comes with a foul taste for many people. Yet another class of ideas, which might reduce the number of problems, involves so-called Grand Unification. This might be achieved in some supersymmetric (SUSY) models. Such models still remain unobserved. A mutual aspect of most of the theories, which attempt to solve the remaining mysteries, is the introduction of new physics, i.e. new particles and/or new interactions. Those might not only solve some of the theoretical problems but also relax some experimental tensions with the Standard Model—namely those in flavour precision experiments. Solutions to several of the presented problems indicate that it is reasonable to expect new physics already at the electroweak scale, i.e. masses of the order of a few hundred GeV.

One of the biggest problems—and arguably the most direct hint for the existence of new physics—is the subject of this thesis: the presence of additional gravitational matter—commonly known as *dark matter*. Apparently, our best theories do not even describe 16% of the matter content of the universe. The vast majority of the gravitational matter remains (so far) unidentified [1–3]. The first hints for dark matter have been discovered as early as 1933 by Fritz Zwicky [4]. Due to large astronomical uncertainties at that time (originally Zwicky’s observations in the Coma Cluster indicated at least 400 times more dark matter than baryonic matter), the results had mostly been ignored until Vera Rubin studied rotation curves of stars in galaxies in the 1970’s [5, 6], reopening the issue.

Today we have overwhelming evidence for the existence of dark matter. Both the rotation of stars in galaxies and the movement of galaxies in galaxy clusters remain a significant hint. Attempts of explaining these observations with modifications of general relativity succeed to some degree, but ultimately fail in light of other dark matter evidence. The latter include observations of galaxy mergers, e.g. the famous bullet cluster [7], which reveal a displacement between visible matter and the bulk of gravitational matter. Furthermore the existence of dark matter can explain the enhanced structure formation in the early universe [8], since dark matter will already cluster before recombination. This characteristic

density profile also leaves imprints in the cosmic microwave background (CMB) [9], which have been observed. So far, no model of modified gravity so far has managed to reproduce the peaks in the CMB power spectrum alongside all the other experimental evidence. Hence, this multitude of effects strongly suggests the existence of new particles as dark matter [10].

Despite all the cosmological hints for particle dark matter, we still have no hard evidence for its particle-nature. The mass, the possible new interactions, as well as any other quantum numbers of the dark matter particles remain an open question. A great effort has been put into experiments for direct detection of dark matter. However, so far no new particles were detected. Another possibility to learn more about dark matter is attempting to produce it in particle collision. But so far, no evidence for new particles has been found at colliders, such as the Large Hadron Collider (LHC) at CERN. Experimentalists will keep up the effort and further improve the limits, hopefully discovering dark matter eventually.

What can theorists do in the matter of dark matter? The null-result of collider and direct detection experiments as well as the cosmological observation of the relic abundance of dark matter can all be translated into constraints on possible dark matter models. Theorists can study the phenomenology of such dark matter models and test their validity in light of those constraints to get new ideas and motivations. One possibility to find dark matter models worth studying is to motivate extensions beyond the Standard Model (BSM) by trying to solve one or many of the aforementioned problems and produce a dark matter candidate along the way. The lightest supersymmetric particle (LSP) in SUSY models or the axion (the quantum of the axion field, which was introduced to solve the strong CP problem) are prominent examples of this approach. An alternative approach is studying possible dark matter interactions with the SM particles in an effective field theory (EFT) framework. In this approach possible new mediators are integrated out and constraints on the scale of the effective operators are studied to gain information on a large class of models.

One problem with models such as those motivated by SUSY is the large number of parameters. This makes them hard to study in an efficient way. EFT models on the other hand may not always be valid (depending on the energies and masses involved) and hence might result in a flawed estimate of the phenomenology. An increasingly popular alternative are so-called *simplified models*. In contrast to the EFT approach, the mediators are not integrated out in the simplified model. Quite to the contrary, fully renormalizable interactions are studied while simultaneously keeping the number of involved parameters reasonably small.

There is a large variety of possibilities to motivate a simplified model. The one we want to mention here is *flavoured dark matter* (FDM) [11–30], on which this thesis focuses. In an analogy to the Standard Model matter content, it is assumed that dark matter also comes in different generations—also known as flavours. Apart from this elegant analogy, such flavour symmetries can also provide a natural stabilization mechanism for the dark matter candidate [15, 25]. FDM is not only an intriguing theoretical consideration, but arises in a natural way in all Grand Unified Theories (GUT), if dark matter and normal matter are unified in one multiplet.

In addition to the previously mentioned measurements, we also need to consider bounds from flavour precision experiments for such generic models. FDM models, coupling a dark

flavour triplet to the quark or lepton sector, have been studied for a number of years. Most of the studies were restricted by imposing the principle of *Minimal Flavour Violation* (MFV) [31–33]. In this framework the possible interactions are strongly restricted by demanding the SM Yukawa couplings to be the only source of flavour and CP violation. This leads to a simple (compared to the general case) structure of the allowed new physics interactions. Only very recently, there have been attempts to study models in a more general framework beyond the MFV approach [25, 34]. In this thesis we present the research which we did on some of these more general models. For the first time, we studied a model coupling flavoured dark matter to the right-handed up-quark triplet with a generic coupling matrix, resulting in a rich and interesting phenomenology. This constitutes the main subject of the thesis. In addition, we studied a model coupling the dark triplet to the left-handed SU(2) quark doublet, also with a generic coupling matrix. The phenomenology of this model shows an interesting combination of the phenomenology of the up-quark model and the previously studied down-quark model [25].

The rest of this thesis is structured as follows. In Chapter 2 we will give a short review of the Standard Model of particle physics. It includes a discussion of the fundamental flavour structures, the origin of flavour and CP-violating effects in the Standard Model and hence the Cabibbo-Kobayashi-Maskawa (CKM) matrix. Next, in Chapter 3 we discuss the simplified model of flavoured dark matter coupling to the SM up-quark triplet, which we studied. The crucial properties and the concept of *Dark Minimal Flavour Violation* (DMFV) are introduced. The parametrization of the generic coupling and the complete list of parameters is presented. Equipped with the fundamental ideas the following chapters focus on the phenomenology of the model in light of the different constraints. Each chapter follows the same substructure. First the idea of the constraining method and experimental bounds are discussed. Then, we continue by applying the bounds on the up-quark DMFV model in detail. Chapter 4 presents the bounds from collider searches at the LHC, which are used to define a safe parameter space for the further analysis. Flavour constraints are discussed in Chapter 5, the constraint from the observed relic abundance of dark matter is discussed in Chapter 6 and last but not least in Chapter 7 effects of direct detection limits are studied. Ultimately, we present a combined analysis of all previous constraints in Chapter 8. The superposition and more importantly the non-trivial interplay of the different bounds is analyzed. We want to emphasize at this points that the combined analysis is absolutely crucial to understand the true constraints on dark matter models. We present the most intriguing effect discovered in this research, originating from an interplay between the relic abundance constraint and direct detection bounds from experiments with natural xenon. Chapter 9 will then briefly discuss the variations in structure and phenomenology of the quark-doublet DMFV model in contrast to the up-quark DMFV model. Finally we recap the most important results and predicted future bounds from upcoming experiments in Chapter 10. The Appendix discusses some more subtle effects, special cases and parameter limits to complement the analysis. The research on the up-quark DMFV model has been published in [35]. The quark-doublet DMFV model research will be published in [36].

Flavour and CP Violation in the Standard Model

For the sake of brevity, we do not intend to give a complete introduction to the Standard Model (SM) of particle physics. We merely give a review of those aspects of the SM flavour sector which are essential for the understanding of this thesis. For this purpose, we first discuss the flavour symmetry structure of the SM. We then continue to derive the single source of flavour and CP violation in the SM—the Yukawa matrices which lead to the existence of the Cabibbo-Kobayashi-Maskawa (CKM) matrix. We remark that the Pontecorvo-Maki-Nakagawa-Sakata (PMNS) matrix is present only in case of massive neutrinos and therefore is not part of the SM. The interplay of weak interactions and Yukawa couplings which results in the unavoidable existence of CP-violating effects is discussed.

2.1 Flavour Symmetry and Yukawa Couplings in the Standard Model

All matter particles in the Standard Model exist in groups of three—referred to as triplets. The members of these triplets only differ from each other in their respective masses, they are commonly referred to as generations or flavours. In absence of the mass terms, the flavours can not be distinguished from each other. Hence, transforming them into one another—by multiplying the flavour triplet with a 3×3 unitary matrix—will leave the Lagrangian, i.e. the physics, unaffected. In the absence of mass terms, the SM Lagrangian incorporates an $U(3)^5$ flavour symmetry. The right-handed electron triplet, the right-handed up-quark triplet and the right-handed down-quark triplet can be transformed independently under their respective flavour symmetries $U(3)_e$, $U(3)_u$ and $U(3)_d$, leaving the Lagrangian invariant. The left-handed down-quark flavour triplet and left-handed up-quark flavour triplet are part of an electroweak $SU(2)_{EW}$ doublet $q_L = (u_L, d_L)^T$ and hence need to transform under the same flavour symmetry $U(3)_q$ to leave the Lagrangian invariant. This is apparent in

the coupling to the W-boson

$$\mathcal{L}_W = \frac{g_W}{\sqrt{2}} \sum_{i=1}^3 \left(\bar{u}_{Li} \gamma^\mu d_{Li} W_\mu^+ + \bar{d}_{Li} \gamma^\mu u_{Li} W_\mu^- \right). \quad (2.1)$$

Here g_W is the weak coupling constant. We can see that the transformation

$$u_L \rightarrow V_{uL} u_L, \quad d_L \rightarrow V_{dL} d_L, \quad (2.2)$$

with two different 3×3 unitary matrices V_{uL} and V_{dL} results in

$$\mathcal{L}_W \rightarrow \frac{g_W}{\sqrt{2}} \sum_{i,j,k=1}^3 \left(\bar{u}_{Li} \gamma^\mu (V_{uL}^\dagger)_{ij} (V_{dL})_{jk} d_{Lk} W_\mu^+ + \bar{d}_{Li} \gamma^\mu (V_{dL}^\dagger)_{jk} (V_{uL})_{ki} u_{Lk} W_\mu^- \right). \quad (2.3)$$

Hence we need to require $V_{uL} \equiv V_{dL} \equiv V_q$ to find the Lagrangian invariant. The same is true analogously for the left-handed electron flavour triplet and the left-handed neutrino flavour triplet, which are also part of an electroweak $SU(2)_{EW}$ doublet. Since the SM does not incorporate right-handed neutrinos, in summary we find a $U(3)^5$ flavour symmetry.

Nevertheless, the SM actually does contain mass terms, which hence result in a breaking of this flavour symmetry. The mass terms of the SM originate in the Yukawa interactions with the Higgs doublet. In the following discussion we focus on the quark sector. The discussion can be carried out analogously in the lepton sector. The Yukawa interactions in the quark sector are

$$\mathcal{L}_Y = -(Y_u)_{ij} \bar{q}_{Li} \tilde{H} u_{Rj} - (Y_d)_{ij} \bar{q}_{Li} H d_{Rj} + h.c. \quad (2.4)$$

with the Yukawa couplings Y_u and Y_d . After electroweak symmetry breaking, the Higgs field acquires a vacuum expectation value (VEV) $H = \frac{1}{\sqrt{2}}(0, v)^\top$, resulting in the mass terms

$$\begin{aligned} \mathcal{L}_Y &= -\frac{v}{\sqrt{2}} (Y_u)_{ij} \bar{u}_{Li} u_{Rj} - \frac{v}{\sqrt{2}} (Y_d)_{ij} \bar{d}_{Li} d_{Rj} + h.c. \\ &= -(M_u)_{ij} \bar{u}_{Li} u_{Rj} - (M_d)_{ij} \bar{d}_{Li} d_{Rj} + h.c. \end{aligned} \quad (2.5)$$

In the last steps we defined the up-quark mass matrix $(M_u)_{ij}$ and the down-quark mass matrix $(M_d)_{ij}$. In a generic theory, we should not expect the Yukawa couplings and hence the mass terms to have any specific structure, they can be arbitrary 3×3 complex matrices.

The physical particles are the mass eigenstates. Hence to find the physical quark states, we need to diagonalize the mass matrices, hence the Yukawa couplings. Using their singular value decomposition we can rewrite

$$M_u = V_{uL}^\dagger m_u V_{uR}, \quad M_d = V_{dL}^\dagger m_d V_{dR} \quad (2.6)$$

with m_u and m_d being real diagonal mass matrices with positive entries and V_{uL} , V_{uR} , V_{dL} and V_{dR} all being 3×3 unitary matrices. This way we can see that the re-definitions

$$u_L \rightarrow V_{uL} u_L, \quad d_L \rightarrow V_{dL} d_L, \quad u_R \rightarrow V_{uR} u_R, \quad d_R \rightarrow V_{dR} d_R \quad (2.7)$$

lead to mass terms with diagonal (and positive) mass matrices, i.e. we have identified the physical quark states. As we have already discussed, the transformation (2.7) will leave a residual in the weak interaction, since the simultaneous diagonalization of up-quark mass matrix and down-quark mass matrix generically demands the left-handed up-quark triplet and left-handed down-quark triplet to transform differently. We find

$$\mathcal{L}_W = \frac{g_W}{\sqrt{2}} \sum_{i,k=1}^3 \left((V_{\text{CKM}})_{ik} \bar{u}_{Li} \gamma^\mu d_{Lk} W_\mu^+ + (V_{\text{CKM}}^\dagger)_{ik} \bar{d}_{Li} \gamma^\mu u_{Lk} W_\mu^- \right). \quad (2.8)$$

where we have defined the Cabibbo-Kobayashi-Maskawa (CKM) matrix

$$V_{\text{CKM}} = (V_{uL}^\dagger)(V_{dL}). \quad (2.9)$$

The CKM-matrix originates in the Yukawa interaction, more precisely in the misalignment of the Yukawa couplings Y_u and Y_d , which demands $V_u \neq V_d$. In the weak interaction terms this results in a physical observable—the CKM-matrix. In the following section we discuss the properties of the CKM-matrix and some of the implications of its existence.

2.2 CKM Matrix and CP Violation

Since V_{uL} and V_{dL} are 3×3 unitary matrices, $V_{\text{CKM}} = (V_{uL}^\dagger)(V_{dL})$ is also a 3×3 unitary matrix. Hence it generically contains 3 real parameters and 6 complex phases. But not all of these are physical observables. So far, we did not fully exhaust all available symmetries. It is still possible to re-define all quark flavours up to a phase, i.e.

$$u_{Lj} \rightarrow e^{i\alpha_j} u_{Lj}, \quad d_{Lj} \rightarrow e^{i\beta_j} d_{Lj} \quad (2.10)$$

This provides us with 5 phase-differences, which can be used to eliminate 5 of the 6 phases in the CKM-matrix. We are left with one physical phase which can not be absorbed into re-definitions. This phase is a source of CP violation. The CP transformation applied on the weak interaction term results in

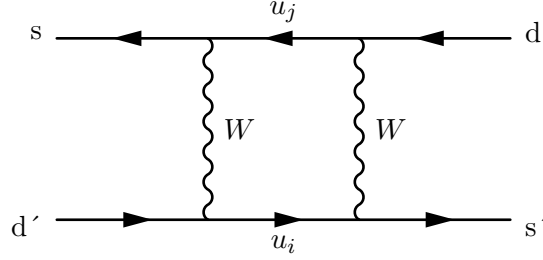


Figure 2.1: Feynman diagram of leading order SM process in neutral Kaon mixing.

$$\begin{aligned}
& (V_{\text{CKM}})_{ij} \bar{u}_{Li} \gamma^\mu d_{Lj} W_\mu^+ + (V_{\text{CKM}}^\dagger)_{ij} \bar{d}_{Li} \gamma^\mu u_{Lj} W_\mu^- \quad (2.11) \\
\rightarrow & (V_{\text{CKM}})_{ij} \bar{d}_{Lj} \gamma^\mu u_{Li} W_\mu^- + (V_{\text{CKM}}^\dagger)_{ij} \bar{u}_{Lj} \gamma^\mu d_{Li} W_\mu^+ \\
= & (V_{\text{CKM}}^*)_{ij} \bar{u}_{Li} \gamma^\mu d_{Lj} W_\mu^+ + (V_{\text{CKM}}^\top)_{ij} \bar{d}_{Li} \gamma^\mu u_{Lj} W_\mu^-.
\end{aligned}$$

Because of the physical phase, we have $V_{\text{CKM}} \neq V_{\text{CKM}}^*$ and hence find that CP does not leave the weak interaction Lagrangian invariant, i.e. it is no longer a symmetry. Hence we conclude that the misalignment of flavour and mass eigenstates, originated in the generic Yukawa couplings, leads us to expect CP violation in the weak interaction of the SM.

CP violation was first discovered in the decays of neutral Kaons in 1964 [37]. Although this should come as no surprise after the discussion above, it did at that time. In 1964, only 2 generations of quarks were discovered yet. With only two quark generations, no CP-violating complex phase is predicted, since the phase re-definitions are enough to eliminate all complex phases in a 2×2 unitary matrix. Historically the discovery of CP violation led Kobayashi and Maskawa to predict the third generation of quarks, since this results in an unavoidable CP-violating phase [38]. For this work they were ultimately awarded the Nobel price in 2008.

A compact review of CP violation in the quark-sector can be found in [39]. We focus on a rough sketch of those aspects most relevant for this work, i.e. neutral meson mixing. As an exemplary case, we study the $K^0 - \bar{K}^0$ mixing in more detail. The Feynman diagram of the LO SM contribution to $K^0 - \bar{K}^0$ mixing is given in Figure 2.1. Due to the off-diagonal terms in V_{CKM} , the weak interaction, or more precisely the W-boson coupling, allows for flavour changing neutral currents (FCNC). Since those effects arise at the loop-level, they are strongly suppressed in the SM. This suppression is known as Glashow-Iliopoulos-Maiani (GIM) mechanism [40].

The contribution in Figure 2.1 can be seen as an off-diagonal element of the effective Hamiltonian describing the two-state system of K^0 and \bar{K}^0 :

$$i \frac{\partial}{\partial t} \begin{pmatrix} K^0(t) \\ \bar{K}^0(t) \end{pmatrix} = \mathcal{H}^K \begin{pmatrix} K^0(t) \\ \bar{K}^0(t) \end{pmatrix}. \quad (2.12)$$

To find the physical states, we need to diagonalize this Hamiltonian. The misalignment of

mass- and flavour-eigenstates results of an oscillation of the states, which can be measured in flavour experiments. The details of the measurement strategies differ for different mesons, depending on the specifics of the involved CKM-elements. Details can be found in [41]. Flavour experiments are a remarkable option to probe physics at large mass scales. The particles do not have to be created on-shell, but the experiments are sensitive to heavy NP in the loop-corrections.

Today CP violation has also been discovered in $B_d^0 - \bar{B}_d^0$ mixing [42]. Bounds for CP violation in $B_s^0 - \bar{B}_s^0$ mixing and $D^0 - \bar{D}^0$ mixing exist, but so far they are still in agreement with no CP violation [42]. Compared to the generic case, the observed CP violation is unexpectedly small. Furthermore, the CKM matrix is surprisingly close to the unit matrix, which indicates an unexpected alignment of the Yukawa couplings of the up-sector Y_u and down-sector Y_d . In the SM, such an alignment is unexpected. This has led physicists to explore the possibility of extended theories. In such theories the Yukawas are considered to be originated from dynamical degrees of freedom, known as flavon fields. After electroweak symmetry breaking, those fields acquire VEVs, which are the Yukawa coupling matrices in the SM. Such an understanding of Yukawas as VEVs of fields in a larger theory can be used to motivate a connection of Y_u and Y_d . If the Yukawa couplings are assigned transformation properties as if they were fields, they are referred to as spurions.

The remarkable agreement of experimental data and SM predictions puts strong bounds on possible extensions of the SM. A common approach to acquire small FCNCs and CP-violating effects in BSM theories is demanding the Yukawa couplings Y_u and Y_d to remain the only sources of flavour and CP violation in the extended theory. Such a requirement constrains the structure of all NP couplings in the larger theory, leading to SM-like predictions. This procedure is commonly known as Minimal Flavour Violation (MFV). In this thesis we will explore models going beyond the limitations of MFV.

Simplified Models of Flavoured Dark Matter

In this chapter, we discuss the details of the studied simplified models. After presenting the motivation for couplings, quantum numbers and transformation properties, we especially address the main idea of Dark Minimal Flavour Violation (DMFV). This framework was first introduced in [25], whose primary concepts we follow closely. We then move on to discuss the flavour structure of the extended theory as well as the parametrization of the coupling matrix and its parameter space. We also have a look at the issue of dark matter decay, repeating the basic proof for dark matter stability in such models. Furthermore, we discuss implications of this chosen framework in the mass-splitting in the dark sector. To conclude the chapter, we address limits to recover the more basic and simpler framework of Minimal Flavour Violation (MFV), building a bridge to more established studies. Understanding this limit suits to stress differences and advantages of this novel and more general approach.

3.1 Coupling Flavoured Dark Matter to the Right-Handed Up-Quark Triplet

The basic motivation for models such as the proposed one is a simple analogy to the Standard Model (SM). All matter particles known to us are arranged in groups of three, with the group members only differing in their mass, see Chapter 2. The three members of these groups are referred to as generations or flavours. Furthermore, we observe that all the SM matter content consists of Dirac fermions—with Majorana neutrinos as a possible exception. Hence, for our model we consider a simple but appealing extension of the Standard Model, a flavour triplet of Dirac fermions in the dark sector.

Still, a multitude of possible interactions with the SM remain. In the past, a number of models coupling to SM matter in different ways has been studied. To keep the model

reasonably simple, most of the studies focus on the interaction with one particular SM particle, or as an alternative one sector of the SM particle content. In the case of flavoured dark matter (FDM) an obvious class of models couples the dark triplet to a SM flavour triplet. Models coupling the dark sector to quark triplets as well as models coupling to the lepton triplets have been studied to some extent [11–30].

In [25] a model coupling to the SM right-handed down-quark flavour triplet has been studied, going for the first time beyond Minimal Flavour Violation (MFV). Following this idea, the authors introduced the framework of Dark Minimal Flavour Violation (DMFV). This concept will be introduced below in more detail. The subject of this thesis is the extension of our knowledge about DMFV models. A straightforward next step is to consider a model coupling the dark triplet to the SM right-handed up-quark flavour triplet in an analogous way.

The primary new physics (NP) interaction in such a model, coupling the dark sector flavour triplet to the SM is chosen as follows:

$$\mathcal{L}_{\text{int}} = -(\lambda_{ij} \bar{u}_{Ri} \chi_j \phi + h.c.). \quad (3.1)$$

In this formula u_{Ri} labels the SM right-handed up-quark triplet with (i, j) being generational indices. λ_{ij} is the NP DM-quark coupling matrix, which is discussed in more detail in Section 3.2. The members of the dark matter (DM) triplet $\chi_j = (\chi_u, \chi_c, \chi_t)^\top$ are chosen to be Dirac fermions, as discussed before. To ensure a truly “dark” matter (DM) with respect to the SM interactions, we choose χ to be a SM gauge singlet. The members of the triplet are labelled by the quark flavour, which they dominantly couple to. Finally, we introduce ϕ as a new scalar mediator, ensuring a renormalizable dimension-four interaction. The mediator carries both QCD colour and hypercharge of the up-quark triplet, ensuring a gauge invariant interaction term.

The DM triplet is chosen to transform in the fundamental representation of a new flavour symmetry $U(3)_\chi$. Summarizing the global quark flavour symmetry in our model, we have

$$U(3)_q \times U(3)_u \times U(3)_d \times U(3)_\chi. \quad (3.2)$$

From the interaction (3.1) it is apparent that λ (spurion) transforms as an $(1_q, 3_u, 1_d, \bar{3}_\chi)$ under this flavour symmetries, i.e.

$$\lambda \rightarrow V_u \lambda V_\chi^\dagger. \quad (3.3)$$

The flavour symmetry of the SM is only broken by the SM Yukawa couplings Y_u and Y_d . In the framework of Minimal Flavour Violation (MFV), it is assumed that those remain the only sources of flavour violation for the entire global flavour symmetry. As a consequence, the structure of the NP coupling matrix λ is severely restricted, see Section 3.5. Many FDM models have been studied under this assumption.

In this work we follow the more general approach of Dark Minimal Flavour Violation

(DMFV), introduced in [25]. In this novel framework we include the NP DM-quark coupling matrix λ as the only new source of flavour violation. The coupling matrix λ is left general, see Section 3.2. Hence, we get a more complicated but also more interesting phenomenology, going beyond the established research for FDM coupling to the SM up-quark triplet.

Since the DM triplet is a gauge singlet, we do not need any complicated structures like a new Higgs sector. Hence, to keep the model simple, we introduce the masses of the new particles in the most straightforward way:

$$\mathcal{L}_{\text{mass}} = -m_{\chi,ij}\bar{\chi}_i\chi_j - m_\phi^2\phi^\dagger\phi. \quad (3.4)$$

To ensure our choice of Dirac fermion dark matter, we impose $m_\phi > m_\chi$. If this requirement were violated, the model would predict a stable scalar, carrying QCD colour and electric charge, which is strictly excluded by data. In Section 3.3 we shall see in more detail that this choice ensures a stable dark matter candidate for our model. Please also note that we choose the same mass for all flavours in the dark sector. This is a direct consequence of demanding DMFV. Nevertheless, renormalization group (RG) running effects unavoidably introduce a mass-splitting, as discussed in Section 3.4.

The most general renormalizable Lagrangian including the minimal field content is hence given as

$$\begin{aligned} \mathcal{L} = & \mathcal{L}_{\text{SM}} + i\bar{\chi}\not{\partial}\chi - m_{\chi,ij}\bar{\chi}_i\chi_j - (\lambda_{ij}\bar{u}_{Ri}\chi_j\phi + h.c.) \\ & + (D_\mu\phi)^\dagger(D^\mu\phi) - m_\phi^2\phi^\dagger\phi + \lambda_{H\phi}\phi^\dagger\phi H^\dagger H + \lambda_{\phi\phi}(\phi^\dagger\phi)^2. \end{aligned} \quad (3.5)$$

The couplings of the mediator to the SM Higgs H as well as the four mediator interaction are given for completeness but prove to be insignificant for this study. The complete list of symmetry transformation properties of all relevant particles is summarized in Table 3.1. In addition to the particles, we also list the SM Yukawa spurion fields Y_u and Y_d as well as the NP coupling matrix λ .

3.2 Coupling Matrix in Dark Minimal Flavour Violation

We now have a closer look at the NP DM-quark coupling matrix λ . Following the assumption of DMFV, λ starts off as a completely general 3×3 complex matrix, hence containing 9 real parameters and 9 complex phases. Using singular value decomposition we can rewrite it as

$$\lambda = U_\lambda D_\lambda V_\lambda, \quad (3.6)$$

with U_λ and V_λ being unitary matrices and D_λ being a diagonal matrix with real and positive entries.

This parametrization still contains a redundancy, since a diagonal re-phasing

	$SU(3)_c$	$SU(2)_L$	$U(1)_Y$	$U(3)_q$	$U(3)_u$	$U(3)_d$	$U(3)_\chi$
q_L	3	2	1/6	3	1	1	1
u_R	3	1	2/3	1	3	1	1
d_R	3	1	-1/3	1	1	3	1
l_L	1	2	1/2	1	1	1	1
e_R	1	1	-1	1	1	1	1
H	1	2	1/2	1	1	1	1
ϕ	3	1	2/3	1	1	1	1
χ_L	1	1	0	1	1	1	3
χ_R	1	1	0	1	1	1	3
Y_u	1	1	0	3	$\bar{3}$	1	1
Y_d	1	1	0	3	1	$\bar{3}$	1
λ	1	1	0	1	3	1	$\bar{3}$

Table 3.1: Symmetry transformation properties of relevant fields and couplings.

$$U_\lambda \rightarrow U_\lambda \text{diag}(e^{-i\alpha_1}, e^{-i\alpha_2}, e^{-i\alpha_3}) \quad (3.7)$$

$$V_\lambda \rightarrow \text{diag}(e^{i\alpha_1}, e^{i\alpha_2}, e^{i\alpha_3}) V_\lambda$$

leaves λ invariant. We use this re-phasing to remove 3 phases from U_λ . In addition, we can use the flavour symmetry $U(3)_\chi$ of the dark matter triplet to remove V_λ entirely. U_λ now contains 3 real parameters and 3 complex phases. We use the parametrization introduced in [43] to rewrite it in terms of three unitary matrices

$$U_\lambda = U_{23}^\lambda U_{13}^\lambda U_{12}^\lambda \quad (3.8)$$

$$= \begin{pmatrix} 1 & 0 & 0 \\ 0 & c_{23} & s_{23}e^{-i\delta_{23}} \\ 0 & -s_{23}e^{i\delta_{23}} & c_{23} \end{pmatrix} \begin{pmatrix} c_{13} & 0 & s_{13}e^{-i\delta_{13}} \\ 0 & 1 & 0 \\ -s_{13}e^{i\delta_{13}} & 0 & c_{13} \end{pmatrix} \begin{pmatrix} c_{12} & s_{12}e^{-i\delta_{12}} & 0 \\ -s_{12}e^{i\delta_{12}} & c_{12} & 0 \\ 0 & 0 & 1 \end{pmatrix}.$$

Here we used the abbreviation $s_{ij} = \sin\theta_{ij}$ and $c_{ij} = \cos\theta_{ij}$. In what follows we refer to θ_{ij} as the (flavour) mixing angles and to δ_{ij} as the phases of the coupling matrix λ . The remaining three parameters in

$$D_\lambda = \text{diag}(D_{\lambda,11}, D_{\lambda,22}, D_{\lambda,33}), \quad D_{\lambda,ii} > 0, \quad (3.9)$$

are referred to as the couplings $D_{\lambda,ii}$ —opposed to the coupling matrix λ . In summary, the generic λ contains 9 physical parameters. For completeness, we want to state the final expression of λ in terms of this parametrization:

$$\lambda = U_{23}^\lambda U_{13}^\lambda U_{12}^\lambda D_\lambda \quad (3.10)$$

$$= \begin{pmatrix} c_{12}c_{13}D_{\lambda,11} & s_{12}c_{13}e^{-i\delta_{12}}D_{\lambda,22} & s_{13}e^{-i\delta_{13}}D_{\lambda,33} \\ (-s_{12}c_{23}e^{i\delta_{12}} - s_{13}s_{23}c_{12}e^{i(\delta_{13}-\delta_{23})})D_{\lambda,11} & (c_{12}c_{23} - s_{12}s_{13}s_{23}e^{i(\delta_{13}-\delta_{12}-\delta_{23})})D_{\lambda,22} & s_{23}c_{13}e^{-i\delta_{23}}D_{\lambda,33} \\ (s_{12}s_{23}e^{i(\delta_{12}+\delta_{23})} - s_{13}c_{12}c_{23}e^{i\delta_{13}})D_{\lambda,11} & (-s_{23}c_{12}e^{i\delta_{23}} - s_{12}s_{13}c_{23}e^{i(\delta_{13}-\delta_{12})})D_{\lambda,22} & c_{13}c_{23}D_{\lambda,33} \end{pmatrix}.$$

To avoid a double counting of the parameter space we limit the parameters of U_λ to

$$\theta_{ij} \in [0, \pi/4] \quad (3.11)$$

$$\delta_{ij} \in [0, 2\pi). \quad (3.12)$$

The presence of both off-diagonal terms and complex phases in this most generic form of the coupling matrix clearly indicates that λ constitutes a new source of both flavour and CP violation. The parameter limits (3.11) for the chosen parametrization (3.10) in the generic case results in the first member of the dark flavour triplet coupling primarily to the first member of the up-quark triplet, etc. It is convenient to label the members of the DM triplet $\chi_j = (\chi_u, \chi_c, \chi_t)^\top$ by their naturally associated quark. We refer to χ_t as top-flavour, etc.

3.3 Dark Matter Stability

It is now time to discuss the arguments for a stable dark matter candidate. Therefor, we repeat the proof for the existence of an unbroken \mathbb{Z}_3 symmetry in the limit of exact DMFV for the dark matter triplet coupling to the quark sector. The proof has been given in [25] in an analogy to models of FDM in MFV [15].

First, we consider the most general operator of arbitrary dimension. We need to involve dark matter particles χ , the NP mediators ϕ as well as QCD colour-charged SM quarks q_L, u_R, d_R and also gluon fields and/or field strengths (summarized by \mathcal{G}). Finally, all other SM particles in a flavour symmetry and QCD neutral combination are included (denoted by \mathcal{S}). Of course, their respective anti-particles are considered as well. We end up with

$$\mathcal{O} \propto \chi \dots \bar{\chi} \dots \phi \dots \phi^\dagger \dots q_L \dots \bar{q}_L \dots u_R \dots \bar{u}_R \dots d_R \dots \bar{d}_R \dots \mathcal{G} \dots \mathcal{S} \dots \quad (3.13)$$

Here the dots represent an arbitrary number N_i of the respective fields i . The critical operator for DM decay is the one with $N_\chi = 1, N_{\bar{\chi}} = N_\phi = N_{\bar{\phi}} = 0$. Our goal is hence to prove that such an operator does not exist.

To do this we first consider the subset of \mathcal{O} which is invariant under QCD, i.e. $SU(3)_c$. For this to be the case we need it to be QCD colour-neutral, i.e.

$$\left(N_\phi - N_{\bar{\phi}} + N_u - N_{\bar{u}} + N_d - N_{\bar{d}} + N_q - N_{\bar{q}} \right) \bmod 3 = 0. \quad (3.14)$$

To consider invariance under the flavour symmetries, we need to include the most general combination of Yukawa couplings Y_u, Y_d and λ added as spurions to the operator

$$Y_u \dots Y_u^\dagger \dots Y_d \dots Y_d^\dagger \dots \lambda \dots \lambda^\dagger \dots \quad (3.15)$$

Requiring $U(3)_u, U(3)_d, U(3)_q$ and $U(3)_\chi$ invariance then demands

$$\left(N_u - N_{\bar{u}} - N_{Y_u} + N_{Y_u^\dagger} + N_\lambda - N_{\lambda^\dagger} \right) \bmod 3 = 0, \quad (3.16)$$

$$\left(N_d - N_{\bar{d}} - N_{Y_d} + N_{Y_d^\dagger} \right) \bmod 3 = 0, \quad (3.17)$$

$$\left(N_q - N_{\bar{q}} + N_{Y_u} - N_{Y_u^\dagger} + N_{Y_d} - N_{Y_d^\dagger} \right) \bmod 3 = 0, \quad (3.18)$$

$$\left(N_\chi - N_{\bar{\chi}} - N_\lambda + N_{\lambda^\dagger} \right) \bmod 3 = 0 \quad (3.19)$$

respectively. By summing (3.16) – (3.19) and subtracting (3.14) we find

$$\left(N_\chi - N_{\bar{\chi}} - N_\phi + N_{\bar{\phi}} \right) \bmod 3 = 0. \quad (3.20)$$

Hence, we see that a simultaneous invariance under the $SU(3)_c \times U(3)_u \times U(3)_d \times U(3)_q \times U(3)_\chi$ symmetry includes a \mathbb{Z}_3 symmetry. Under this \mathbb{Z}_3 the dark matter particles χ carry the charge $e^{i2\pi/3}$ and the NP mediator ϕ carries the charge $e^{-i2\pi/3}$. All SM particles carry \mathbb{Z}_3 charge +1.

We can therefore conclude that none of the new particles can exclusively decay into SM particles. Since we demand that the mediator ϕ is heavier than any member of the triplet χ , this implies the lightest flavour of χ as a stable dark matter candidate. The combination of DMFV and QCD invariance is hence enough to ensure this (for our choice of representations).

In case of FDM coupling to the lepton sector, no particles carrying QCD colour are present. Hence, the $SU(3)_c$ invariance requirement in the above derivation drops out and no residual \mathbb{Z}_3 symmetry is recovered. Even in the framework of DMFV, an additional symmetry, such as e.g. a \mathbb{Z}_2 , needs to be introduced to achieve stable dark matter [34].

3.4 Mass Spectrum of the Dark Sector

We now move on to discuss possible effects violating the perfect mass degeneracy of the dark flavours. As stated before, in DMFV we demand that there are no explicit contributions to the mass matrix m_χ , which directly violate the degeneracy.

The unavoidable contribution we are left with comes from renormalization group (RG)

running effects. The universal (at the high energy scale, where DMFV is broken) mass is at low scales renormalized by the coupling matrix λ . The resulting mass matrix, including the splitting corrections, is of the form

$$m_{\chi,ij} = m_{\chi} \left(\mathbf{1} + \eta \lambda^{\dagger} \lambda + \mathcal{O}(\lambda^4) \right)_{ij} = m_{\chi} \left(1 + \eta (D_{\lambda,ii})^2 + \mathcal{O}(\lambda^4) \right) \delta_{ij}. \quad (3.21)$$

Note that no summation over the indices is understood. The unitary matrices U_{ij}^{λ} (see (3.10)) drop out of the formula, leaving only a dependence on the couplings $D_{\lambda,ii}$. This also ensures only diagonal corrections to the mass matrix. The size of the corrections is parametrized by η , which ultimately depends on the exact details of the complete theory. From RG running we expect it to be of the order

$$\eta \propto \frac{1}{16\pi^2} \log \left(\frac{m_{\chi}^2}{\Lambda^2} \right), \quad (3.22)$$

with Λ being the previously mentioned high scale of DMFV breaking. In general, another correction $\propto \lambda^{\dagger} \lambda$ may arise at tree level in a DMFV preserving way, by integrating out additional heavy d.o.f. In this case we would expect $\eta \sim \mathcal{O}(1)$.

Since the value of η depends on the details of a complete theory, we will treat it as another parameter of the simplified model. We impose the constraint

$$|\eta (D_{\lambda,ii})^2| < 0.3 \quad (3.23)$$

to ensure convergence of the DMFV expansion in (3.21). Furthermore, we note that a negative value of η ensures that the masses of the dark matter flavours remain below the mediator mass. It turns out that a negative choice is anyway favoured by the collective constraints, see Chapter 4 and Chapter 7.

3.5 Minimal Flavour Violation Limit

So far, most of the established research was focused on models in the MFV framework. In this section, we analyze the connection of our up-quark DMFV model to those studies. As mentioned before, in MFV models, the only allowed sources of flavour (and hence CP) violation are the SM Yukawa couplings. This restricts the possible structures of the NP coupling matrix λ in terms of Y_u, Y_d . The first possible structure is

$$\lambda = \alpha \mathbf{1} + \beta Y_u^{\dagger} Y_u + \dots \quad (3.24)$$

with free parameters α and β . Looking at the flavour transformation properties of the spurion Yukawas (as well as the unit matrix $\mathbf{1}$ of course), it is easy to see that this corresponds to identifying $U(3)_{\chi}$ with $U(3)_u$. This transformation property then also limits the allowed

choice for mass terms in the dark sector:

$$m_{\chi,ij} = m_{\chi} \left(\mathbf{1} + \eta Y_u^{\dagger} Y_u + \dots \right)_{ij}. \quad (3.25)$$

Plugging the MFV assumption for λ , i.e. (3.24), into our DMFV form for the mass-splitting (3.21), we recover (3.25) (by identifying $\eta = 2\alpha\beta$). Therefore, we can conclude that MFV can be recovered as a consistent limit of DMFV for the identification $U(3)_{\chi} \hat{=} U(3)_u$.

The next possibility is the case of identifying $U(3)_{\chi}$ with $U(3)_d$. This case results in the MFV coupling structure

$$\lambda = \alpha Y_u^{\dagger} Y_d + \dots \quad (3.26)$$

and we find the required mass structure

$$m_{\chi,ij} = m_{\chi} \left(\mathbf{1} + \eta Y_d^{\dagger} Y_d + \dots \right)_{ij}. \quad (3.27)$$

Trying the same procedure as before, we find it impossible to recover this structure as a limit of the DMFV approach (3.21) for $U(3)_{\chi} \hat{=} U(3)_d$.

The third possibility is $U(3)_{\chi} \hat{=} U(3)_q$, with coupling matrix structure

$$\lambda = \alpha Y_u + \dots \quad (3.28)$$

and mass structure

$$m_{\chi,ij} = m_{\chi} \left(\mathbf{1} + \eta_1 Y_u Y_u^{\dagger} + \eta_2 Y_d Y_d^{\dagger} + \dots \right)_{ij}. \quad (3.29)$$

The MFV limit cannot be recovered for this choice either.

Hence, we can conclude that the only valid MFV limit corresponding to our DMFV model is $U(3)_{\chi} \hat{=} U(3)_u$. Keeping in mind that $Y_u \approx (0, 0, y_t)$, we can determine from (3.24) and (3.25) that this MFV limit has an approximate symmetry in the first and second generation of the dark sector as well. The coupling matrix is diagonal and the only element of significant size is the (3,3) component. The MFV framework—apart from the aim to keep it simple—is mainly chosen to guarantee safety from stringent constraints in the flavour sector. Nevertheless, one of the main results of this work is that the constraints by no means demand such a fixed structure. MFV misses a huge part of the generically allowed parameter space. This study emphasises that going beyond MFV models is well motivated.

Constraints from Direct Searches at the LHC

After having studied the main properties of the model, we now move on to study its phenomenology. We have to consider effects from the observed relic abundance of dark matter and direct detection experiments. Furthermore—as should be no surprise for a model of flavoured dark matter—constraints from flavour precision data need to be considered. All these constraints can be studied with a self-written MATHEMATICA [44] program. In this program all parameters of the model are randomized and the resulting model is tested against the constraints. If it does not violate any of the constraints, we keep the valid parameter set. Studying the patterns of those sets enables us to gain a deeper understanding of the model.

Of course we also need to consider the possibility of creating some of the new particles at particle colliders. The most serious collider constraints originate from the LHC data. Writing a MATHEMATICA program to study the collider phenomenology is not meaningful, since it could not compare at all in speed with the already existing implementation in MadGraph5_aMC@NLO [45]. MadGraph5_aMC@NLO is a powerful tool to study collider phenomenology (both in the SM as well as BSM), making use of the computational power of Markov Chain Monte Carlo (MCMC) methods. It allows to simulate processes up to LO accuracy for user-defined Lagrangians, and NLO accuracy for QCD corrections to SM processes. Using the program it is possible to compute cross sections as well as generate hard events, which can be studied further using a variety of tools. We will make use of MadGraph5_aMC@NLO to calculate the cross sections for processes in our NP model.

Due to these two different methods, it is not straightforward to conduct a combined analysis. Hence, for this work, we choose a split strategy. First we analyze the collider constraints. The resulting phenomenology is then used to identify a safe region of parameter space, i.e. we will pick parameter ranges in a meaningful way, avoiding all constraints of collider data by our choice. We will then move on to study the effects from the other aforementioned

constraints on this remaining safe parameter space. This strategy is suitable to achieve the main goal of this analysis, i.e. a combined analysis of all sources of constraints. Possible weak spots of this strategy are discussed in more detail in Chapter 8.

With this idea in mind, we now start with the analysis of the constraints from collider searches. The chapter is organized as follows. First we review some basic ideas and techniques of particle accelerators and detectors. Then we have a look at the relevant processes in our model, leading to phenomenologically interesting signals. Existing bounds on the most constrained signatures are used to infer constraints on the parameter space of our model. In Section 4.4 we discuss the impact of flavour mixing angles (of the NP coupling λ) on the phenomenology.

4.1 Detection Signatures at Particle Colliders

Particle colliders provide a unique approach to study possible extensions of the Standard Model, such as dark matter models. The majority of methods to search for hints on the nature of dark matter are based on searching for signals from the relic abundance of dark matter or observe contributions from higher order processes involving virtual new particles. Opposed to this, the main idea of collider searches is to actually produce these new particles on-shell, (re-)creating what only happens in the most energetic regions of the universe and very early after the Big Bang, when the universe was still hot enough. Making use of the equivalence of mass and energy, particle accelerators collide highly energetic SM particles to produce all kind of possible other particles in the process. If an interaction between NP particles—such as our dark matter flavours and mediator—and the SM particles does exist, those NP particles are bound to be produced in a fraction of the collisions—given the center of mass energy is large enough.

The final state particles of such collisions need to be identified to acquire some knowledge about the fundamental interactions, which have taken place in the collision. To detect the final state particles, the collisions are controlled to take place inside of particle detectors. There is a large variety of possible detection principles and methods, which we do not want to discuss in detail. In the following discussion, we will focus on the two general purpose detectors ATLAS and CMS at the LHC. Using multiple detection mechanisms and advanced reconstruction analytics it is possible to identify most of the standard particles to some degree of uncertainty. For our study the most important signals are those of light-quark jets, bottom-quark events, top-quark events and so-called missing transverse energy. We will discuss these possibilities in some more detail now.

If coloured (QCD) particles, such as a quark or a gluon, are created in the collision, they will create showers of colour-neutral particles due to the confinement of QCD. This process is known as hadronization and the showers of particles are known as jets. In principle the jets of light quarks (up, down, strange, charm) are very hard to distinguish. We will follow a standard convention, treating those light-quark jets as one kind of jet.

If a bottom-quark is created, it can often be identified as such using so-called *b-tagging*. This method is based on features unique to the bottom-quark and the resulting jets. The bottom-quark lifetime is long enough to allow the bottom-quark (or rather the hadron

containing the bottom-quark) to travel some distance from the primary vertex, yet is short enough, that the vast majority of bottom-quarks decays inside the particle detector. Relying on the high precision of modern silicon detectors allows to trace the products of this decay back to the place of the decay, distinguishing it from the primary collision point. Those so-called *displaced vertices* are a reliable indication for the presence of a bottom-quark in the process. In addition, the bottom-quarks in general are significantly more massive than their decay products, resulting in decay products with a higher transverse momentum than the original b-jet. This results in a larger angle of the jet, compared to light quark jets, a larger invariant mass of the jet and low-energetic leptons with momenta perpendicular to the jet. Observing these features in a jet is a strong—but not foolproof—indication for a b-jet.

Finally, to cover the last quark-flavour, top-quarks in the final state can also be reconstructed to some degree of uncertainty. The main idea again relies on b-tagging. The top-quark nearly instantly decays, nearly exclusively into a bottom-quark and a W-boson. Reconstruction of both the W-boson and the bottom-quark is then a strong indication for a top-quark having been created in the collision.

Apart from the quark-signals, the “signal” of dark matter in the detector is important for our study. The dark matter particles have avoided detection in all direct detection experiments so far. Hence, the cross section for interaction with SM matter has to be extremely small. If a DM particles is created in one of the many collision events at the particle accelerator, it is therefore highly unlikely that it will interact with the detector while passing through. This means that we do not detect the DM particle at all. Fortunately there is still a way to take note of the presence of dark matter particles, if they were not the only particles in the final state. Reconstructing the rest of the final state might lead to observing so-called *missing transverse energy* (MET) \cancel{E}_T . Since we know that the original particles in the collision have zero total momentum transverse to the beam pipe, momentum conservation tells us that the final state particles need to have zero transverse momentum as well. If we reconstruct those final state particles, which we can detect, and notice that we find a significant amount of transverse momentum, this is a strong indication that there must have been some particles, invisible to the detector, travelling into the opposite direction. Those additional particles carried the missing transverse momentum/energy. In the Standard Model, neutrinos are one example of such particles, basically invisible to the detector. In our model, the dark matter particles will result in a MET signature.

4.2 Processes and Signatures of the Model

The most stringent constraints from collider experiments are bounds coming from the LHC, especially from its two general purpose detectors ATLAS and CMS. The main idea of the presented analysis is using the similarity of signatures from our model to signatures from dedicated supersymmetry (SUSY) searches. To understand this, let us discuss the possible processes involving NP from our model in more detail.

Just as a NP particle can not exclusively decay to SM particles in our model, no NP particle can be singly produced from a pure SM initial state. Hence, all possible interactions at

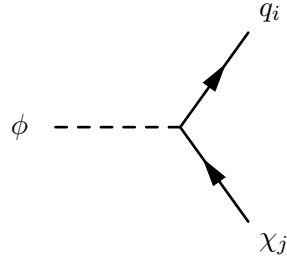


Figure 4.1: Decay modes of NP mediator. The branching ratios of the different decay channels depend on the coupling parameters.

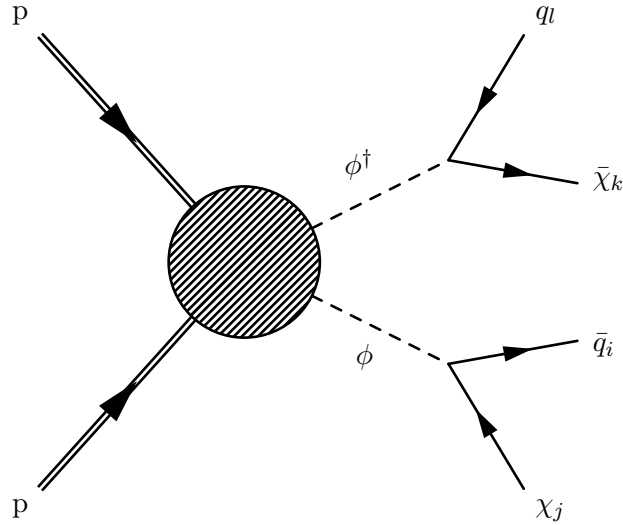


Figure 4.2: Studied LHC DM-creation processes. The contributions to the $pp \rightarrow \phi\phi^\dagger$ production process, here shown as an effective vertex, are given in Figure 4.3.

particle colliders involving NP from the presented model have to involve at least two of the new particles.

The most obvious signature is the direct production of a dark matter pair, i.e. $\chi\bar{\chi}$. Dark matter flavours—being a SM gauge singlet—will not interact with the particle detector, but can only be “detected” as missing transverse energy (MET) \cancel{E}_T . Hence, such a process can in principle not be detected at all. Yet, so-called initial state radiation may happen. One (or possibly many) gluons can be radiated off the initial state particles, resulting in a jet. If this jet is boosted against the DM particles, we observe a jet plus missing transverse energy signature. Of course instead of an initial state gluon, other particles, such as a photon, are possible in the same way. We neglect the possibility of heavier DM flavours decaying to the lighter DM flavours inside the detector. This possibility will be discussed below

The limits from these so-called mono-X signatures have been shown to be less stringent than the bounds from jet searches (to be discussed below) in case of a coloured t-channel mediator [46]. In [25] the authors found these results confirmed for the down-quark DMFV model. In analogy we expect this to hold the same way for the up-quark DMFV model.

The most relevant process is based on the production of $\phi\phi^\dagger$, since the bounds for the

produced signature are the strongest. To understand the signature of $\phi\phi^\dagger$, we have a look at the primary NP interaction between the dark matter triplet and the SM up-quark triplet via the NP mediator ϕ , see Figure 4.1. The latter can not decay exclusively to SM particles (see Section 3.3). Hence, its primary decay is mediated by the tree-level NP interaction, producing one SM quark and one DM flavour. The entire process is pictured in Figure 4.2. Two quark flavours and two DM flavours in the final state are produced.

As discussed in Section 4.1 the light quarks hadronize and shower in the detector. The top-quark—being significantly heavier—decays before it can hadronize. As discussed, it is possible—with some degree of uncertainty—to distinguish light-quark jets (with either up, charm, down and strange as primary quarks) from such showers with heavier quarks as origin. For our model, it hence makes a difference if a top-quark or a light quark (up or charm) is produced in the mediator decay. As discussed before, the dark matter flavours will only be “detected” as missing transverse energy. Again, we neglect the possible decay of heavier dark matter flavours.

The structure of this process and its signature is similar to some SUSY processes. If both quarks in the final state are top-quarks, it is analogous to the production of a stop anti-stop pair (the SUSY partners of the top-quark), with subsequent decay to $t\bar{t}$ and dark matter candidates of the considered SUSY model. In case of light-quark jets in the final state, it is analogous to first/second generation squarks with subsequent decay SM light quarks plus SUSY DM candidates.

For both cases dedicated ATLAS and CMS searches exist. The ATLAS collaboration provides exclusion bounds on the cross section of this process, depending on the involved squark and DM masses for the 8 TeV Run of the LHC. We choose two representative ATLAS analyses [47, 48] to constrain our model. For the considered model these translate to bounds on the cross section depending on the masses m_ϕ and m_χ .

There is also the possibility of producing $\chi\phi$. The mediator will subsequently decay and we will get a quark plus MET final state. Since bounds for the $\phi\phi^\dagger$ are more stringent, we focus on this process for the rest of the study.

To understand the process $pp \rightarrow \phi\phi^\dagger \rightarrow \chi\bar{\chi}q\bar{q}$ in more detail, let us first discuss the possible production modes of $\phi\phi^\dagger$, see Figure 4.3. Since ϕ is charged under QCD colour it couples to gluons and can hence be produced by pure QCD effects. The magnitude of the production hence only depends on one NP parameter, i.e. the mass of the mediator m_ϕ . The tree-level processes are shown in Figure 4.3a to Figure 4.3d.

In addition we also expect a contribution from t-channel DM exchange, see Figure 4.3e. This contribution depends on both the dark matter mass m_χ and the NP coupling matrix λ . We shall see in Section 4.3 that this has interesting consequences for the phenomenology.

To make it easier to understand the phenomenology, let us also look in more detail at the mediator decay modes, see Figure 4.1. The tree-level decay via the NP interaction depends on the parameters of the coupling matrix λ . The relative strength of the couplings to the different generations of quarks will hence determine the branching ratios and hence the probability for $t\bar{t}$ or jets final states.

Before we move on to study the constraints in more detail, let us summarize the approxi-

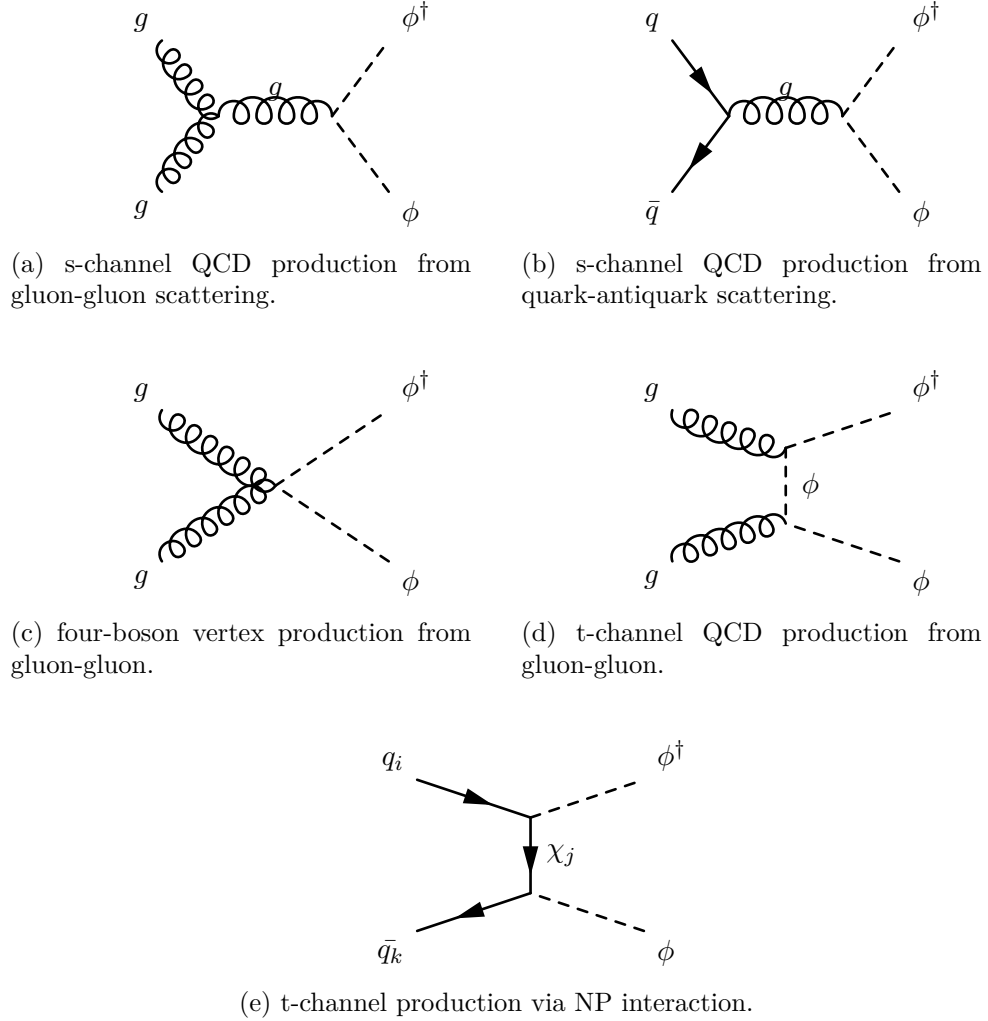


Figure 4.3: Relevant production channels for $\phi\phi^\dagger$. (a) to (d) are QCD processes, while (e) depends on the parameters of the NP model. We therefore expect a constant cross section from the first four diagrams (only depending on the mass of the mediator). From the last channel we expect more complex effects.

mations we make.

- The predicted cross sections for the up-quark DMFV model are directly compared to the bounds for the SUSY model studied by the experimental collaborations. In doing this we assume that the final state kinematics are comparable.
- Only leading (LO) contributions to the NP production cross section are taken into account.
- Bounds from mono-X searches are assumed to be negligible just as in previously studied analogous models.
- Possible final states with one top-quark and one light quark in the final state are an

additional signature of this model. Such $tj + \cancel{E}_T$ signatures are generated in a similar way in supersymmetric theories with flavour violating squark decays, see e.g. [49–54]. Since no dedicated searches for such signatures exist yet, we cannot include any bounds on them.

- Data from the 8 TeV LHC run 1 has been used for the constraining bounds. No analogous explicit cross section bounds from 13 TeV run 2 data have been made publicly available so far. Hence using data from run 2 would need a detailed, more sophisticated study, going beyond the scope of this work. The full data from run 2 will shift the bounds on the NP masses further up.
- The possibility of heavier DM flavours decaying into lighter DM flavours inside the detector is neglected. For a more detailed discussion of the decay of heavier flavours see Appendix D of [25]. For small mass-splittings, soft decay products (e.g. jets, photons, leptons) might not be energetic enough to be detected by the detectors at all. However, detecting soft objects in combinations with high p_T jets would be a strong hint for such chain decays. For a near degenerate case displayed decays would be a distinctive signature to look for. For more sizeable mass-splitting, we have to expect multi-jet signals in association with missing transverse energy. Such signals could be used to distinguish our model from other models with coloured mediators.

All these approximations are assumed to cause sub-leading quantitative, but no significant qualitative effect on the bounds derived in the following section.

4.3 Constraints and Safe Parameter Space

4.3.1 Methodology

A FEYNRULES [55] implementation of the up-quark DMFV model is used to create the so-called U.F.O. file, which contains all the information of the studied model in a form that can subsequently be understood by MadGraph5_aMC@NLO [45]. The MadGraph5_aMC@NLO result for the LO signal cross section is then compared with the aforementioned most constraining ATLAS searches [47, 48], which provide upper bounds on the signal cross section.

Evaluating a single parameter set in MADGRAPH takes $\mathcal{O}(1 \text{ minute})$ using a computer with an Intel(R) Core(TM) i5-4590 CPU @ 3.30GHz and 8GB RAM of memory. The model ultimately contains 11 free parameters—3 couplings $D_{\lambda,ii}$, 3 mixing angles θ_{ij} , 3 phases δ_{ij} , the dark matter mass parameter m_χ and the mediator mass m_ϕ . This list does not contain the parameter η , since mass-splitting between the dark matter flavours is neglected here. Due to the *curse of dimensionality* scanning this 11-dimensional parameter space with a moderate grid of just 10 points per parameter would last about a few hundred thousand years.

To get an idea of the phenomenology in a reasonable time, a smart scanning procedure is hence mandatory. In the parameter scan we make the following restrictions:

- All mixing angles and phases are set to zero. This results in a diagonal coupling matrix consisting of the couplings $D_{\lambda,ii}$. The influence of phases can not increase the magnitude of the cross section, hence setting them to zero can not result in an underestimation of the constraints. The influence of the mixing angles is discussed in detail in Section 4.4. In light of the choice of safe parameter space, we find that including them can not result in more serious constraints for this safe parameter space.
- The scan covers the subset of the parameter space with $D_{\lambda,11} = D_{\lambda,22}$. For the limit of diagonal coupling matrix, the couplings $D_{\lambda,11}$ and $D_{\lambda,22}$ govern the branching ratio for light-quark jets in the mediator decay, while $D_{\lambda,33}$ governs the top-quark case. Since we do not distinguish between up- and charm-quark jets, the degeneracy assumption $D_{\lambda,11} = D_{\lambda,22}$ is a reasonable and useful simplification. Of course $D_{\lambda,11}$ and $D_{\lambda,22}$ have different influence on the t-channel production process (see Figure 4.3e), due to the different up-quark and charm-quark PDFs in the proton). We need to keep this in mind, when analyzing the phenomenology.

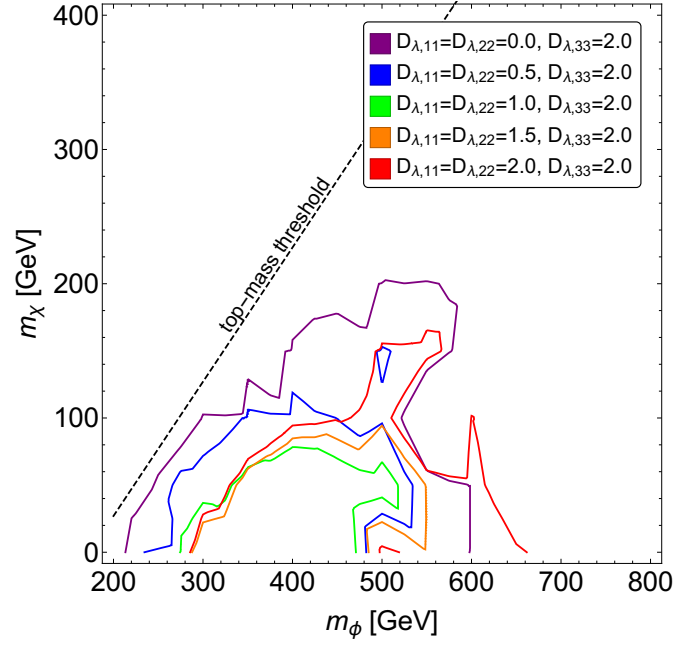
Using those restrictions a sufficient scan of the remaining parameter space can be conducted in a matter of weeks. We will now study the two signatures in turn.

4.3.2 $t\bar{t} + \cancel{E}_T$ Final State

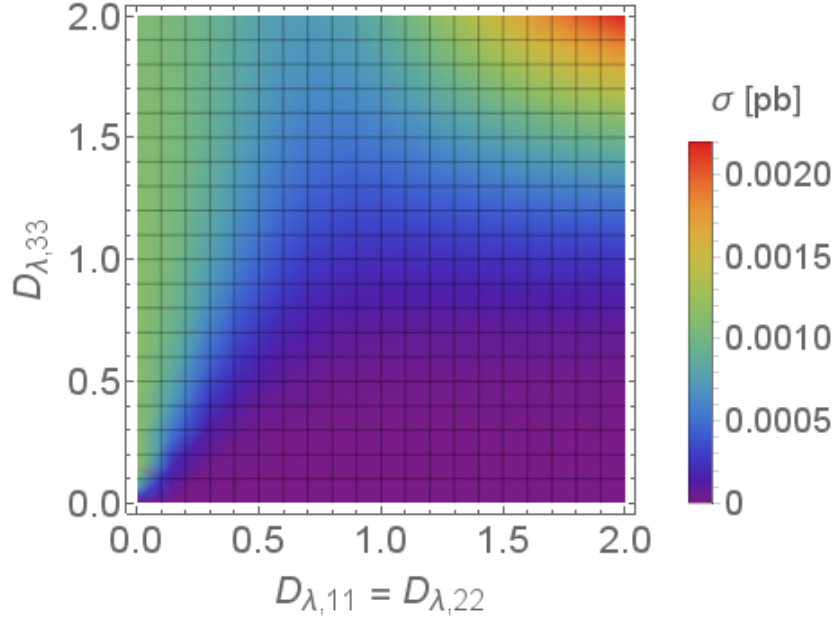
The first signature we study is $t\bar{t} + \cancel{E}_T$. For this signature, both mediators need to decay into third generation quarks. As discussed, we are working in the limit of $\lambda = D_\lambda = \text{diag}(D_{\lambda,11}, D_{\lambda,22}, D_{\lambda,33})$, which means that $D_{\lambda,33}$ governs the probability for the top-quark final state, while $D_{\lambda,11} = D_{\lambda,22}$ govern the probability for competing decays involving light quarks. Therefore, the branching ratio for third generation decay increases with increasing $D_{\lambda,33}$ and decreases with increasing $D_{\lambda,11} = D_{\lambda,22}$. As a first approximation we can expect the cross section to show the same pattern.

Figure 4.4a shows the 95% C.L. exclusion contours in the $m_\phi - m_\chi$ plane for the $t\bar{t} + \cancel{E}_T$ final state, obtained with the data from [47]. For the top-quark final state to be kinematically allowed, the mediator mass has to be split from the DM mass by at least the top-quark mass. For the parameter space with a smaller splitting between m_ϕ and m_χ the bounds from $t\bar{t} + \cancel{E}_T$ final state searches can hence not impose any constraints. This unconstrained area is the area above the “top-mass threshold” line in Figure 4.4a. In the figure we see various exclusion contours for different values of the couplings $D_{\lambda,ii}$. The area below the lines is excluded by the data. While the third generation coupling is fixed at a high value $D_{\lambda,33} = 2.0$ for all shown contours, we see the influence of different value of $D_{\lambda,11} = D_{\lambda,22}$.

Increasing $D_{\lambda,11} = D_{\lambda,22}$ from 0 to 0.5 and again from 0.5 to 1.0, we observe a reduction of the exclusion area, which is in agreement with a decrease of the cross section (CS), due to the diminished branching ratio of the top-quark final state. If we continue to increase the value of $D_{\lambda,11} = D_{\lambda,22}$, we at some point make a surprising observation. Instead of a further decline in the exclusion area, the exclusion area starts to grow. This can only be explained by a rise in the CS. Since the $t\bar{t} + \cancel{E}_T$ branching ratio has to drop, we conclude that the $\phi\phi^\dagger$ production has to be enhanced.



(a) 95% C.L. exclusion contours for varying first and second generation couplings at fixed $D_{\lambda,33} = 2.0$.



(b) LO $t\bar{t} + \cancel{E}_T$ cross section for 8 TeV pp collisions for $m_\phi = 850$ GeV and $m_\chi = 50$ GeV.

Figure 4.4: Constraints on the $t\bar{t} + \cancel{E}_T$ final state from 8 TeV LHC run 1 data, obtained from bounds in [47].

The explanation for this effect is the process in Figure 4.3e. While all the other production processes are pure QCD and hence independent of the NP couplings $D_{\lambda,ii}$, the process in this diagram depends on the NP coupling. At the LHC protons are collided. Protons consist of valence up- and valence down-quarks and various sea quarks and gluons. For the NP production in Figure 4.3e to happen, one of the following processes has to take place. Either a valence up-quark interacts with a \bar{u} sea quark, or one sea quark interacts with an anti sea-quark of the same generation. Since no top sea-quarks are present in protons, the chance for the process to happen is entirely governed by $D_{\lambda,11} = D_{\lambda,22}$.

We can hence understand the effect by concluding that for large couplings $D_{\lambda,11} = D_{\lambda,22}$ the NP production mode exceeds the QCD production. To get a more quantitative idea of this effect, we need to look at Figure 4.4b. In the figure we can see the cross section as a function of the coupling in the $(D_{\lambda,11} = D_{\lambda,22}) - D_{\lambda,33}$ plane for fixed masses $m_\phi = 850$ GeV and $m_\chi = 50$ GeV. For such a mass gap between the dark matter particles and the mediator, the effects from reduced phase space due to the large top-quark mass is irrelevant. In the figure we can observe the expected drop in cross section for increasing $D_{\lambda,11} = D_{\lambda,22}$ below about $D_{\lambda,11} = D_{\lambda,22} = 1.0$.

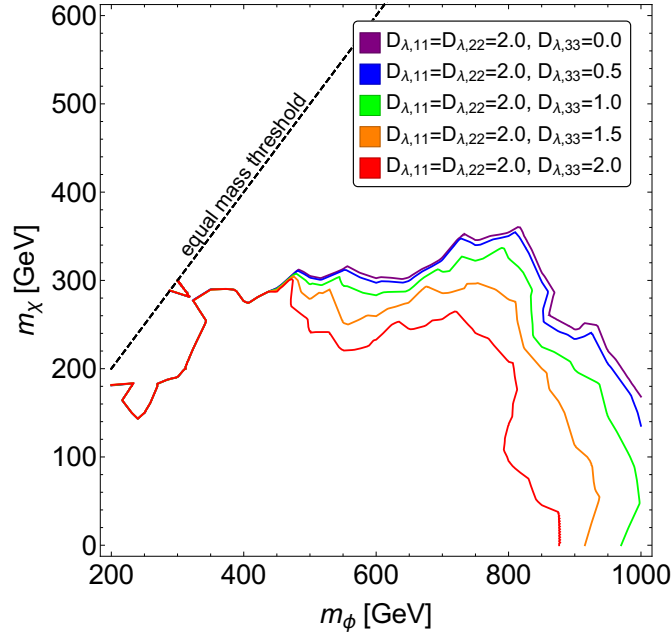
The effect of increased cross section for very large $D_{\lambda,11} = D_{\lambda,22}$ is only visible if $D_{\lambda,33}$ is also of sufficient size. For small $D_{\lambda,33}$, the suppression due to the drop in branching ratio is too significant to be compensated by the rise in production. If we look at the extreme case of $D_{\lambda,11} = D_{\lambda,22} = D_{\lambda,33} = 2.0$, we observe a cross section roughly twice as big as for $D_{\lambda,33} = 2.0$, $D_{\lambda,11} = D_{\lambda,22} = 0$. Neglecting the top-quark mass the branching ratio for each quark flavour in the final state is equally large for degenerate couplings $D_{\lambda,ii}$. Hence, the branching ratio for $t\bar{t}$ at $D_{\lambda,11} = D_{\lambda,22} = D_{\lambda,33} = 2.0$ is only 1/9 of the one at $D_{\lambda,33} = 2.0$, $D_{\lambda,11} = D_{\lambda,22} = 0$. We conclude that the production apparently is enhanced by more than a factor of 10. The NP production mode exceeds the combined effect of all QCD production modes by more than an order of magnitude for $D_{\lambda,11} = D_{\lambda,22} = 2.0$.

This increase in the production follows a power law in the couplings and hence leads to serious exclusion bounds, if even higher couplings are allowed. Hence a reasonable upper limit for the couplings needs to be chosen to prevent an exclusion of all the phenomenologically interesting mass range. A more detailed discussion on larger couplings can be found in Appendix A.

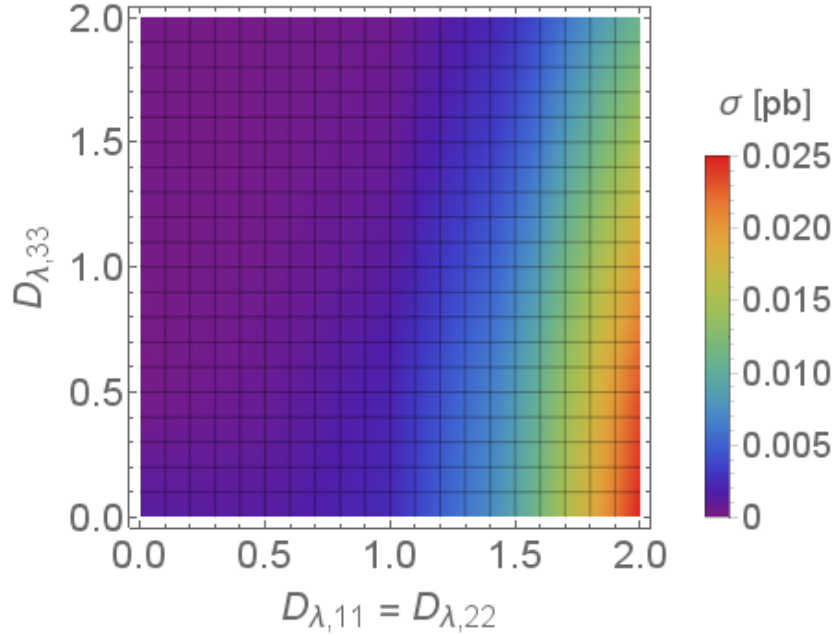
4.3.3 Jets + MET Final State

Now we have a look at the jets+ \cancel{E}_T final state. The model is constrained by the bounds in [48]. In this scenario the effects from branching ratio enhancement and production enhancement are adding up. Both effects increase with increasing $D_{\lambda,11} = D_{\lambda,22}$. On the x -axis of Figure 4.5b we can see the pure effect of the production enhancement, showing an exponential growth of the cross section. We hence find our previous observation confirmed.

Increased $D_{\lambda,33}$ causes a drop in the branching ratio to jets. Since both first generation quarks in the final state are counted as a jet event, the drop in branching ratio from $D_{\lambda,33} = 0$ to $D_{\lambda,33} = D_{\lambda,11} = D_{\lambda,22}$ is (neglecting the top-quark mass) only 4/9 and hence not as significant as in the $t\bar{t}$ case. The factor of 4/9 originates from the drop in probability



(a) 95% C.L. exclusion contours at fixed $D_{\lambda,11} = D_{\lambda,22} = 2.0$ and increasing $D_{\lambda,33}$.



(b) LO jets + \cancel{E}_T cross section for 8 TeV pp collisions for $m_\phi = 850$ GeV and $m_\chi = 50$ GeV.

Figure 4.5: Constraints on the jets + \cancel{E}_T final state from 8 TeV LHC run 1 data, obtained from bounds in [48].

for a mediator to decay into light quarks. For $D_{\lambda,33} = 0$ the mediator can only decay to up- or charm-quark, while in the case of $D_{\lambda,33} = D_{\lambda,11} = D_{\lambda,22}$, the probability for decay to either up- or charm-quark is (neglecting the top-quark mass) $2/3$. Hence the probability for both mediators to decay to light quarks and ultimately producing the jet signature is $2/3 \cdot 2/3 = 4/9$. Looking at the $D_{\lambda,11} = D_{\lambda,22} = 2.0$ line in Figure 4.5b, we can observe the pure effect of decrease in branching ratio with increasing $D_{\lambda,33}$ at the expected rate. Hence, we can be confident that no significant effects are neglected.

Note that the maximum CS reached in Figure 4.5b is an order of magnitude bigger than the one reached in Figure 4.4b for the same parameter space. Figure 4.5a shows the exclusion contours for the jets+ \cancel{E}_T final state. We show contours at fixed $D_{\lambda,11} = D_{\lambda,22} = 2.0$ and observe the effect of increasing $D_{\lambda,33}$. As expected the only effect is a continuous reduction of the excluded area, but in a moderate way.

Even for the degenerate case of $D_{\lambda,33} = D_{\lambda,11} = D_{\lambda,22} = 2.0$ a significant amount of parameter space is still excluded. Overall the exclusion bounds from the jets final state search prove to be more stringent than the ones from $t\bar{t} + \cancel{E}_T$ data, mostly due to the new physics production process in Figure 4.3e. Even more than $t\bar{t} + \cancel{E}_T$ data, the jets+ \cancel{E}_T bounds demand a reasonable upper limit on the couplings.

We are primarily interested in DM masses that are $\mathcal{O}(10 \text{ GeV} - 1 \text{ TeV})$, since this is the phenomenologically interesting range, which will be probed in the upcoming decades. NP at this scale is motivated by several popular extensions of the Standard Model. One example for such motivation is the so-called WIMP miracle. A weakly interaction massive particle (WIMP), i.e. a dark matter particle of a few hundred GeV mass, which has a coupling of weak interaction strength to SM particles, is found to reproduce approximately the correct relic abundance of DM in a thermal freeze-out scenario.

For reasons that will be explained in more detail in Chapter 6 and Chapter 7, a DM mass in this interesting region in our model should be associated with a mediator of mass in the TeV range. Yet, we can see that for $D_{\lambda,33} < D_{\lambda,11} = D_{\lambda,22}$ the collider constraints from the 8 TeV LHC run 1 data alone are enough to eliminate a significant part of the interesting parameter space.

For the rest of our analysis, we therefore focus on the parameter space with $D_{\lambda,11}, D_{\lambda,22} < D_{\lambda,33}$. At the same time we demand $D_{\lambda,ii} \leq 2.0$ due to the NP production enhancement, which needs to be kept at bay. We will see in Chapter 7 that direct detection constraints also demand an upper bound on the couplings. With our current choices we are left with the red exclusion contour in Figure 4.5a as the worst possible exclusion limit. Figure 4.6 shows the exclusion contours for increasing values of degenerate $D_{\lambda,ii}$. The figure illustrates that the bounds strictly rise with degenerate couplings and hence $D_{\lambda,33} = D_{\lambda,11} = D_{\lambda,22} = 2.0$ produces the most stringent constraints amongst the safe parameter space.

Therefore, by additionally limiting the parameter space to the area with $m_\phi > 850 \text{ GeV}$ we can make sure that even for the maximally allowed couplings, no interesting part of the DM mass spectrum is excluded by the jets+ \cancel{E}_T constraints. At the same time we are also safe from the $t\bar{t} + \cancel{E}_T$ bounds for this choice, see Figure 4.4a.

We have hence identified a safe parameter space, in which the parameters are limited in a meaningful way for the further analysis, avoiding all bounds from the present collider data.

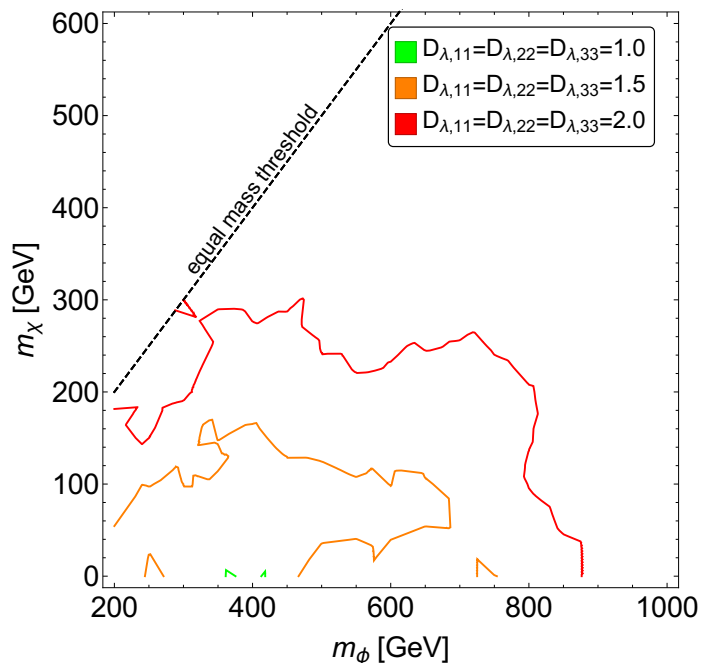


Figure 4.6: Constraints on the jets + \cancel{E}_T final state from 8 TeV LHC run 1 data, obtained from bounds in [48]. The figure shows the exclusion contours for degenerate $D_{\lambda,ii}$ at different values. We observe that the exclusion area strictly grows with increasing $D_{\lambda,11} = D_{\lambda,22} = D_{\lambda,33}$.

At this point we want to address one of the simplification we made by setting $D_{\lambda,11} = D_{\lambda,22}$. The major reason to the large cross sections for large couplings $D_{\lambda,11} = D_{\lambda,22}$ is the enhanced $\phi\phi^\dagger$ production. The main contribution is governed by $D_{\lambda,11}$, due to the valence up-quark in the proton. Yet in our choice of safe parameter space we demand $D_{\lambda,22} < D_{\lambda,33}$ as well. This choice is not just purely motivated by the collider bounds, but also due to the fact that other constraints favour top-flavoured dark matter relic, see Chapter 6 and Chapter 7. This can be achieved by making sure that the top-flavour is the lightest flavour. From (3.21) we can read off the dependence of the mass-splitting on the couplings $D_{\lambda,ii}$. To make sure that the top-flavour is the lightest, we need the coupling $D_{\lambda,33}$ to be either the lowest or the highest. Due to the reasons discussed before, we chose the latter case. Chapter 8 will discuss in more detail the strong case for top-flavoured DM and the ranking of the couplings made by the combined analysis.

4.4 Effects of Flavour Mixing Angles

At this point, we want to address the influence of the flavour mixing angles in λ . In the collider analysis so far, the mixing angles have been set to zero. The presence of mixing can in general have a significant impact on the LHC constraints. Effectively the non-zero mixing angles shift the influence of couplings. E.g. a non-zero mixing angle θ_{ij} enables the decay of the mediator ϕ into a DM flavour χ_j and a SM quark q_i , which is not primarily

associated with this DM flavour. This decay is then governed by $D_{\lambda,jj}$ instead of $D_{\lambda,ii}$. These shifts can affect the NP production (Figure 4.3e) in an analogous way.

In case of a significant splitting between the couplings $D_{\lambda,ii}$, the mixing angles can therefore cause significant shifts in the phenomenology. Nevertheless, such effects can never cause any problems for the previously chosen safe parameter space. To understand why, let us look at an exemplary case. A process that is governed by a coupling $D_{\lambda,ii} = A_1$ in the case of no mixing, will get influences from a coupling $D_{\lambda,jj} = A_2$ by the presence of the flavour mixing angle θ_{ij} . Assuming that $A_2 > A_1$ this will cause the cross section for the original process to increase. Yet the mixing can never cause the cross section to rise above the value it would take for $D_{\lambda,ii} = A_2$ in the case of no mixing. Since the safe parameter space is limited to $D_{\lambda,11}, D_{\lambda,22} < D_{\lambda,33} \leq 2.0$, the cross section for interactions with light quarks will be strictly bound from above by the cross section value for the case of $D_{\lambda,11} = D_{\lambda,22} = 2.0$ case. This extreme case can be only be reached in the case of $D_{\lambda,33} = D_{\lambda,11} = D_{\lambda,22} = 2.0$. In this degeneracy case the mixing angles have no effect at all. Hence, the red exclusion contour in Figure 4.5a remains the worst possible exclusion, even in the presence of non-zero mixing angles.

In conclusion, the safe parameter space identified in Subsection 4.3.3 will ensure compliance with the collider constraints also in the presence of arbitrary mixing angles.

4.5 Summary of Collider Constraints Results

In summary, the following observations on the up-quark DMFV model phenomenology have been made in light of the LHC searches for SUSY squarks:

- Bounds from jets + \cancel{E}_T final states provide the most stringent constraints, clearly exceeding the second most stringent bounds of the $t\bar{t} + \cancel{E}_T$ final state.
- The NP t-channel DM exchange production process in Figure 4.3e becomes the dominant contribution for large couplings $D_{\lambda,11} = D_{\lambda,22}$.
- The constraints of collider searches can be avoided by restricting our parameter space in a meaningful way for the following studies. This *safe parameter space* is given as follows:

$$m_\phi > 850 \text{ GeV}, \quad (4.1)$$

$$2.0 \geq D_{\lambda,33} \geq D_{\lambda,11}, D_{\lambda,22}. \quad (4.2)$$

In light of the 13 TeV LHC run 2 data the bounds for m_ϕ are expected to be too low to guarantee safety for the highest allowed couplings and simultaneously low DM masses. However, we will see in the following analysis, that the DM mass will be bounded from below by a combination of constraints from relic abundance and direct detection data. At the same time bounds from future direct detection measurements will give rise to an upper bound on the couplings, see Subsection 7.3.3. Therefore, even the updated constraints from run 2 might not cause more serious constraints

for the range of mediator mass we consider. This subject will be discussed in greater detail in Chapter 8.

- Non-zero mixing angles in the NP coupling λ can in principle have a big impact on the phenomenology. However, the choice of safe parameter space ensures that the constraints from collider searches are always satisfied.

Constraints from Flavour Precision Experiments

After having identified the safe parameter space from collider constraints, we now move on to study the impact from other constraints. Before looking at the combined analysis, we want to understand the individual effects. In this chapter we start with bounds from flavour precision data. We find that the bounds from neutral meson mixing are the most relevant for our model. The basic ideas of CP violation in neutral meson mixing and the SM contributions to this process have been sketched in Section 2.2. In this chapter, we discuss the contributions of the NP model to those observables. After identifying the impact on the model parameters, we discuss the impact on rare decays, justifying why those bounds are negligible.

5.1 Contributions to Neutral Meson Mixing

As discussed in Chapter 3, the NP coupling matrix λ in the generic DMFV framework not only includes flavour mixing angles θ_{ij} , but also complex phases δ_{ij} . Hence we expect significant new effects on flavour and CP observables. The most significant bounds are those from neutral meson mixing data. We will argue in Section 5.3, that the NP contributions to rare decays in our model are naturally small and can hence be ignored.

The only relevant meson consisting of flavours of the SM up-quark triplet is the D meson, in contrast to three existing mesons consisting of down-quark flavours. Due to the large mass and hence negligible lifetime of the top-quark no bound states of it exist. The latest bounds on neutral D meson mixing [56] are not as stringent as comparable data from $K^0 - \bar{K}^0$ and $B_{d,s} - \bar{B}_{d,s}$ oscillations in the down-quark sector. Hence, we find less serious constraints for the up-quark DMFV model than those found for the down-quark DMFV model in [25]. We now analyze the constraints from $D^0 - \bar{D}^0$ mixing on our model in detail.

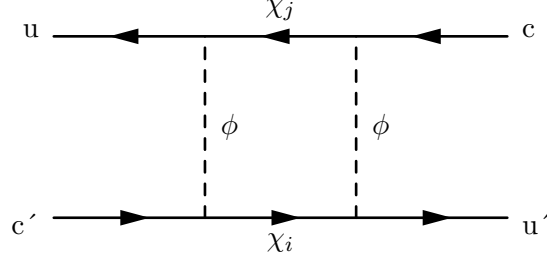


Figure 5.1: Feynman diagram of leading order NP process in neutral D-meson mixing.

The leading order NP contribution to $D^0 - \bar{D}^0$ mixing is given analogously to electroweak box diagrams contributions in the SM, see Figure 2.1 for the LO SM contribution to neutral Kaon mixing. The Feynman diagram of the LO NP process contributing to $D^0 - \bar{D}^0$ mixing is shown in Figure 5.1.

The Feynman diagram represents the amplitude:

$$\begin{aligned}
 i\mathcal{A} = & \sum_{i,j} \int \frac{d^4k}{(2\pi)^4} \bar{u}_R \lambda_{uj} \frac{i \left((-p_u^\mu + k^\mu) \gamma_\mu + m_{\chi_j} \right)}{(p_u^\mu - k^\mu)^2 - m_{\chi_j}^2 + i\epsilon} \lambda_{cj}^* c_R \\
 & \times \bar{u}'_R \lambda_{ui} \frac{i \left((p_{c'}^\nu + k^\nu) \gamma_\nu + m_{\chi_i} \right)}{(p_{c'}^\nu + k^\nu)^2 - m_{\chi_i}^2 + i\epsilon} \lambda_{ci}^* c'_R \\
 & \times \frac{i}{k^2 - m_\phi^2 + i\epsilon} \cdot \frac{i}{(k^\nu + p_{c'}^\nu - p_{u'}^\nu)^2 - m_\phi^2 + i\epsilon} + \text{rotated diagram}
 \end{aligned} \tag{5.1}$$

with k^μ being the loop momentum and the rest following common conventions. We need to sum over the DM flavours. Since the mixing happens in the meson rest frame, it is safe to assume that the external momenta (of the participating valence quarks) are small compared to the loop-momentum: $p_i \ll k$ for all relevant values of k and besides $p_i^2 \ll m_{\chi_i}^2, m_\phi^2$. The expression for the amplitude then simplifies significantly. It can be solved with the standard method using Feynman parameters, see e.g. [57].

For the effective Hamiltonian describing neutral D meson mixing we ultimately find:

$$\mathcal{H}_{eff}^{\Delta C=2,new} = \frac{1}{128\pi^2 m_\phi^2} \sum_{i,j} \lambda_{uj} \lambda_{cj}^* \lambda_{ui} \lambda_{ci}^* \cdot L(x_i, x_j) \cdot Q_{uc}^{VRR} + h.c. \tag{5.2}$$

with the effective operator

$$Q_{uc}^{VRR} = (\bar{u}_\alpha \gamma_\mu P_R c_\alpha) (\bar{u}_\beta \gamma_\nu P_R c_\beta) \tag{5.3}$$

and the loop function

$$L(x_i, x_j) = \left(\frac{x_i^2 \log(x_i)}{(x_i - x_j)(1 - x_i)^2} + \frac{x_j^2 \log(x_j)}{(x_j - x_i)(1 - x_j)^2} + \frac{1}{(1 - x_i)(1 - x_j)} \right) \quad (5.4)$$

with

$$x_i = \frac{m_{\chi_i}^2}{m_\phi^2}. \quad (5.5)$$

Please note that, while the amplitude (5.1) contains distinguishable spinors, the effective operator (5.3) contains the indistinguishable fields, which in total leads to two Wick contractions $(\bar{u}'_\alpha \gamma_\mu P_R c'_\alpha)(\bar{u}_\beta \gamma_\nu P_R c_\beta)$ and two Wick contractions $(\bar{u}'_\alpha \gamma_\mu P_R c'_\beta)(\bar{u}_\beta \gamma_\nu P_R c_\alpha)$. In the matching, we hence find a symmetry factor of 2 in the Wick contractions on the effective field theory (EFT) side, which leads to the addition factor of 1/2 in the coefficient of (5.2).

For $x_i = x_j = x$, i.e. degenerate masses of the dark matter flavours, the loop function simplifies to

$$L(x) = \frac{2x \log(x)}{(1-x)^3} + \frac{(1+x)}{(1-x)^2}. \quad (5.6)$$

From (5.2) we get the NP contribution to the off-diagonal mass matrix element of the $D^0 - \bar{D}^0$ system

$$\begin{aligned} M_{12}^{D,\text{new}} &= \frac{1}{2m_D} \langle \bar{D}^0 | \mathcal{H}_{\text{eff}}^{\Delta C=2,\text{new}} | D^0 \rangle^* \\ &= \frac{1}{384\pi^2 m_\phi^2} \eta_D m_D f_D^2 \hat{B}_D \sum_{i,j} \lambda_{ui}^* \lambda_{ci} \lambda_{uj}^* \lambda_{cj} \cdot L(x_i, x_j). \end{aligned} \quad (5.7)$$

Here we used the commonly used parametrization of the hadronic matrix element

$$\langle \bar{D}^0 | Q_{uc}^{VRR} | D^0 \rangle = \frac{2}{3} m_D^2 f_D^2 \hat{B}_D. \quad (5.8)$$

In this formula m_D is the mass of the neutral D meson, which can be measured in experiment. Furthermore we introduced the form factor f_D and the bag parameter \hat{B}_D , which are both quantities which have to be calculated on the lattice. Finally η_D contains corrections from RG running from the weak scale $\mu \sim M_W$ down to the meson scale $\mu = 3 \text{ GeV}$ [58], at which the relevant lattice calculations [59, 60] are performed. Just as in the original DMFV paper [25], RG running from the weak scale to the NP scale as well as differences in matching conditions between the SM and the NP scenario are being neglected. We expect this to cause negligible quantitative corrections to the phenomenology.

m_{D^0}	$(1864.75 \pm 0.15 \pm 0.11) \text{ MeV}$
\hat{B}_D	0.75 ± 0.02
f_D	$209.2 \pm 3.3 \text{ MeV}$
η_D	0.772
τ_{D^0}	0.41 ps
x_{12}^D	$\in [0.10\%, 0.67\%] \text{ (95\% CL)}$
Φ_{12}^D	$\in [-5.3^\circ, 4.4^\circ] \text{ (95\% CL)}$

Table 5.1: Parameters and experimental constraints used in the numerical analysis [42, 56, 58–61].

Due to the significant mass gap between the neutral D meson and the particles in the considered NP scenario, no contributions to the off-diagonal entry of the absorptive part Γ_{12}^D of the mixing amplitude are obtained.

5.2 Phenomenological Analysis

To study the phenomenology we use the parameters collected in Table 5.1. The model-independent constraints on the $D^0 - \bar{D}^0$ mixing amplitude [56], need to be converted to compare with the element $M_{12}^{D,\text{new}}$ calculated above. Using the standard convention $\arg(\Gamma_{12}^D) = 0$, the CP-violating phase Φ_{12}^D is simply the phase of $M_{12}^{D,\text{new}}$. The SM contribution to Φ_{12}^D is expected to be $\mathcal{O}(10^{-3})$. Hence, we neglect that contribution compared to potential large contributions from the NP complex phases δ_{ij} . The SM prediction for the absolute value of $M_{12}^{D,\text{new}}$ is less precise, due to the dominant long-range contributions. The SM contribution to

$$x_{12}^D = \frac{2|M_{12}^D|}{\Gamma_D} = 2|M_{12}^D|\tau_{D^0} \quad (5.9)$$

are expected to be $\mathcal{O}(1\%)$ [62]. For this study we use the very conservative estimate of $x_{12}^{D,SM} \in [-3\%, 3\%]$. We use this and the 95% C.L. intervals in Table 5.1 to constrain the parameters of the NP coupling λ in the following way.

Assuming the largest possible absolute values for x_{12}^D and Φ_{12}^D we can calculate the worst possible absolute value of the imaginary part of M_{12}^D which has not been excluded yet. Since we expect no SM contribution to the imaginary part, this value is imposed as an upper bound on the absolute value of the NP contribution to $\Im(M_{12}^D)$.

In addition we constrain the real part of $M_{12}^{D,\text{new}}$. The SM and NP contributions need to result in a combined value of $x_{12}^D \in [0.10\%, 0.67\%]$. Since we assume the SM contribution to not exceed 3% in absolute value, the NP contribution can in conclusion not exceed this by far either. For simplicity we impose a 3% bound for $|x_{12}^{D,\text{new}}|$ as well. The bounds on real and imaginary part of $M_{12}^{D,\text{new}}$ are numerically:

$$\begin{aligned}
|\Im(M_{12}^{D,\text{new}})| &\leq 5.0 \cdot 10^{-16} \text{ GeV}, \\
|\Re(M_{12}^{D,\text{new}})| &\leq 2.4 \cdot 10^{-14} \text{ GeV}.
\end{aligned}
\tag{5.10}$$

For the course of the analysis, the assumption of degenerate DM masses is used. The only place the explicit masses enter in the formula is the loop function $L(x_i, x_j)$. Since we restrain ourselves to 30% maximum correction to the DM mass, see (3.23), it can be shown that such splittings result in minor percent level corrections which will have no significant influence on the phenomenology.

The meson data is not sensitive to the relic of dark matter, but is only influenced by virtual NP in loop corrections. Hence, we make no assumptions on the hierarchy in the dark sector.

Figure 5.2 shows the valid areas of the flavour mixing angles which remain after imposing the flavour bounds in form of (5.10), for an exemplary choice of dark matter and mediator mass. The pattern remains qualitatively the same for different mass values. The valid values for a mixing angle θ_{ij} are shown in dependence on the coupling splitting $|D_{\lambda,ii} - D_{\lambda,jj}| = \Delta_{ij}$.

To understand the resulting form, we need to have a closer look at (5.7). The part involving the NP coupling and therefore the mixing angles can be rewritten, using the parametrization in (3.10), as

$$\sum_{i,j} \lambda_{ui}^* \lambda_{ci} \lambda_{uj}^* \lambda_{cj} = \left((\lambda \lambda^\dagger)_{cu} \right)^2 = \left((U_\lambda D_\lambda D_\lambda^\dagger U_\lambda^\dagger)_{cu} \right)^2.
\tag{5.11}$$

D_λ is diagonal, while U_λ is the product of three unitary matrices $U_\lambda = U_{23}^\lambda U_{13}^\lambda U_{12}^\lambda$. Of the product, only the off-diagonal cu-component is relevant for $M_{12}^{D,\text{new}}$. This component can be suppressed in two different ways. Either the related mixing angle is directly suppressed, or there is a sufficient degeneracy between the couplings. The degeneracy solution comes as no surprise, since a $D_\lambda \propto \mathbb{1}$ allows to commute U_λ with it. Since U_λ is unitary, we are then left with a purely diagonal matrix and the cu-component is naturally zero.

In practice no perfect degeneracy of the couplings is necessary. The major contribution to the cu-component is proportional to $(\sin \theta_{12})^2 (D_{\lambda,22} - D_{\lambda,11})^2$. There are several sub-leading contributions. Yet the major term is dominating the phenomenology completely, as becomes apparent in Figure 5.2. We observe valid points either for sufficiently degenerate couplings $D_{\lambda,22}, D_{\lambda,11}$, or for sufficiently suppressed mixing angle θ_{12} .

The constraints are not strong enough to have comparable effects on the other mixing angles. Only for simultaneously large θ_{13} and θ_{23} they generate a significant contribution to $D^0 - \bar{D}^0$ mixing. Since Figure 5.2 shows the valid areas without fixing other parameters, this correlation remains hidden in the figure. Compared to the down-quark DMFV model [25], the flavour constraints from the up-quark regime are of more limited consequences. Future data from flavour experiments, such as Belle II [63], will improve the bounds. In addition, the large uncertainty of the theory prediction of x_{12}^D remains an important point for improvement.

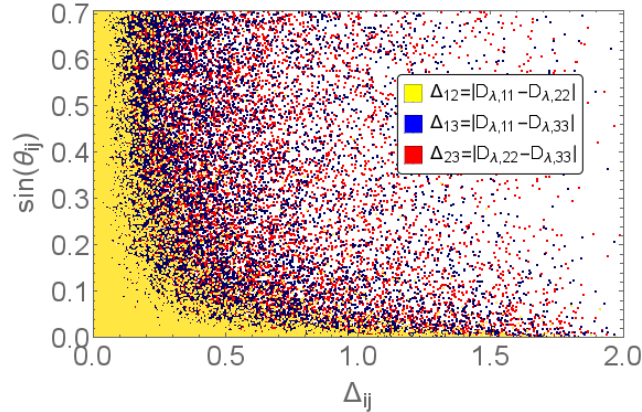


Figure 5.2: Valid ranges of flavour mixing angles θ_{ij} in dependence of the splittings between the associated couplings $D_{\lambda,ii}$ and $D_{\lambda,jj}$, for mediator mass $m_\phi = 850$ GeV and DM mass $m_\chi = 250$ GeV. The different colours correspond to the different mixing angles θ_{ij} and splittings $|D_{\lambda,ii} - D_{\lambda,jj}| = \Delta_{ij}$: $ij = 12$ in yellow, $ij = 13$ in blue, $ij = 23$ in red.

5.3 Remarks on Potential Effects from Rare Decays

Concerning the constraints from data on rare decays of the D meson, we recall the results found in the original down-quark DMFV model [25] for rare K and B decays. The authors found the NP contributions for those decays to be negligible. This conclusion can be transferred to our model. We expect SM-like predictions for rare D meson decays. Hence, we find no further impact on our model.

Nearly all constraints from rare flavour violating top-quark decays are so far not stringent enough to be relevant for our model, either. The only exception is the FCNC top-quark decay $t \rightarrow q + \text{invisible}$ with $q = u, c$. In case of a sufficiently small DM mass $m_\chi < (m_t/2)$, the decay $t \rightarrow \chi \bar{\chi} q$ is kinematically allowed, potentially resulting in a large NP contribution to the signature. Due to the large top-quark mass, this is a relevant constraint on part of the interesting DM mass range. Nevertheless, we will not study its implications here, since we will see later in more detail that such low DM masses are already excluded by a combination of relic abundance, direct detection and collider constraints.

5.4 Summary of Effects from Flavour Constraints

To conclude the chapter, we want to give a small summary of our results. The main observations on the implications of flavour constraints on the up-type DMFV model are:

- Compared to the down-type DMFV model the constraints from flavour data have less significant implications on the mixing angles θ_{13} and θ_{23} . Independently of the splittings between the couplings they can take large values. Only simultaneous large values of both θ_{13} and θ_{23} are excluded for large splittings between the couplings.

-
- The main constraint is the one on θ_{12} . For larger splitting between the couplings $D_{\lambda,11}$ and $D_{\lambda,22}$, the mixing angle is significantly bounded from above.
 - Data from rare decays has no impact on the part of the parameter space which is not already excluded by the other bounds.

Constraint from Relic Abundance of Dark Matter

In this chapter we study the impact of the observed relic abundance of dark matter on our model. First we have a look at the latest measurements of the energy content of the universe. We discuss the idea of dark matter thermal freeze-out to explain the observed relic and its implication for dark matter models. Then, we derive the dark matter annihilation cross section for the most general version of the considered model. Depending on the involved masses and couplings we derive several limits of this formula, discussing their impact on the parameters. For two interesting benchmark scenarios we study the phenomenology in detail.

6.1 Measurements of Relic Abundance

The relic abundance of dark matter can be estimated by studying the directional fluctuations of the cosmic microwave background (CMB). After the Big Bang, the temperature of the universe remained for a considerable amount of time high enough to prevent the formation of atoms. The photons were energetic enough to ionize even hydrogen atoms, keeping electrons and nuclei in a lasting plasma state. Due to the large number of photons present (approximately 10^{10} times more photons than baryons), the ions were prevented from clustering, preventing any structure formation of SM matter in this early stage of the universe. Nevertheless, density oscillations in the plasma were present.

When the temperature finally dropped so low that an insignificant fraction of the photons remained energetic enough to ionize hydrogen, the electrons and nuclei formed electrically neutral atoms. This process is known as recombination. As a consequence the matter became transparent for the photon background, for the first time. The momentary density fluctuation at the time of recombination became imprinted in the energy density of the photons. Those photons form the CMB, which can be observed today. Please note that the

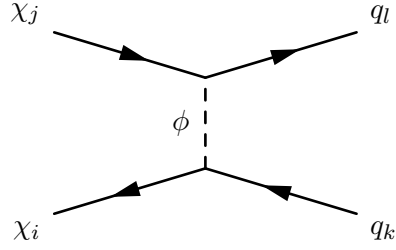


Figure 6.1: Tree-level process of DM annihilation.

process of recombination is a statistical process, actually extended over a significant period of time. We have omitted many details in this short review of the main ideas.

At present time, the energy fluctuations in the CMB can be detected to high precision by highly advanced experiments, such as the Planck space observatory, which currently provides the most accurate measurement. Conducting an evolved analysis of the CMB power spectrum provides information about the density fluctuations at the moment of recombination. The presence of dark matter affects this pattern. Since dark matter is electrically neutral, it can already cluster at times when electrons and nuclei are still ionized. The presence of such overdense regions of clustered dark matter changes the density oscillation in a characteristic way. The relic abundance can be inferred from the imprints in the CMB fluctuations.

6.2 Thermal Freeze-Out

In the course of this study we assume that the observed abundance dark matter is a thermal relic. The idea of thermal freeze-out is one of the most considered approaches to explain the observed relic abundance of dark matter. The main idea of this approach is sketched in the following. In the early universe, shortly after the Big Bang the average energy density was high enough for SM particles and heavy NP particles to exist in a thermal equilibrium. SM particles constantly annihilate into NP particles and vice versa. The leading process of mutual annihilation of DM particles and SM quarks into each other is shown as an example for this process in Figure 6.1. The state of thermal equilibrium between DM and SM particles elegantly explains an otherwise remarkable coincidence—the similar order of magnitude of DM and SM energy density. If no connection between the two sectors was present, we would in general not expect any correlation at all. In principle we could not be surprised if one sector would dominate the other by hundreds of orders of magnitude. Yet in the case of a thermal equilibrium in the early universe, a similar order of magnitude can be expected.

Due to the expansion of the universe, the temperature continuously drops. Once the average temperature drops below the mass of the heavier particles, the annihilation process only continues to run in one direction. If possible, the remaining heavier particles will then decay. In our model this is the case for the heavy mediator ϕ . They can directly decay into a dark matter flavour and a SM quark flavour, via the NP DM-quark interaction in (3.1). The same is true for the heavier dark matter flavours, which can decay into the lighter flavours.

The other possibility is that the heavy particle can no longer decay, since it is stable due to some protecting symmetry. In our model this is the case for the lightest dark matter flavour. The only possible process to deplete the equilibrium density of the dark matter flavour is pair annihilation. The tree-level mode is t-channel exchange of the mediator ϕ , see Figure 6.1. The DM particles continuously annihilate into SM quarks, depleting the population.

As the population continuously drops, the universe continues to expand. Both these processes lead to a continuous decrease in the average number density of DM particles. Due to those two processes the chance for two dark matter particles to meet and annihilate at some point (roughly when the temperature drops below a critical value $T_f \approx m_\chi/20$) effectively vanishes, resulting in a constant number of remaining DM particles. Their number density will of course continue to drop (in average), due to the ongoing expansion of the universe. Yet their relative density compared to SM particles remains constant. This process is known as thermal freeze-out.

To be precise, the freeze-out is an asymptotic process, never fully completed. Especially in overdense regions, e.g. galaxies and even more so galaxy cores, the annihilation process to some degree continues until today. Such present-day annihilation might be detected in indirect searches, see the discussion in Section 6.4.

The resulting number density of the dark matter relic depends on the cross section of the annihilation process. If the cross section is too large, the DM population will be depleted too fast and we would predict less than the observed relic abundance. If the cross section is too low, we predict more relic dark matter than observed. We need just the right cross section to reproduce the correct relic abundance.

Remarkably, the entire process of freeze-out throughout the history of the universe can be traced and the resulting mass density can be calculated in terms of the cross section. In [64] the authors made a sophisticated analysis of this evolution. They find that for DM masses below 10 GeV the dependence between the resulting relic density at present time and the thermally averaged annihilation rate factor (“cross section”) $\langle\sigma v\rangle$ is quite irregular. However, for DM masses $\gtrsim 10$ GeV the connection

$$10^{27} \langle\sigma v\rangle \Omega h^2 = 2.1 - 0.3 \log \Omega h^2 \quad (6.1)$$

between the cross section $\langle\sigma v\rangle$ and the relic abundance of DM Ωh^2 holds to 5% precision. Using the measured relic abundance, we can use (6.1) to determine the necessary value for the cross section. The currently most precise value for Ωh^2 has been measured by the Planck collaboration [9]:

$$\Omega h^2 \approx 0.12. \quad (6.2)$$

This results in a necessary cross section of

$$\langle\sigma v\rangle \approx 2.0 \cdot 10^{-26} \text{ cm}^3/\text{s}. \quad (6.3)$$

The original prediction from 2012 in [64] was $\langle\sigma v\rangle \approx 2.2 \cdot 10^{-26} \text{ cm}^3/\text{s}$. The updated measurement of the relic abundance from Planck changed this by approximately 10%. In addition, we already mentioned an approximate 5% uncertainty from the population evolution, depending on the DM mass. Considering those uncertainties, we will require the calculated value for $\langle\sigma v\rangle$ to match the value in (6.3) within a 10% tolerance range. This tolerance range does not qualitatively affect the phenomenology and furthermore simplifies the numerical analysis.

In principle, the upper bound on the annihilation cross section can be relaxed. Assuming that the DM candidate of our model does not make up for all the DM relic abundance, allows for higher cross sections. Nevertheless, the lower bound is indisputable, since we cannot justify a model predicting a larger relic abundance than is observed. For the course of this study we assume that our DM candidate makes up for the entire relic. The possibility of relaxing this constraint is discussed in more detail in Subsection 8.1.3.

To determine the impact of the relic abundance constraint on our model, we need to calculate the annihilation cross section generated by the process in Figure 6.1. In contrast to the formula derived in [25], we cannot neglect the masses of all quarks compared to the DM mass, due to the large top-quark mass. Hence, we need to include the phase space factors properly. Using the procedure in [65] we derive the overall averaged annihilation cross section formula as

$$\langle\sigma v\rangle_{\text{eff}} = \frac{1}{18} \cdot \frac{3}{32\pi} \cdot \frac{1}{4} \sum_{i,j=1}^3 \sum_{k,l=u,c,t} |\lambda_{ki}|^2 |\lambda_{lj}|^2 \frac{\sqrt{(4m_\chi^2 - (m_k - m_l)^2)(4m_\chi^2 - (m_k + m_l)^2)}}{\left(m_\phi^2 + m_\chi^2 - \frac{m_k^2}{2} - \frac{m_l^2}{2}\right)^2}. \quad (6.4)$$

Here $m_{k,l}$ are the masses of the final state quarks. Since we are considering a Dirac fermion as dark matter, we converted the result into an effective cross section. Hence, we had to include a factor of 1/2 [66,67].

The formula (6.4) includes a factor of 1/9 from averaging over all combinations of dark matter flavours in the initial state. This formula hence assumes that all DM flavours are present during the freeze-out, which is not necessarily the case. If the flavours are sufficiently split in mass, the heavier flavours have already decayed when the lightest flavour, i.e. the dark matter candidate, freezes out. For more details on the decay of heavier flavours see Appendix D of [25]. Furthermore, (6.4) assumes that the decay channels into all quark flavours are open. Since we consider dark matter masses as low as 10 GeV, final states including top-quarks might be kinematically forbidden, which leads to a modification of the formula. The different scenarios and limits of the formula are discussed in more detail in the next section.

6.3 Scenarios and Limits

We will now take a more detailed look at the different freeze-out scenarios. To understand the different scenarios we need to review the mass-splitting effects in DMFV. As discussed

in Section 3.4 the non-universality of the coupling matrix λ gives rise to the mass-splitting between the DM flavours χ_i in the following form:

$$m_{\chi,ij} = m_\chi \left(\mathbf{1} + \eta \lambda^\dagger \lambda + \mathcal{O}(\lambda^4) \right)_{ij} = m_\chi \left(1 + \eta (D_{\lambda,ii})^2 + \mathcal{O}(\lambda^4) \right) \delta_{ij}. \quad (6.5)$$

with η taken as a free parameter in our simplified model. As mentioned before, the freeze-out takes place when the temperature drops below the critical value $T_f \approx m_\chi/20$. For different masses m_{χ_i} , the freeze-out hence occurs at different temperatures $T_{f,i} \approx m_{\chi_i}/20$. A derivation for this relation can be found in [68]. If the mass-splitting between the flavours is negligible compared to the freeze-out temperatures they will effectively all freeze out together and co-annihilation between the different DM flavours is present—as was included in (6.4). If on the other hand there is a significant splitting, the lightest flavour(s) will effectively freeze out alone. By the time this freeze-out happens, the heavy/heavier flavour(s) have already decayed and only the lightest flavour(s) can (co-)annihilate. Hence the first sum in (6.4) will only run over the DM flavour(s) present and the averaging factor has to be adapted.

Even if the mass-splitting is ever so small and multiple flavours are present at the freeze-out, the heavier flavours are expected to completely decay into the DM candidate eventually. The present relic abundance of dark matter will only consist of the lightest DM flavour. Since the mass-splitting in this case is insignificant, this process will not affect the dark matter relic abundance in any relevant way.

As mentioned before, the combined analysis favours the case of top-flavoured dark matter. Hence, we focus on this dark matter candidate for the course of this analysis. As we can see from (6.5), the corrected mass value for a DM flavour χ_i is determined by the coupling $D_{\lambda,ii}$ and η . The LHC constraints discussed in Chapter 4 prefer $D_{\lambda,33}$ to be the largest coupling. Hence, to ensure the top-flavour as the lightest flavour, we choose a negative η for this analysis.

We now discuss two benchmark cases in detail:

- For the **quasi-degenerate freeze-out (QDF)** scenario we require all DM flavours to freeze out together. Their mass-splitting has to be significantly smaller than the freeze-out temperature T_f . To ensure this we demand a splitting below 1%. To make such a small splitting likely to happen, we fix $\eta = -0.01$, which is the smallest justifiable magnitude. Larger absolute values of η will cause a more stringent effect on the couplings, but not change our findings qualitatively.
- For the **single flavour freeze-out (SFF)** we require the top-flavour to be significantly split from the other flavours and hence be the only flavour present at the time of the final DM freeze-out. For this to happen, we demand the mass-splitting to be at least 10% relative to the other flavours. To make such a large splitting likely to happen, we set $\eta = -0.075$, which is the largest absolute value, which even for the maximum value of $D_{\lambda,ii} \leq 2.0$ is consistent with mass corrections of at most 30 %, see (3.23).

Of course there is also the possibility of two-flavour freeze-out. We do not discuss this possibility in detail, since most of its properties can be inferred from what we learn by studying the QDF and SFF scenarios.

6.3.1 Quasi-degenerate Freeze-Out

For this scenario to take place, the mass-splitting between the three DM flavours has to be sufficiently small. As discussed before, we require a splitting below 1%. Since the couplings $D_{\lambda,ii}$ govern the mass-splitting, we hence need to impose constraints on the coupling to accomplish QDF. Since we also demand top-flavoured dark matter and choose a negative η , we get the following upper and lower limits for $D_{\lambda,11}$ and $D_{\lambda,22}$ in terms of $D_{\lambda,33}$:

$$\sqrt{\frac{D_{\lambda,33}^2 - \frac{0.01}{|\eta|}}{0.99}} \leq D_{\lambda,11}, D_{\lambda,22} < D_{\lambda,33}, \quad (6.6)$$

For a third generation coupling $D_{\lambda,33}^2 \leq \frac{0.01}{|\eta|}$ the lower bound on the other couplings is zero.

For the cross section formula we need to distinguish three different DM mass ranges:

- $m_{\chi_t} \geq m_t$: The DM particles are sufficiently heavy to annihilate in all combinations of quark flavours in the final state. Hence, (6.4) is the correct formula.
- $\frac{m_t}{2} \leq m_{\chi_t} < m_t$: The final state with two top-quarks is kinematically forbidden and hence needs to be excluded from formula (6.4).
- $m_{\chi_t} < \frac{m_t}{2}$: We need to exclude any final state with top-quarks from formula (6.4).

Please note that m_{χ_t} here is the mass of the top-flavour after the corrections from (6.5). Strictly speaking there can be cases where m_{χ_t} already dropped below one of the thresholds, yet m_{χ_u} and/or m_{χ_c} are still above and some of the initial state combinations still allow for top-quark final states, which are excluded for a $\chi_t \bar{\chi}_t$ initial state. We ignore such details in the analysis. For simplification, we furthermore ignore the mass-splitting of the dark matter flavours in the numerical evaluation of the formula. This results in a negligible error, since the QDF scenario requires splittings below the percent level and we only apply the experimental value in (6.3) up to a 10% tolerance range. Last but not least, we neglect the relatively small up-quark and charm-quark mass relative to the DM mass of at least 10 GeV. For the numerical analysis we use $(m_u, m_c, m_t) = (0, 0, 173.5 \text{ GeV})$ [42].

To understand the effect of the relic abundance constraint on this scenario, let us look in more detail at (6.4). In the limit of $m_\chi \gg m_t$ we can neglect the phase space factors, leading to a significant simplification of the formula:

$$\langle \sigma v \rangle_{\text{eff}} = \frac{1}{18} \cdot \frac{3}{32\pi} \sum_{i,j=1,2,3} \frac{D_{\lambda,ii}^2 D_{\lambda,jj}^2 \cdot m_\chi^2}{(m_\phi^2 + m_\chi^2)^2}. \quad (6.7)$$

Imposing the relic abundance constraint (6.3) for fixed DM mass m_χ and mediator mass m_ϕ then effectively results in a spherical constraint on the three couplings, i.e.

$$D_{\lambda,11}^2 + D_{\lambda,22}^2 + D_{\lambda,33}^2 = \text{const.} \quad (6.8)$$

Since we have $D_{\lambda,ii} \geq 0$, we are limited to 1/8 of the surface of the sphere defined by (6.8). Furthermore, the constraints $D_{\lambda,ii} \leq 2.0$ cut out part of the remaining shell. The bounds (6.6) further restrain the valid area. For non-negligible phase space factors we do not have the nice simplified form (6.7), but have dependences on the mixing angles. This deforms the shell of valid points. Since we impose the relic abundance constraint only up to a 10% tolerance interval, we expect a valid area which is part of such a deformed shell with finite thickness in the $D_{\lambda,11} - D_{\lambda,22} - D_{\lambda,33}$ space.

In Figure 6.2 we can see the valid area with imposed relic abundance constraint for fixed mediator mass $m_\phi = 850$ GeV and various DM masses. In Figure 6.2b we clearly see the lower and upper bounds on the coupling $D_{\lambda,11}$ in terms of $D_{\lambda,33}$. Since we picked $m_u = m_c = 0$ the valid areas in the $D_{\lambda,22} - D_{\lambda,33}$ plane look just the same as in the $D_{\lambda,11} - D_{\lambda,33}$ plane. This symmetry can also clearly be seen in Figure 6.2a.

In addition to the constraints from imposing QDF, we can also observe the allowed areas varying in dependence of the DM mass. Lower DM mass results in a viable area at higher average couplings. This comes as no surprise, since both couplings and the DM mass are in the numerator of the cross section formula. For fixed mediator mass a lower DM mass demands higher couplings to still fulfill the relic abundance constraint.

Once the DM mass drops below the top-quark mass the valid area shifts more significantly with the DM mass. The reason for this is the changed influence on the couplings, since the valid decay channels are limited and hence the number of contributing terms decreases. The couplings have to be even larger to compensate for this. We can see that for sufficiently low DM mass the couplings have to take values in the range of 2.0. As discussed before, both the collider and the direct detection constraints demand a reasonable upper bound on the couplings. We limit ourselves to $D_{\lambda,ii} \leq 2.0$ in this study. Hence, we see that the relic abundance constraint results in a lower bound on the DM mass, depending on the mediator mass. This lower bound is a consequence of the combination of constraints.

The phases δ_{ij} have no influence on the cross section and the flavour mixing angles θ_{ij} have little influence in the QDF scenario for most DM masses.

6.3.2 Single Flavour Freeze-Out

For the single flavour freeze-out (SFF) to happen, we need a significant mass-splitting between the lightest flavour and the other DM flavours. We require at least 10% splitting and demand the top-flavour as dark matter relic. This results in the following bounds for $D_{\lambda,11}$ and $D_{\lambda,22}$ in terms of $D_{\lambda,33}$:

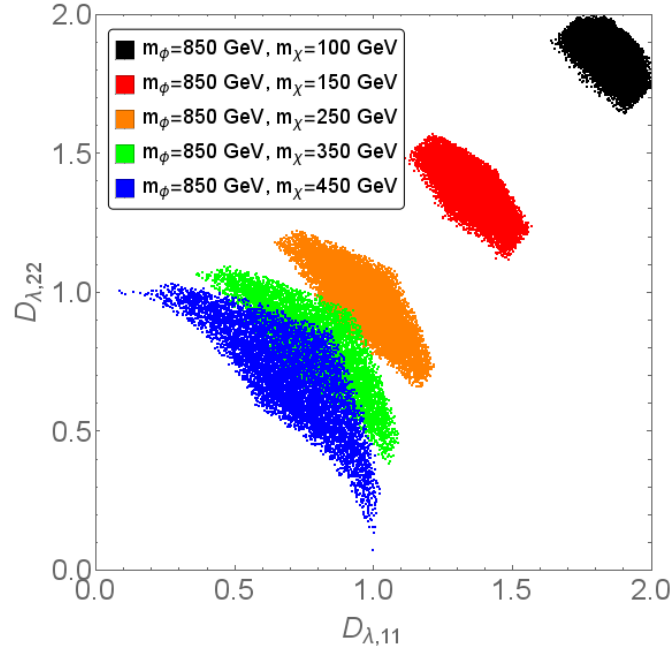
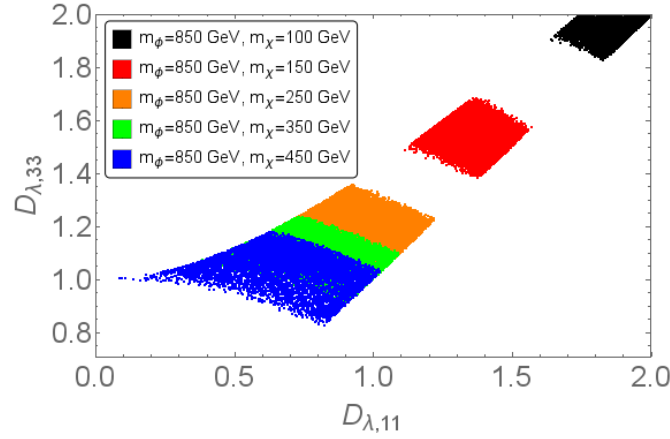
(a) Allowed areas in the $D_{\lambda,11}$ - $D_{\lambda,22}$ plane.(b) Allowed areas in the $D_{\lambda,11}$ - $D_{\lambda,33}$ plane.

Figure 6.2: Valid regions of parameter space in the QDF scenario (with $\eta = -0.01$) compatible with the relic abundance constraint, at different DM masses.

$$D_{\lambda,11}, D_{\lambda,22} < \sqrt{\frac{D_{\lambda,33}^2 - \frac{0.1}{|\eta|}}{0.9}}. \quad (6.9)$$

For too low third generation coupling, i.e. $D_{\lambda,33}^2 < \frac{0.1}{|\eta|}$ those bounds can not be fulfilled. This means that for SFF to occur we need a sufficiently high $D_{\lambda,33}$ depending on the value of η . As discussed, we fix $\eta = -0.075$ in this analysis. Compared to the QDF scenario, we

need to modify the cross section formula, including only the $\chi_t \bar{\chi}_t$ initial state. The formula then reads:

$$\langle \sigma v \rangle_{\text{eff}} = \frac{1}{2} \cdot \frac{3}{32\pi} \cdot \frac{1}{4} \sum_{k,l=u,c,t} |\lambda_{k3}|^2 |\lambda_{l3}|^2 \frac{\sqrt{(4m_{\chi_t}^2 - (m_k - m_l)^2)(4m_{\chi_t}^2 - (m_k + m_l)^2)}}{\left(m_\phi^2 + m_{\chi_t}^2 - \frac{m_k^2}{2} - \frac{m_l^2}{2}\right)^2}. \quad (6.10)$$

Since we no longer average over the initial states, there are less terms and no averaging factor $1/9$. The only parameters (apart from the masses) that remain in the cross section formula are $D_{\lambda,33}$, θ_{13} and θ_{23} . Hence the influence of the reduced number of parameters on the cross section is more significant than before.

We have to distinguish the same three DM mass ranges as in the QDF scenario. Once the mass drops below a threshold the number of terms drops even further and hence the influence of the parameters becomes even more significant.

In Figure 6.3 we can see the valid areas of mixing angles in terms of $D_{\lambda,33}$ for fixed mediator mass $m_\phi = 850$ GeV and two different dark matter mass parameters. In Figure 6.3a we observe a connected area of allowed couplings $D_{\lambda,33}$ valid for the relic abundance constraint in the case of $m_\chi = 220$ GeV. For the lowest allowed $D_{\lambda,33}$ high values of the mixing angles are necessary to achieve a large enough cross section to reach the lower limit of the tolerance interval. As $D_{\lambda,33}$ increases the entire range of couplings becomes valid, without violating the relic abundance constraint. At this point we should remember that we show the valid values without fixed other parameters, so no correlation between the two mixing angles θ_{13} and θ_{23} is visible in the diagram. For yet even larger values of the coupling $D_{\lambda,33}$ the highest coupling values become excluded, since they result in a cross section exceeding the bounds. The upper bound on the couplings continuously decreases with increasing coupling.

Yet, at some point the upper bound suddenly relaxes. From this point on the upper bounds constantly increases with increasing coupling. The reason for this turn-around is the phase space factor in (6.10). We need to remember that $m_\chi = 220$ GeV for this scan is the uncorrected mass parameter. With increasing $D_{\lambda,33}$ the corrected top-flavour DM mass m_{χ_t} decreases, approaching the top-quark mass. If m_{χ_t} becomes sufficiently close to the top-quark mass the phase space suppression of those final state terms becomes effectively more significant than the enhancement of the other terms, which are hence allowed to take larger values without violating the relic abundance constraint. This explains why in this range of $D_{\lambda,33}$ the upper bound continuously relaxes with increasing coupling.

When the corrected mass m_{χ_t} reaches the top-quark mass and drops below it, the final state with two top-quarks no longer contributes to the formula. From this point on increasing $D_{\lambda,33}$ only increases all present terms and hence again demands decreasing mixing angles. In Figure 6.3a we can observe this as a clear kink in the upper bound at $D_{\lambda,33} \approx 1.7$.

An analogous pattern can be observed in Figure 6.3b for $m_\chi = 230$ GeV. Yet due to the larger dark matter mass parameter there is an interval of $D_{\lambda,33}$ values where even the lowest values of the mixing angles can not push down the cross section far enough to be in agreement with the relic abundance constraint. Only when the phase space factor suppression effect

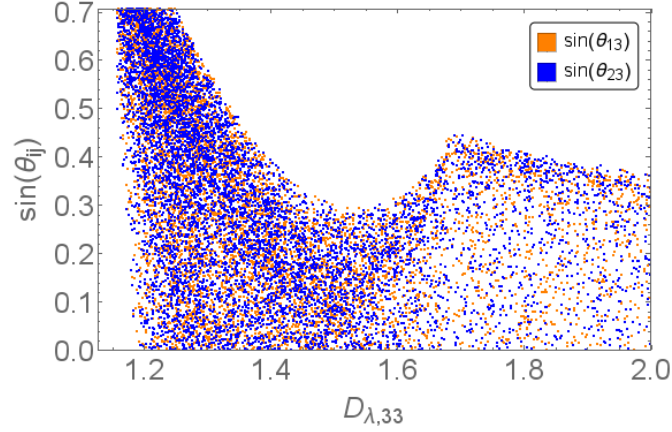
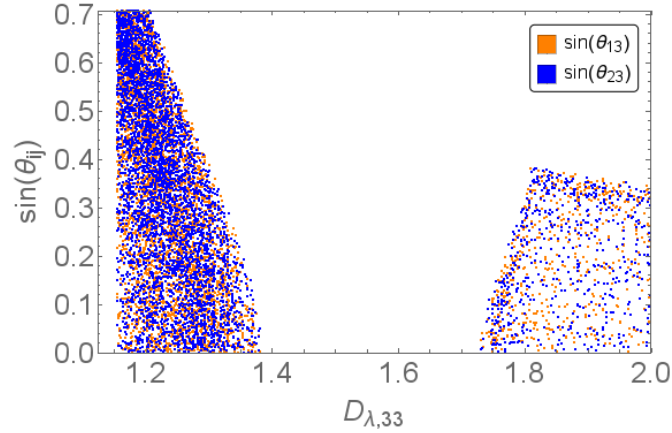
(a) Valid areas for $m_\chi = 220$ GeV.(b) Valid areas for $m_\chi = 230$ GeV.

Figure 6.3: Allowed ranges for the flavour mixing angles in dependence on $D_{\lambda,33}$, for SFF scenario (with $\eta = -0.075$) at $m_\phi = 850$ GeV. Different colours correspond to the different mixing angles θ_{ij} : $ij = 13$ in orange, $ij = 23$ in blue.

kicks in, we can find valid points again. This leads to a disconnected valid area for $D_{\lambda,33}$.

In terms of mass bounds we rediscover the same effect as in QDF. Too low DM masses demand couplings exceeding 2.0 and hence are excluded. Yet, we observe an additional effect. As discussed, we also have a lower bound on the coupling $D_{\lambda,33}$ to guarantee SFF. Hence, we also experience an upper bound on the dark matter mass. Figure 6.4 shows the valid area in the $m_\phi - m_{\chi_t}$ plane for SFF with fixed $\eta = -0.075$. In the figure we show the corrected DM mass m_{χ_t} . We can clearly observe the lower as well as an upper bound on the DM mass. The upper bound on m_{χ_t} depends on the lower bound for $D_{\lambda,33}$ and hence on the parameter η . By allowing for larger absolute values of η , we can significantly relax this bound. Yet a larger absolute value of η would exclude larger couplings, since it would otherwise lead to violation of our convergence constraint (3.23). This would effectively lead to an increased lower bound in the DM mass. Hence, Figure 6.4 served to give a qualitative understanding of the general situation. In summary, SFF is only possible for a valid interval

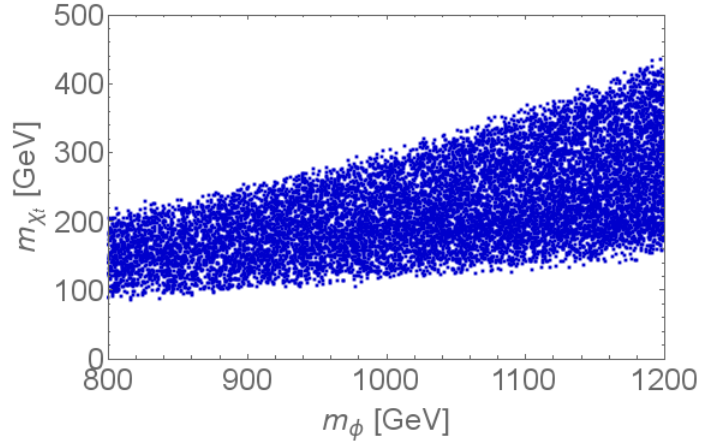


Figure 6.4: Valid DM mass ranges in dependence on m_ϕ for SFF (at fixed $\eta = -0.075$) with relic abundance constraint applied. We observe both a lower and upper bound on the DM mass.

of DM masses in terms of the mediator mass and η .

6.4 Remarks on Constraints from Indirect Detection

At this point, it is time for some remarks on indirect detection. As already mentioned before, the process of DM annihilation can still take place today, especially in overdense regions such as the galactic center. The products of this annihilation process might be detected as an excess in e.g. the anti-proton flux. Due to the significant uncertainties associated with the assumed propagation model, we did not include possible constraints from indirect searches in our analysis. However, using the latest AMS-02 data [69], recently quite stringent constraints on WIMP DM have been derived [70,71]. Those constraints have the potential to exclude additional parts of the considered parameter space.

Nevertheless, the impacts on our up-type DMFV model with a top-flavoured DM candidate are expected to be less significant than in the generic WIMP case. The reason lies in the multiple DM flavours. The simple relation between the annihilation cross section relevant for the relic abundance of DM and the DM annihilation happening at present time in our universe is lost if multiple flavours have been present at the freeze-out. Considering the top-flavour as a DM candidate, the pure top-flavour annihilation cross section is smaller than the average cross section, being kinematically suppressed by the large top-quark mass. This suppresses the contribution to the indirect detection signal.

A detailed analysis of these constraints is beyond the scope of this thesis and left for future studies. We note that our model can not accommodate for the hint of a ~ 80 GeV WIMP DM candidate claimed in [70]. The combination of collider and relic abundance constraints, excludes such low DM masses in our model.

6.5 Summary of Effects from Relic Abundance Constraint

Studying the impact of the relic abundance constraint on our model, we made the following observations:

- We required the annihilation cross section to have the correct value to reproduce the observed relic abundance of dark matter. For a fixed mediator mass m_ϕ and fixed coupling λ the relic abundance constraint then demands a specific DM mass m_χ . The larger the coupling, at fixed mediator mass, the smaller the DM mass has to be. An upper bound on the couplings therefore results in a lower bound on the DM mass. The exact value of this lower bound depends on the mediator mass. With increasing mediator mass, we find an increasing lower bound on the DM mass.
- To realize single flavour freeze-out, a significant splitting between the masses of the DM flavours is necessary. Such a mass-splitting demands a splitting in the couplings $D_{\lambda,ii}$, hence resulting in a lower bound on (in case of top-flavoured DM) $D_{\lambda,33}$. This lower bound translates to an upper bound on the DM mass. The exact value depends on the mediator mass, with larger values of m_ϕ resulting in an increased value of the upper bound. The lower bound on the coupling also depends on the parameter η governing the mass-splitting. A larger $|\eta|$ results in a decreased lower bound on the coupling, i.e. a relaxed upper bound on the DM mass. For more details on the influence of η see Appendix B.

Constraints from Direct Detection Experiments

Last but definitely not least, we now take a look at the bounds from direct detection experiments. The main principles of direct detection experiments are presented first, and the convenient way of presenting the current limits, i.e. as a bound on the spin-independent WIMP-nucleon cross section, is discussed. We then study the significant contributions to DM-SM scattering in the DMFV model. We discuss cancellation patterns as well as the consequences of using natural xenon as target material. Finally, implications from future direct detection experiments are discussed.

7.1 Direct Detection Experiments

The main idea of direct detection experiments is as simple as it is elegant. Since particle dark matter is supposedly present everywhere, some of the dark matter particles might every now and then scatter off some of the SM particles here on earth. Such a scattering would result in an energy deposit in the SM particle, which in principle could be detected as e.g. a heat signature. Unfortunately there are two problems, which make such a detection highly challenging. The first problem is the expected minor average relative velocity between the dark matter particles in the vicinity of earth and the earth itself. This minor velocity results in a minor recoil energy in the average DM-SM scattering. To distinguish this small energy deposit from thermal fluctuations, the target material has to be kept at very low temperature.

The second, maybe even larger challenge, is the large background. Among other things, cosmic rays, radioactive decays, even neutrinos have to be considered. Controlling and understanding this multitude of backgrounds is one of the major obstacles of direct detection experiments. To limit the cosmic ray background, most direct detection experiments are located underground.

The major direct detection experiments, which provide the currently most stringent exclusion bounds for DM masses $\mathcal{O}(50 \text{ GeV}-1 \text{ TeV})$, are using liquid xenon as a target material. To understand the typical form of the obtained exclusion bounds, we need to understand two effects. First, the cross section for scattering and the energy deposit is proportional to the reduced mass of the WIMP-nucleon system. WIMP is the abbreviation for weakly interacting massive particle, an interesting class of dark matter candidates. In the direct detection community, this term is commonly used as representative for dark matter in general, which is why we frequently adopt it in this section. For DM masses significantly above the mass of the nucleus, the reduced mass is approximately identical to the mass of the nucleus, i.e. constant. For DM masses significantly below the mass of the nucleus, the reduced mass is approximately equal to the DM mass, hence decreasing with decreasing DM mass. Hence, the recoil energy transferred to the nucleus decreases with DM mass and hence detecting such a scattering becomes increasingly hard for lower DM masses. The cross section bounds for light DM masses suffer from this effect.

The second effect we need to consider is the following. The expected event rate is proportional to the local DM number density and the cross section for WIMP-xenon scattering $\frac{dN}{dt} \sim \sigma_{Xe} \cdot n$. Since the average local DM mass density ρ is known, the number density is inverse proportional to the DM mass, $n = \rho/m_\chi$. For increased DM mass we hence expect a lower number density and hence a smaller number of events for a fixed cross section. In consequence, the cross section bound, which can be inferred from the lack of any signal events is less stringent for larger DM masses.

For small DM masses the effect from the reduced recoil energy dominates, resulting in weak bounds on the cross section. The strongest exclusion bound is typically achieved in the range of $m_\chi \approx 50 \text{ GeV}$. For larger DM masses the effect from decreased number density dominates, the upper bound on the cross section increasing approximately proportional to the DM mass.

The inferred experimental bounds are typically provided in form of bounds on the so-called spin-independent WIMP-nucleon cross section σ_n^{SI} . This bound is inferred from the WIMP-xenon cross σ_{Xe} section bound, by assuming a spin-independent coupling of the WIMP and equally strong coupling to protons and neutrons. Neglecting the small mass-splitting between proton and neutron, we then have $\sigma_n^{SI} = \frac{\sigma_{Xe}}{A^2}$, with A being the average xenon mass number.

7.2 WIMP-Nucleon Scattering

To understand the constraints from direct detection experiments on WIMP-nucleon scattering, we first need to discuss the relevant processes. We use the derivation in [17] and the adaption to the down-quark DMFV model in [25] to derive the contributions for our model. All relevant contributions are depicted in Figure 7.1 for our choice of the top-flavour as dark matter relic. The dark matter of our model couples to the up-quarks in the protons and neutrons. The leading-order scattering between χ_t and up-quarks is the tree-level s-channel ϕ exchange diagram, followed by the box diagram contribution. Apart from direct scattering off the up-quarks, we also need to include the photon-penguin with the proton

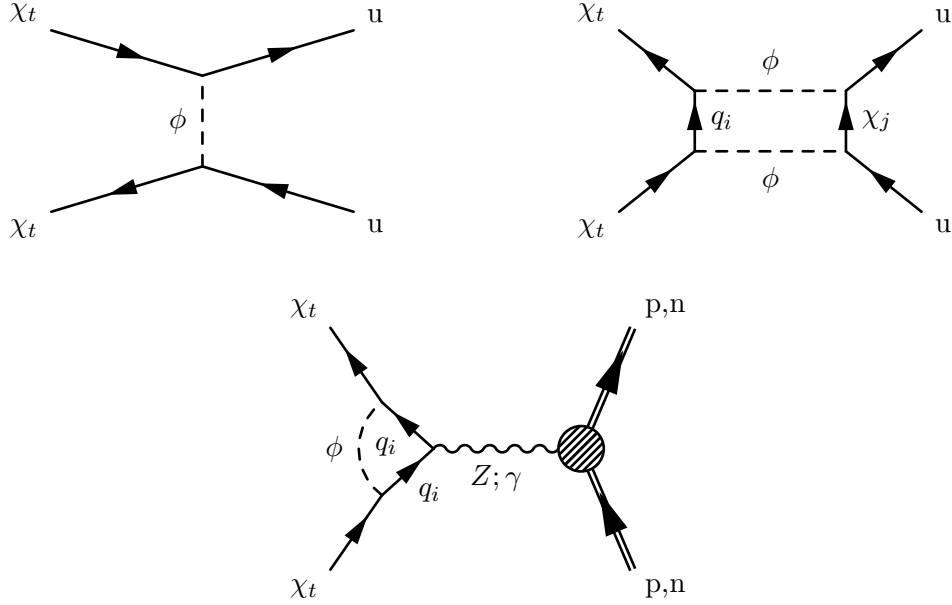


Figure 7.1: Feynman diagrams of relevant processes contributing to DM-nucleon scattering.

as well as the Z-penguins with both proton and neutron. Since the recoil energy in such a DM scattering is $\lesssim 100$ keV [72], both the photon and the Z-boson couple to the nuclei without probing their substructure, which allows us to treat the interaction as point-like. The Z-penguin is relevant due to the large top-quark mass—as opposed to the down-quark DMFV model. Contributions from both Higgs and gluon exchange have been found to be negligible in [73].

Due to the different charges and number of valence up-quarks, the DM will couple differently to protons and neutrons, parametrized by f_p and f_n respectively in the following analysis. The spin-independent WIMP-nucleon cross section, for a nucleus with mass number A and atomic number Z , is given as

$$\sigma_n^{SI} = \frac{\mu_n^2}{\pi A^2} |Z f_p + (A - Z) f_n|^2, \quad (7.1)$$

with μ_n being the reduced mass of the WIMP-nucleon system. The processes in Figure 7.1 result in the following respective contributions to f_p and f_n :

- The tree-level s -channel ϕ exchange between DM and up-quarks contributes:

$$f_p^{\text{tree}} = 2f_n^{\text{tree}} = \frac{|\lambda_{ut}|^2}{4m_\phi^2}. \quad (7.2)$$

- The box-diagram is given as

$$f_p^{\text{box}} = 2f_n^{\text{box}} = \sum_{i,j} \frac{|\lambda_{ui}|^2 |\lambda_{jt}|^2}{32\pi^2 m_\phi^2} L\left(\frac{m_{q_i}^2}{m_\phi^2}, \frac{m_{\chi_j}^2}{m_\phi^2}\right), \quad (7.3)$$

with L being the same loop function as in the D-meson mixing, defined in Equation 5.4.

- Since the neutron is electrically neutral, we only find a photon penguin contribution to f_p :

$$f_p^{\text{photon}} = - \sum_i \frac{|\lambda_{it}|^2 e^2}{48\pi^2 m_\phi^2} \left[\frac{3}{2} + \log\left(\frac{m_{q_i}^2}{m_\phi^2}\right) \right] \quad (7.4)$$

- Finally, the contributions of Z penguin diagrams are:

$$f_p^Z = - \frac{3|\lambda_{tt}|^2 e^2 \left(\frac{1}{2} - 2\sin^2\theta_W\right) m_t^2}{32\pi^2 \sin^2\theta_W \cos^2\theta_W m_Z^2 m_\phi^2} \left[1 + \log\left(\frac{m_t^2}{m_\phi^2}\right) \right], \quad (7.5)$$

$$f_n^Z = - \frac{3|\lambda_{tt}|^2 e^2 \left(-\frac{1}{2}\right) m_t^2}{32\pi^2 \sin^2\theta_W \cos^2\theta_W m_Z^2 m_\phi^2} \left[1 + \log\left(\frac{m_t^2}{m_\phi^2}\right) \right], \quad (7.6)$$

with the weak mixing angle θ_W . The Z -penguin contributions are proportional to m_q^2/m_ϕ^2 and hence significantly suppressed, except for a top-quark in the loop. Only in the latter case we find a non-negligible contribution. This is why we only show the contribution with top-quark in the loop.

In this analysis we omit effects from RG running. Those have been calculated in [74]. The authors of [75] studied the same model as we did in [35], including RG running effects in the direct detection formula. Those effects alter the relative couplings to the different quark flavours, hence enhancing tree-level coupling to up-quarks even in the case of the dark matter relic coupling primarily to heavier quarks. In spite of the RG running corrections the top-flavoured DM case remains the favoured scenario. The authors of [75] reproduce our results, yet claim that the RG running effects slightly weaken our case for top-flavoured DM. As a consequence they also explore the case of charm-flavoured DM.

7.3 Phenomenology

7.3.1 Cancellation Pattern of Contributions

The combination of all contributions in (7.1) has to result in a cross section which is below the current bounds. The strongest bounds for the spin-independent WIMP-nucleon cross section in the considered dark matter mass range are currently provided by the LUX [76],

PandaX-II [77] and XENON1T [78] collaborations. In the future the bounds will be improved by both existing as well as upcoming experiments, such as XENONnT [79], LUX-ZEPLIN (LZ) [80] and DARWIN [81]. In the analysis, we use the current XENON1T exclusion bounds provided in [78], as a representative of the state of the art.

To understand the impact of the direct detection constraints on our model, we need to take a closer look at the multitude of contributing terms. Our first observation is that—considering the parametrization of the NP DM-quark coupling λ given in (3.10)—all the terms in both f_p and f_n are proportional to $(D_{\lambda,33})^2$. This is a consequence of our choice of top-flavoured dark matter. In the cross section formula we hence have an overall factor of $(D_{\lambda,33})^4$. A sufficiently small third generation coupling can therefore be enough to suppress the expected direct detection signal below all exclusion bounds.

If the coupling $D_{\lambda,33}$ is too large to suppress the cross section sufficiently, achieving a small cross section gets more complicated. Especially the tree-level contribution causes a serious problem already for reasonably small coupling $D_{\lambda,33}$. In addition we find that nearly all other processes only add to this contribution, since they are also positive. There is only one exception, namely the Z-penguin with the neutron. To achieve a sufficiently low cross section, a destructive interference between the sum of contributions is necessary. Since all other contributions are loop-suppressed, the tree-level diagram is for small $D_{\lambda,33}$ generically by far the largest positive contribution. Therefore, the negative neutron Z-penguin will have to cancel mainly this tree-level contribution. The two contributions are given as

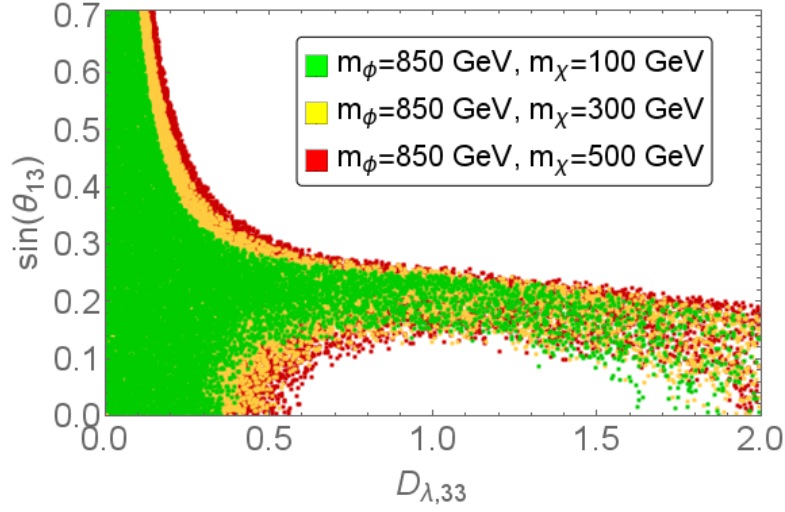
$$A^{tree} = \mathcal{A}_I \cdot \sin^2 \theta_{13} \cdot D_{\lambda,33}^2, \quad (7.7)$$

$$A_n^Z = \mathcal{A}_{II} \cdot \cos^2 \theta_{13} \cdot \cos^2 \theta_{23} \cdot D_{\lambda,33}^2, \quad (7.8)$$

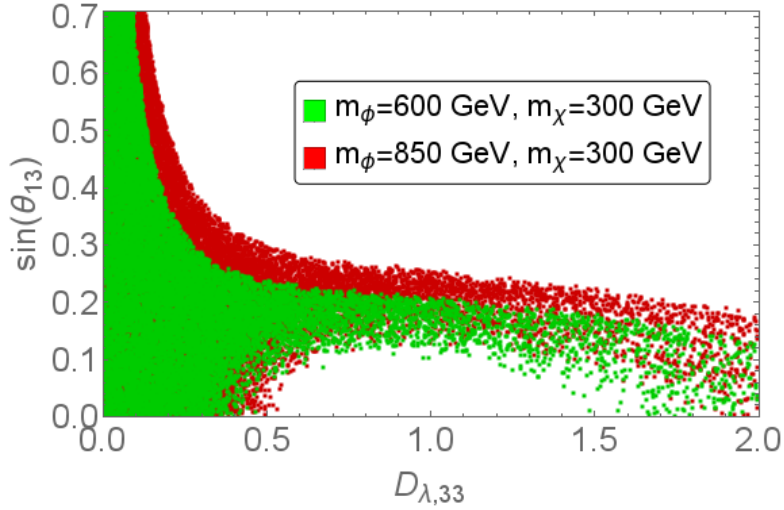
with \mathcal{A}_I and \mathcal{A}_{II} including all constants and the dependence on the mediator mass m_ϕ . We can see that both terms have the same dependence on $D_{\lambda,33}$. Hence, for a fixed mediator mass, the cancellation between the two terms is governed by the two flavour mixing angles θ_{13} and θ_{23} . Increasing θ_{13} at the same time increases the tree-level process and decreases (in magnitude) the Z-penguin. θ_{23} can tune the magnitude of the Z-penguin independently of the tree-level process.

Figure 7.2a shows the valid area in the $D_{\lambda,33} - \theta_{13}$ plane for fixed mediator mass and different values of the DM mass. To guarantee a top-flavoured DM relic we imposed the constraints of the QDF freeze-out scenario, discussed in Subsection 6.3.1. Those constraints on the couplings $D_{\lambda,11}$ and $D_{\lambda,22}$ have only small impact on the observed phenomenology. We choose the QDF scenario over the SFF scenario (see Subsection 6.3.2), since the lower bound on $D_{\lambda,33}$ would already exclude a large portion of the interesting parameter space. For the remaining parameter space the implications of direct detection constraints are basically the same as in the QDF scenario.

We observe that for sufficiently small $D_{\lambda,33}$ all mixing angles θ_{13} are allowed, as expected. For increasing $D_{\lambda,33}$ we see the effects of the necessary cancellation. A large θ_{13} becomes forbidden, since they result in a too large tree-level contribution, while suppressing the negative neutron Z-penguin. At the same time, too small θ_{13} is also invalid. Although the



(a) Valid ranges of flavour mixing angle θ_{13} as function of $D_{\lambda,33}$ at various values of m_χ and fixed m_ϕ (in QDF).



(b) Valid ranges of flavour mixing angle θ_{13} as function of $D_{\lambda,33}$ for various values of m_ϕ and fixed m_χ (in QDF).

Figure 7.2: Constraints on the flavour mixing angle θ_{13} with current XENON1T direct detection bounds applied [78].

tree-level contribution is suppressed for such small θ_{13} , the Z-penguin will be too large, leading again to a too large cross section. What we observe is a valid interval of θ_{13} values. In this interval the cancellation between tree-level and neutron Z-penguin (as well as all the other positive contributions) suppresses the cross section sufficiently. Since the cancellation does not have to be perfect, we observe a valid band and not just a line. Furthermore the influence of θ_{23} on the Z-penguin also relaxes the bounds on θ_{13} .

For yet even larger couplings $D_{\lambda,33}$ the situation gets more complex. The box-diagram

contribution is proportional to $D_{\lambda,ii}^2 D_{\lambda,jj}^2$ and hence becomes competitive to the tree-level contribution for sufficiently large couplings. The neutron Z-penguin hence has to cancel both large positive contributions. This shifts the valid band of θ_{13} in favour of smaller mixing, which result in a more complete suppression of the tree-level process and an enhanced Z-penguin. For even larger couplings the necessary cancellation becomes impossible since the box-diagrams increases more rapidly with $D_{\lambda,33}$ than the Z-penguin. Hence, the direct detection constraint results in an upper bound on the couplings $D_{\lambda,ii}$. This bound on $D_{\lambda,33}$ can not be observed in Figure 7.2a, since we are limited to $D_{\lambda,33} < 2.0$. For a more detailed discussion of couplings exceeding 2.0 see Appendix A.

The discussed cancellation is clearly favoured in the case of top-flavoured relic DM. As we can see from the parametrization of λ in (3.10), the top-flavour as DM relic enables a naturally large coupling to the top-quark. This results in a naturally large Z-penguin contribution (which is only relevant for a top-quark in the loop). At the same time it is possible to arbitrarily suppress the tree-level process with a low mixing angle θ_{13} , enabling a sufficient cancellation even for large values of $D_{\lambda,33}$. Nevertheless, it is true that the discussed cancellation pattern is not completely impossible for charm-flavoured relic DM or even up-flavoured relic DM. The top-flavour is simply the choice which allows for the largest valid parameter space, which is why we choose it for this analysis. Our aim is to show the scenario which is least constrained. For more details on the case of charm-flavoured relic DM see [75].

In Figure 7.2a we can also see the impact of different dark matter mass parameters m_χ on the valid area. For DM mass above approximately 50 GeV, the direct detection bound relaxes with higher DM mass, as explained in Section 7.1. Hence the constraints are not as stringent and we find larger valid areas. The range of $D_{\lambda,33}$, for which all values of the mixing angle θ_{13} are valid, extends further for higher masses. Furthermore for higher masses the valid interval of θ_{13} bends slower to lower values, ultimately allowing larger couplings $D_{\lambda,33}$.

In Figure 7.2b we can see the influence of different mediator masses at fixed DM mass. So far we only mentioned the overall factor of $D_{\lambda,33}^4$ in the cross section. In addition we have an overall factor of $1/(m_\phi)^4$. From this we can see that a large enough mediator mass is also sufficient to suppress the WIMP-nucleon cross section below the bound. Hence, an arbitrarily large mediator mass enables the model to satisfy the direct detection constraint, but violates the relic abundance constraint as discussed later (see Chapter 8 and Appendix C). We can see in the figure that for the larger mediator mass we obtain a larger valid area. In addition we observe a shift of the central value of the valid θ_{13} band. The reason for this is the different influence of the mediator mass in the different contribution. For example, compared to the tree-level process the Z-penguin involves an additional factor of $\left[1 + \log\left(\frac{m_t^2}{m_\phi^2}\right)\right]$. Hence the point of perfect cancellation between them shifts with the value of the mediator mass.

isotope	half-life	abundance ρ
^{124}Xe	stable	0.095%
^{126}Xe	stable	0.089%
^{128}Xe	stable	1.910%
^{129}Xe	stable	26.401%
^{130}Xe	stable	4.071%
^{131}Xe	stable	21.232%
^{132}Xe	stable	26.909%
^{134}Xe	stable	10.436%
^{136}Xe	2.165×10^{21} y	8.857%

Table 7.1: Half-life and natural abundance of stable and quasi-stable xenon isotopes.

7.3.2 Consequences of Natural Xenon

So far we have omitted an important detail. All xenon direct detection experiments use natural xenon as target. Xenon has nine stable or quasi-stable isotopes, see Table 7.1. Seven of those make up a significant fraction of the natural abundance and hence are highly relevant for the detection process. As discussed in detail in Section 7.1, the bound on the spin-independent WIMP-nucleon cross section is inferred from the absence of signal in the direct detection experiment. The cross section bound is calculated assuming that the cross section with every target xenon atom is equally large. Since in our model we have different coupling strengths to the proton and the neutron, it is straightforward to see that we predict different cross sections for different isotopes. To get a cross section value which can be compared with the experimental bound, we need to calculate an averaged effective WIMP-nucleon cross section for natural xenon $\sigma_{n,\text{nat-Xe}}^{SI}$. Weighting the respective cross sections $\sigma_{n,i}^{SI}$ of the isotopes i with their relative abundance ρ_i , we get

$$\sigma_{n,\text{nat-Xe}}^{SI} = \sum_{i=1}^9 \rho_i \cdot \sigma_{n,i}^{SI} = \sum_{i=1}^9 \rho_i \cdot \frac{\mu_n^2}{\pi A_i^2} |Z f_p + (A_i - Z) f_n|^2. \quad (7.9)$$

Since the only negative contribution to the amplitude is the Z-penguin, the cancellation pattern varies for different isotopes. To guarantee the absence of any signal in the experiment, the cross section with all present isotopes has to be sufficiently suppressed. A perfect suppression can only be achieved with maximally one of those isotopes. Hence, the up-quark DMFV model constitutes a concrete example of xenophobic dark matter [82]. For the down-quark DMFV model studied in [25], the authors found an analogous situation, with the difference that the negative contribution was the photon-penguin (remember that the sign of this contribution is changed due to the different electromagnetic charge of the mediator ϕ in a model coupling to down-quarks).

Although we omitted these details in Subsection 7.3.1 Figure 7.2 shows the valid areas for an analysis using the weighted effective WIMP-nucleon cross section in (7.9).

7.3.3 Effects from Future Bounds

The consequences of using natural xenon, discussed in Subsection 7.3.2, are especially interesting in light of future bounds from both the existing as well as planned direct detection experiments. In Figure 7.3 we see the valid areas in the $D_{\lambda,33} - \theta_{13}$ plane at fixed mediator and DM mass for different strength of constraints, i.e. the current XENON1T bounds [78] as well as projected bounds from XENON1T [79], XENONnT [79], LUX-ZEPLIN (LZ) [80] and DARWIN [81] respectively. We can see that the current XENON1T bounds are not strong enough to exclude any couplings $D_{\lambda,33}$ below 2.0. Yet, with increasing strength of the projected bounds more and more of the larger $D_{\lambda,33}$ values are excluded. The reason for this is straightforward. For larger couplings the cross section is less suppressed due to the overall proportionality to $(D_{\lambda,33})^4$ and hence the cancellation between the different contributions needs to be more perfect. Achieving this for all isotopes at the same time at a sufficient level becomes less likely and finally impossible. For more stringent constraints from future measurements, the point where this simultaneous suppression becomes insufficient is reached for lower $D_{\lambda,33}$ values.

The consequences of this effect can only be fully appreciated in combination with the relic abundance constraint. This will be discussed in more detail in Chapter 8.

Finally we should mention that these results make a strong case for experiments with other target materials. Due to the different mass number to atomic number ratio in different elements, an absence of signals in experiments with xenon and simultaneously in experiments with other target materials is even harder to achieve for models with such cancellation patterns. So far, for DM masses above approximately 50 GeV no experiments with other target materials reach sensitivities comparable to those of xenon experiments. Experiments such as e.g. CRESST II [83], which uses $CaWO_4$ as target material, are more sensitive in the lower DM mass ranges but not competitive to xenon detectors in the ranges we consider. Another class of direct detection experiments, such as EDELWEISS-III [84], which uses germanium as target materials, and PICO-60 [85], which uses C_3F_8 as target material, are more sensitive for DM masses above 10 GeV, but are still not competitive to xenon detectors yet. The exclusion bounds provided by those experiments are still orders of magnitudes weaker than those of xenon experiments. Still it would be interesting to conduct a combined analysis of xenon and other existing bounds, which we leave as a task for future work.

7.4 Summary of Effects from Direct Detection Constraint

We identified the following interesting effects of the direct detection constraint on the model:

- In light of the stringent bounds, provided by leading direct detection experiments, a destructive interference between the different contributions to WIMP-nucleon scattering is needed for large couplings. In case of top-flavoured DM, this puts strong constraints on the mixing angle θ_{13} . We observe both an upper as well as for some range of $D_{\lambda,33}$ also a lower bound on θ_{13} .

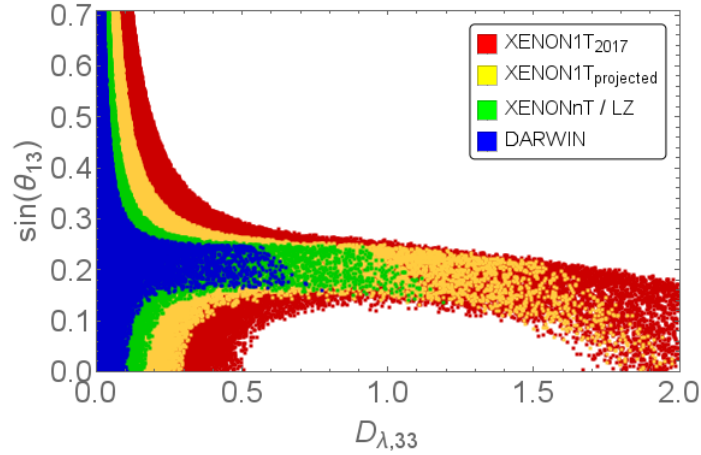


Figure 7.3: Valid areas of parameter space, for different applied strength of cross section limits, for DM mass $m_\chi = 250$ GeV and mediator mass $m_\phi = 850$ GeV. The current exclusion bounds of XENON1T [78] as well as the projected bounds of XENON1T [79], XENONnT [79], LUX-ZEPLIN (LZ) [80] and DARWIN [81] have been applied respectively.

- The necessary cancellation can not be achieved for arbitrarily large couplings. This results in an upper bound on the couplings, see Appendix A for more details.
- It is essential to consider the different xenon isotopes present in natural xenon. Since the aforementioned cancellation pattern is different for different isotopes, a sufficient simultaneous suppression for all isotopes is necessary. For larger coupling $D_{\lambda,33}$, this is harder to achieve. In light of stronger direct detection bounds from upcoming experiments, the upper bound on the couplings will get more stringent.
- Since the only negative contribution, enabling the discussed cancellation, is the Z-penguin coupling to the neutron, which has only sufficient size for top-quarks in the loop, the direct detection bounds favour a top-flavoured DM candidate. The top-flavour has a naturally large coupling to the top-quark, favouring the necessary cancellation and allowing for a sufficient suppression of the tree-level contribution.

Combined Analysis of Constraints

Finally, having studied the effects of all constraints on their own, we take a look at their combined impact. First, we present a combined analysis of flavour, relic abundance and direct detection constraints, implemented in our MATHEMATICA program. We identify the superposition and interference of the individual constraints. The consequences of future data is also discussed, especially in view of the consequences for the DM mass bounds. Finally, we summarize the overall interplay of the entire multitude of effects, including those from collider bounds obtained using MadGraph5_aMC@NLO.

8.1 Phenomenological Analysis

8.1.1 Methodology

We use our self-written MATHEMATICA program to find the valid parameter space satisfying flavour, relic abundance and direct detection constraints at the same time. To identify the valid parameter space, first all parameters of the NP coupling matrix λ are randomized. At this stage we apply constraints on the couplings $D_{\lambda,ii}$ to guarantee top-flavoured dark matter relic in the chosen freeze-out scenario. We conduct scans for both quasi-degenerate freeze-out (QDF) as well as single flavour freeze-out (SFF) with the respective constraints and values of η applied as presented in Chapter 6. Such scans are conducted for several pairs of DM masses m_χ and mediator masses m_ϕ to get a broad overview of all effects at different mass values.

After having randomized the parameters of λ in accordance with the freeze-out scenario, we calculate the corrected masses of the DM flavours $m_{\chi_u}, m_{\chi_c}, m_{\chi_t}$. The complete set of parameters $\{D_{\lambda,11}, D_{\lambda,22}, D_{\lambda,33}, \theta_{12}, \theta_{13}, \theta_{23}, \delta_{12}, \delta_{13}, \delta_{23}, m_\phi, m_{\chi_u}, m_{\chi_c}, m_{\chi_t}\}$ is then tested against the constraints.

To save computation time the constraints are applied in order of significance. The relic abundance constraint is applied first, since it has proven to veto the largest part of the parameter space. We neglect the minor effects of mass-splitting in the QDF case. Only if the parameter set satisfies the relic abundance constraint, the WIMP-nucleon cross section is calculated and tested against the direct detection bound for DM mass m_{χ_t} . If this bound is satisfied as well, we finally check the flavour constraints. As described in Chapter 5, we neglect the mass corrections in the loop function, since they only cause a negligible quantitative correction. In case the parameter set passes all constraints, we keep it. Scanning over a huge amount— $\mathcal{O}(10^8 - 10^{10})$ —of randomized parameter sets gives us then a chart of the valid parameter space.

Apart from the scans at fixed mediator and DM mass, we also conduct scans where the DM and mediator mass parameters are randomized together with the other parameters. This helps us to better understand the mass bounds in the combined analysis, see Subsection 8.1.3.

8.1.2 Superposition and Interference of Effects in Combined Analysis

The combined analysis conducted here includes flavour, relic abundance and direct detection constraints. The collider constraints are only “applied” in form of the safe parameter space identified in Chapter 4.

Figure 8.1 shows valid mixing angles for fixed mediator mass $m_\phi = 850 \text{ GeV}$ in different scenarios with different DM masses m_χ . In each plot we show in different colours all mixing angles θ_{ij} displayed in dependence of the splitting between the related couplings $|D_{\lambda,ii} - D_{\lambda,jj}| = \Delta_{ij}$.

In all diagrams we recover the effect from the $D^0 - \bar{D}^0$ mixing constraint. The mixing angle θ_{12} is only allowed to take large values if the splitting between $D_{\lambda,11}$ and $D_{\lambda,22}$ is sufficiently small.

An even stronger effect is visible for θ_{13} . In all presented cases the mixing angle is only allowed to take values in a narrow band. Figure 8.2 helps us to understand this effect better. In this figure we can see the valid θ_{13} values in dependence of $D_{\lambda,33}$ for different DM masses at a fixed mediator mass in the QDF scenario and with the combined constraints applied. We can see that for different DM mass values, different valid areas are found. Those valid areas are always confined to a limited range in both $D_{\lambda,33}$ and θ_{13} . The reason is the interference between relic abundance and direct detection constraints. For fixed DM mass and mediator mass the RA constraint will force the coupling into a valid interval. For all dark matter masses shown in Figure 8.2 the required interval is beyond the values of $D_{\lambda,33}$ where all mixing angles θ_{13} are still allowed by the direct detection bound. Instead we are in the $D_{\lambda,33}$ range where we find a band of θ_{13} . Depending on the DM mass, the relic abundance constraint cuts out a piece from this valid band. By combining the valid areas in Figure 8.2 it is possible to trace the original valid- θ_{13} band—from the direct detection constraints alone. With decreasing DM mass the relic abundance constraint demands larger $D_{\lambda,33}$ until for $m_\chi = 100 \text{ GeV}$ the part is reached where the band allows θ_{13} as low as 0. We can conclude that the combination of direct detection and relic abundance bounds results

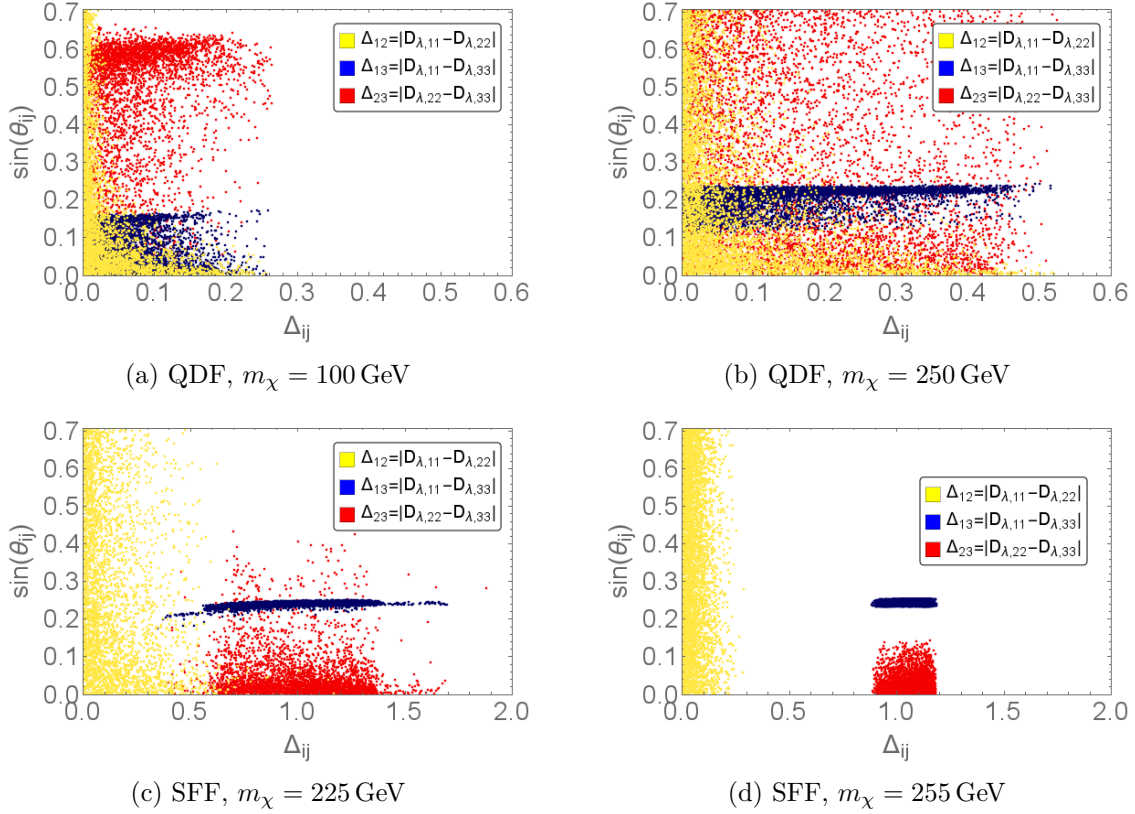


Figure 8.1: Valid regions of parameter space, with combined flavour, relic abundance and direct detection constraints applied, for different freeze-out scenarios and DM masses, with $m_\phi = 850$ GeV. Different colours correspond to the different mixing angles θ_{ij} and associated splittings $|D_{\lambda,ii} - D_{\lambda,jj}| = \Delta_{ij}$: $ij = 12$ in yellow, $ij = 13$ in blue, $ij = 23$ in red.

in a serious constraint on the parameter space of our model, especially on θ_{13} .

The same effect takes place in case of SFF. But, as we can see in Figure 8.1c and Figure 8.1d, the impact is even more serious, forcing θ_{13} into a very narrow valid band. The reason for this is the strong impact of the relic abundance constraint on θ_{13} and θ_{23} . As discussed in Subsection 6.3.2 in detail, those two mixing angles in addition to $D_{\lambda,33}$ are the only parameters governing the annihilation cross section in single flavour freeze-out. Since they need to satisfy both direct detection and relic abundance constraints in the combined analysis (as well as the weaker but still existing flavour constraints), they are constrained to a smaller valid region which allows to satisfy all bounds simultaneously. Already in Figure 8.1c for $m_\chi = 225$ GeV we can see that the highest values of θ_{23} are excluded, in Figure 8.1d we can see that for slightly bigger DM mass the constraints have even more drastic effects.

Note that the same narrow valid band can also be observed in the QDF case. Although the overall valid band is broader, we can identify a narrow sub-band which is more densely populated in the scatter plot. The explanation for this sub-band is that this narrow band is close to the perfect cancellation for the average WIMP-xenon scattering cross section. If the cancellation is close to perfect already via the value of θ_{13} , the other parameters have

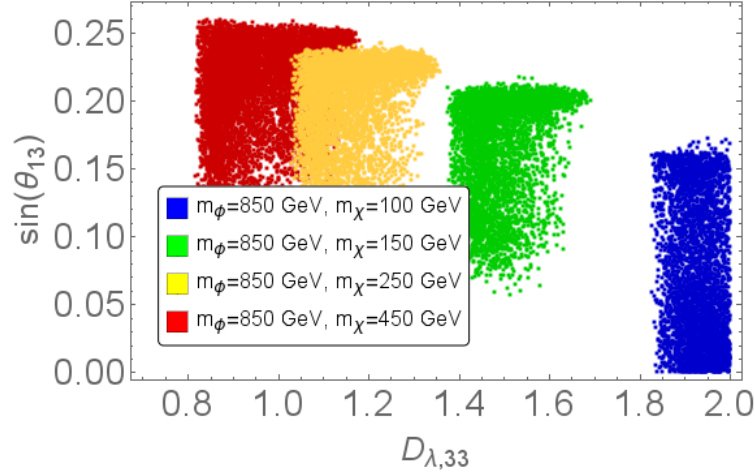


Figure 8.2: Valid ranges of flavour mixing angle θ_{13} as function of $D_{\lambda,33}$ for various values of m_χ and fixed m_ϕ (in QDF) with combined flavour, relic abundance and direct detection constraints applied.

more flexibility, making it more likely to find valid parameter sets. While for QDF, also θ_{13} values outside the near-perfect cancellation area have a chance of fulfilling the combined constraints, in the SFF case only the near-perfect cancellation area survives, since the other parameters are already strictly constrained.

In addition to the effect on the mixing angles, we can observe the effect from the SFF conditions on the couplings $D_{\lambda,ii}$. For larger DM masses, the relic abundance constraint demands small couplings. But to ensure SFF the couplings need to be split by a minimum amount, depending on η defined in (6.5). For our choice of η this leads to a minimum value for the third generation coupling of roughly $D_{\lambda,33} = 1.16$. We can see in Figure 8.1d that, already for a DM mass of $m_\chi = 250$ GeV, $D_{\lambda,33}$ is forced close to this value. Since for such small $D_{\lambda,33}$ the other couplings need to be close to zero, we observe large splittings Δ_{13} and Δ_{23} . It is easy to extrapolate this behaviour to larger DM masses, resulting in the aforementioned exclusion of SFF for too large DM masses.

We also observe the effect of the splitting conditions in the QDF case. Comparing Figure 8.1a to Figure 8.1b, we can see that the allowed splittings are more seriously restricted for the smaller DM mass. The reason is that the smaller DM masses demand larger couplings $D_{\lambda,ii}$. Since the magnitude of the mass corrections is larger for increased couplings, larger relative mass-splittings are realized for the same inter-coupling splitting at larger absolute value of the couplings. To still satisfy a mass-splitting below 1%, which is demanded to realize the QDF scenario, the couplings are hence forced to lie closer together for larger values.

8.1.3 Dark Matter Mass Bounds in Combined Analysis

To conclude our analysis we study the valid DM mass ranges in light of the combined constraints. Scanning over the entire parameter space, including m_χ and m_ϕ , results in the

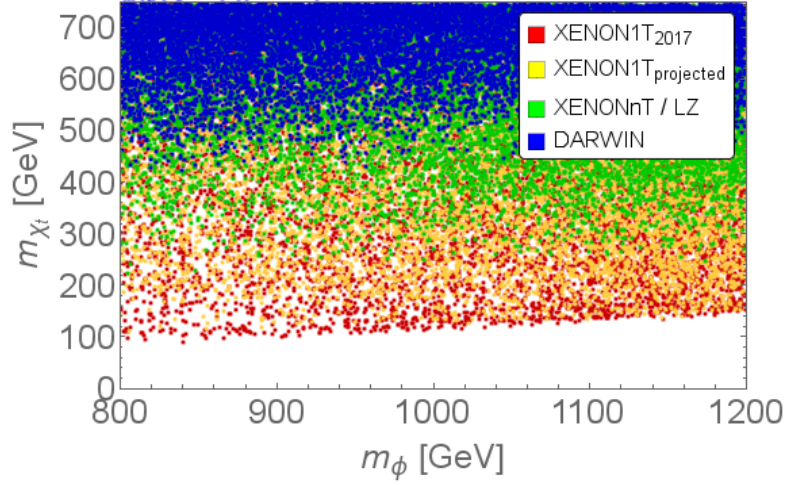
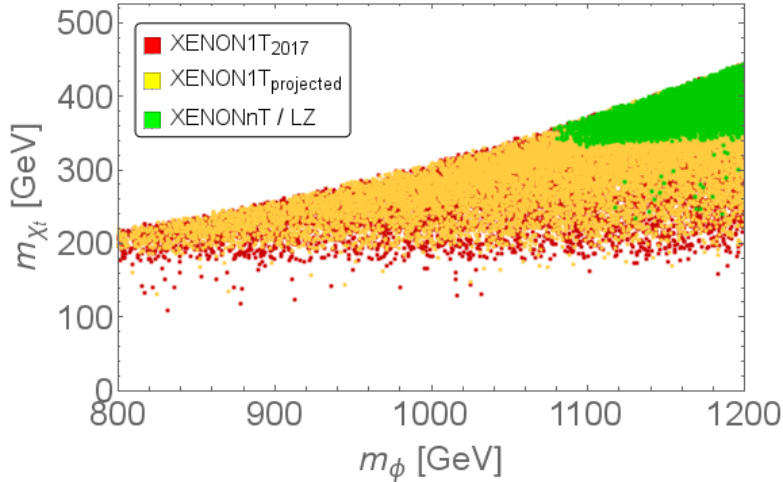
(a) QDF scenario (with $\eta = -0.01$).(b) SFF scenario (with $\eta = -0.075$).

Figure 8.3: Valid area in the $m_\phi - m_{\chi_t}$ plane with combined flavour, relic abundance and direct detection constraints applied. We show the valid area for different strengths of direct detection bounds. The current exclusion bounds of XENON1T [78] as well as the projected bounds of XENON1T [79], XENONnT [79], LUX-ZEPLIN (LZ) [80] and DARWIN [81] are applied respectively. The interference of relic abundance and direct detection effects results in a lower bound on the DM mass, increasing with more stringent direct detection bounds.

plots in Figure 8.3. We see the valid parameter space in the $m_\phi - m_{\chi_t}$ range for different strengths of the direct detection bounds. We can observe a lower bound on the dark matter mass (depending weakly on m_ϕ). As discussed in Chapter 6, such a lower bound naturally results from the relic abundance constraint in combination with an upper limit on the couplings, such as the $2.0 \geq D_{\lambda,33} \geq D_{\lambda,11}, D_{\lambda,22}$ limit we picked as a consequence of strong LHC constraints.

In Subsection 7.3.3 we found that more stringent direct detection bounds lead to an even more serious upper bound on the couplings, mainly due to the necessary simultaneous suppression of DM scattering cross sections with all xenon isotopes. For low masses the relic abundance constraint demands too large couplings which are no longer allowed for such strong direct detection bounds. Hence, we conclude that the combined constraints result in a lower bound on the DM mass in our model. We can see that the lower bound on the DM mass slightly increases with increasing m_ϕ . Therefore, this bound can not be relaxed by picking a larger mediator mass. Lower mediator masses allow for lower DM masses in this combined analysis, but will ultimately be rejected by LHC bounds. In summary, more stringent direct detection bounds result in an indisputable exclusion of larger and larger DM masses, constituting a larger and larger discovery potential.

For completeness, we should mention that in the discussion so far we assumed that the DM flavour χ_t of our model constitutes the entire relic abundance of dark matter. Instead we could assume that our DM candidate only provides a fraction of the DM relic. This would relax the constraints from the absence of signal in the direct detection experiments. But, at the same time we would require a larger annihilation cross section to achieve a smaller χ_t relic abundance. Hence, at fixed m_ϕ and m_χ such a relaxation of the relic assumption would demand larger couplings, which then in turn result in a higher WIMP-nucleon scattering cross section. The exact relation between these two effects—relaxation of the direct detection bounds and simultaneous necessary increase of the scattering cross section—has not been analyzed in this study and is in detail left for future work. A rough estimate shows that these two effects approximately cancel each other.

For the SFF case we see even more drastic consequences of the combined constraints. DM masses below the top-quark mass require a large degree of fine-tuning, even for the current constraints. Future direct detection bounds push the DM mass bound significantly higher. For the chosen $\eta = -0.075$ the DARWIN constraints will be enough to completely exclude SFF for $m_\phi < 1.2$ TeV. This can of course be relaxed by allowing a larger (in magnitude) η . Nevertheless, the important insight is that sufficiently strong direct detection bounds can probe the entire SFF scenario.

Before we start the summary of constraints, a remark on the LHC bounds from run 2 data is in order. We concluded in Chapter 4 that the constraints from run 1 data does not affect the parameter space bounded by $m_\phi > 850$ GeV, $2.0 \geq D_{\lambda,33} \geq D_{\lambda,11}, D_{\lambda,22}$. Since the run 2 data will result in more serious constraints, we expect a larger fraction of the parameter space to be affected. Most likely a significant part in the low DM mass / low mediator mass region in the plots in Figure 8.3 will be excluded by the updated LHC constraints. Nevertheless, the most important result of the combined analysis is the possibility to probe a large range of DM masses independent of the mediator mass using the combination of relic abundance and direct detection constraints. Opposed to this, the absence of LHC signals can easily be justified by a large mediator mass.

8.2 Summary of Constraints

We want to conclude this analysis with a summary of the whole multitude of constraints and their interplay. The following crucial effects on the up-type DMFV model have been identified:

- The strongest collider constraints come from jets + \cancel{E}_T final state searches. They exclude low mediator masses. For large couplings the NP production channel is dominant. Hence, the collider constraints require sufficiently low couplings for reasonably low mediator masses.
- Constraints from $D^0 - \bar{D}^0$ mixing require a suppressed mixing angle θ_{12} or a sufficient degeneracy of $D_{\lambda,11}$ and $D_{\lambda,22}$.
- Requiring the observed abundance of dark matter to be a thermal relic, forces the couplings into certain ranges (depending on the mediator and DM mass). The upper bound on the couplings then result in a lower bound on the DM mass (depending on the mediator mass).
- The large top-quark mass results in different freeze-out patterns depending on the DM mass. If the top-quark final state channel is significantly suppressed or excluded, mixing angles can significantly affect the annihilation cross section.
- In the SFF scenario, the mixing angles θ_{13} and θ_{23} considerably affect the annihilation cross section. Due to the reduced number of contributing terms the effect on the remaining parameters is more stringent.
- The necessary splitting condition on the coupling $D_{\lambda,33}$ for SFF together with relic abundance constraints results in an upper bound on the dark matter mass (depending on η).
- Direct detection bounds provide serious constraints. If the WIMP-nucleon cross section is not sufficiently suppressed by small couplings or a large mediator mass, a destructive interference of the different contributions is necessary. For this interference to happen, the mixing angle θ_{13} is restricted to a narrow band.
- Since direct detection experiments use natural xenon, the cancellation has to be sufficient for all stable xenon isotopes. Since this is hard to achieve, the larger values of $D_{\lambda,33}$ are excluded. More stringent future bounds will push down the upper limit for $D_{\lambda,33}$.
- The necessary cancellation pattern in the the WIMP-nucleon cross section originates in the negative neutron Z-penguin contribution. This contribution is only significant for a top-quark in the loop. Hence, the cancellation pattern is favoured in the top-flavoured relic DM case, which we chose as the benchmark model for this study.

By imposing the constraints simultaneously, we find an interesting interplay:

- For a given DM and mediator mass, the relic abundance constraint demands the couplings to lie in a certain range. If the couplings achieved in this way are sizeable, the direct detection bounds will then force the flavour mixing angle θ_{13} in a narrow valid band.
- For dark matter masses $m_{\chi_t} < m_t$ the SFF scenario is only possible at the price of fine-tuning, mostly due to the significant demand of the relic abundance constraint on the mixing angles. Since only $D_{\lambda,33}$, θ_{13} and θ_{23} are governing the annihilation cross section, and only few terms remain, the constraints on those mixing angles are very stringent. They need to fulfill those stringent bounds and hence are less flexible to also satisfy the other constraints.
- Although the case of two flavour freeze-out was not discussed in this study, it is straightforward to infer one effect of such a scenario. Demanding top-flavoured dark matter would lead to a necessary splitting between $D_{\lambda,11}$ and $D_{\lambda,22}$. In combination with the $D^0 - \bar{D}^0$ mixing constraints this would then cause an upper bound on θ_{12} .
- The constantly improving bounds from direct detection experiments push down the upper limit on the couplings. Combined with the relic abundance constraint this leads to an increasing lower bound on the DM mass. The exact bound value depends on the mediator mass. A larger mediator mass m_ϕ results in an increased lower bound on m_χ . Hence, opposed to collider bounds, this combination of relic abundance and direct detection constraints effectively probes an increasing range of DM masses (for all mediator masses), hopefully bringing us closer to a discovery.

Finally we want to remark on the identified valid parameter space. As discussed in Chapter 2, the good agreement of SM predictions and flavour experiments is a major motivation for testing new models first in the framework of Minimal Flavour Violation (MFV). Another reason for this is the simplicity of this framework, resulting in a small number of new parameters. In this study we went beyond MFV, following the principles of Dark Minimal Flavour Violation (DMFV). In Section 3.5 we discussed the MFV limit of our model. Yet, the phenomenological analysis of all constraints identified valid parameter space, which in large parts is nowhere near the MFV limit. Our results underline that the experimental data does not demand such a restriction of NP models in general. Going beyond MFV rewards us by a rich and interesting new phenomenology and is hence well motivated.

Coupling Flavoured Dark Matter to the Left-Handed Quark-Doublet

So far we have studied a model coupling a DM flavour triplet to the right-handed SM up-quark flavour triplet. This has been done analogously to the down-quark DMFV model, which had been studied in [25]. Now we want to study a more complex model, coupling the DM flavour triplet to the SM left-handed quarks, which is a doublet under the electroweak $SU(2)_{EW}$ gauge symmetry, see Chapter 2. We study the most straightforward realization of such an interaction, introducing a $SU(2)_{EW}$ -doublet mediator, which allows us to keep the DM flavour triplet as a $SU(2)_{EW}$ -singlet. We again follow the principles of Dark Minimal Flavour Violation (DMFV), studying a general coupling structure. In this chapter we follow the same structure as in the analysis of the up-quark DMFV model. To avoid unnecessary repetition, we limit the discussion to the basic principles and most fundamental results. Our main focus lies on understanding the differences between the up-quark DMFV and quark-doublet DMFV model and the changed impact on the phenomenology.

9.1 Simplified Model

The fundamental interaction in the model coupling the DM flavour triplet to the left-handed SM $SU(2)_{EW}$ quark-doublet is given as

$$\mathcal{L}_{\text{int}} = - \left(\lambda'_{ij} \bar{q}'_{Li} \chi_j \Phi + h.c. \right). \quad (9.1)$$

Here, $\bar{q}'_{Li} = (\bar{u}'_{Li}, \bar{d}'_{Li})$ labels the left-handed SM $SU(2)_{EW}$ quark-doublet in the flavour basis. λ'_{ij} labels the NP coupling between the new particles and the quark-doublet in the flavour basis. With $\chi_j = (\chi_u, \chi_c, \chi_t)^\top$ we denote the DM flavour triplet of Dirac fermions. Just as in the up-quark DMFV model, we chose its members to be SM gauge singlets.

For convenience we label the components the same way as in the up-quark DMFV model. Finally we introduced the $SU(2)_{EW}$ mediator-doublet scalar $\Phi = (\phi_u, \phi_d)^\top$, which has to carry the QCD colour and hypercharge of the SM quark-doublet. This way, the interaction is gauge invariant. This interaction guarantees a stable DM candidate in analogy to the up-quark DMFV model, see Section 3.3.

We chose to present the NP interaction in the quark-doublet flavour basis to be able to derive its correct form in the mass basis. As discussed in Chapter 2, to diagonalize the mass matrices of the SM quarks, \bar{u}'_{Li} and \bar{d}'_{Li} have to be multiplied by different unitary matrices V_{uL} and V_{dL} . The general parametrization of λ in the DMFV framework was derived in Section 3.2. Recalling the singular value decomposition $\lambda = U_\lambda D_\lambda V_\lambda$, we can see that an unitary 3×3 matrix can be absorbed into U_λ in the definition of λ . Hence, for the up-quark DMFV model this was no issue, which is why we did not even discuss this. But in the doublet-quark DMFV model we get different unitary matrices V_{uL} and V_{dL} in the up and down sector. Hence, we need to make a choice. This is a direct consequence of coupling our NP particles to the SM quark-doublet.

For the course of this study we choose to absorb V_{uL} . We define $\lambda := V_{uL} \lambda'$ as our basis DM-quark coupling in the mass-basis of the quarks. In the down-sector we then find the coupling to be $\tilde{\lambda} := V_{dL} V_{uL}^\dagger \lambda = V_{CKM}^\dagger \lambda$. Here we have used the standard definition for the CKM-matrix V_{CKM} , see Chapter 2. Decomposing the interaction term in up-quark and down-quark coupling parts, we then find:

$$\mathcal{L}_{\text{int}} = -(\lambda_{ij} \bar{u}_{Li} \chi_j \phi_u + h.c.) - (\tilde{\lambda}_{ij} \bar{d}_{Li} \chi_j \phi_d + h.c.), \quad (9.2)$$

with \bar{u}_{Li} and \bar{d}_{Li} denoting the quarks in the mass-basis. Following the principles of DMFV we use the parametrization introduced in Section 3.2 for the coupling λ being a new source of flavour and CP violation beyond Minimal Flavour Violation (MFV). For V_{CKM} we use the latest new physics results of the UTfit Collaboration [86]. The new physics fit provides the best estimate of the CKM-matrix under the assumption of a new physics influence being present in the measurement of FCNC processes. Since our model directly predicts such new physics, we need to use the new physics fit.

We can see from the interaction-part of the Lagrangian (9.2) that this quark-doublet DMFV model in some way is a combination of the previously studies up-quark DMFV [35] and down-quark DMFV model [25]. Yet it is not a simple superposition, since the couplings in the up- and down-sectors are connected. Hence, in the phenomenological implications on λ we can expect an interesting combination of the constraints found for those two models.

The mass terms are again realized in the most simple way, following the principles of DMFV

$$\mathcal{L}_{\text{mass}} = -m_{\chi,ij} \bar{\chi}_i \chi_j - m_\phi^2 \Phi^\dagger \Phi. \quad (9.3)$$

Note that ϕ_u and ϕ_d have the same mass m_ϕ on Lagrangian level. Due to their different couplings to the Higgs sector (we do not explicitly state those couplings here), this degeneracy will be violated when the Higgs acquires a vacuum expectation value (VEV). We neglect

such mediator mass corrections in this analysis.

Due to the unitarity of the CKM-matrix, it will drop out of the mass-splitting formula, which hence takes the same form as in the up-quark DMFV model:

$$m_{\chi,ij} = m_{\chi} \left(\mathbb{1} + \eta_1 \lambda^\dagger \lambda + \eta_2 \tilde{\lambda}^\dagger \tilde{\lambda} + \mathcal{O}(\lambda^4) \right)_{ij} = m_{\chi} \left(1 + \eta (D_{\lambda,ii})^2 + \mathcal{O}(\lambda^4) \right) \delta_{ij}. \quad (9.4)$$

We again incorporate $\eta = \eta_1 + \eta_2$ as a free parameter in our simplified model.

Using (9.1) and (9.4) we can try to identify a MFV limit for this model, in the way discussed in Section 3.5. As can be checked easily, the only valid limit is achieved by identifying the DM flavour with the quark-doublet flavour symmetry $U(3)_\chi \cong U(3)_q$.

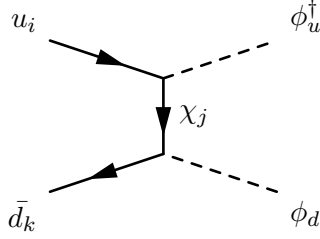
9.2 LHC Constraints

As discussed in Section 4.2 the strongest bounds originate from mediator pair production and subsequent decay. This holds true for the quark-doublet DMFV model as well. ϕ_u couples to DM and the up-quark triplet, while ϕ_d couples to DM and the down-quark triplet. We get the following changes compared to the up-quark DMFV model's phenomenology.

- **Production:** The QCD production mode via the gluons remain the ones shown Figure 4.3a to Figure 4.3d. Those production modes can generate $\phi_u \phi_u^\dagger$ and $\phi_d \phi_d^\dagger$. Only the t-channel DM exchange in addition can generate a mixed state of ϕ_u and ϕ_d , see Figure 9.1.
- **Decay:** ϕ_u will strictly decay into DM plus a member of the up-quark triplet, while ϕ_d strictly decays to DM plus a member of the down-quark triplet. Hence, we need to consider the following possible final states, for which dedicated searches exist. $t\bar{t} + \cancel{E}_T$ can be realized if we have a $\phi_u \phi_u^\dagger$ intermediate state, with both mediators decaying into the third generation quarks. The effect of the parameters on the cross section for this final state is exactly the same as in the up-quark DMFV model. In addition $b\bar{b} + \cancel{E}_T$ can be realized with $\phi_d \phi_d^\dagger$ intermediate state and subsequent decay to third generation quarks. The effects are basically (negligible corrections due to the influence of the CKM-matrix) the same as in the down-quark DMFV model. The final signature is then jets + \cancel{E}_T . This final state can not only be realized for $\phi_d \phi_d^\dagger$ and $\phi_u \phi_u^\dagger$ intermediate state but also for the mixed states of ϕ_u and ϕ_d - each time with decay to light quarks of both mediators respectively.

Since there are a lot more contributions to the jets + \cancel{E}_T in this model but approximately the same contributions for the $b\bar{b} + \cancel{E}_T$ and $t\bar{t} + \cancel{E}_T$ final states, it comes as no surprise that we observe by far the strongest constraints from the jets + \cancel{E}_T bounds - which have already been found to be dominant in the up-quark DMFV and down-quark DMFV model respectively.

For the phenomenological analysis we use the assumptions, simplifications and strategies which were discussed in Chapter 4. To keep it short we only show the exclusion bounds

Figure 9.1: Relevant production channel for $\phi_u\phi_d$ mixed state.

from the jets + \cancel{E}_T final state, see Figure 9.2. We can see that the constraints for equivalent coupling strengths exclude a significantly larger region of the $m_\phi - m_{\chi_t}$ plane than in the up-quark DMFV model. We do not show the exclusion bounds for mediator masses larger than 1 TeV, since in this area numerical uncertainties from extrapolation of the exclusion data given in [48] dominate.

From Figure 9.2a we can learn that we would have to constrain $1.5 \geq D_{\lambda,33} \geq D_{\lambda,11}, D_{\lambda,22}$ to be safe from the constraint for mediator masses as low as 850 GeV. Nevertheless, for the course of this analysis we will use the same “safe parameter space”, which was identified for the up-quark DMFV model analysis, see Section 4.5. This allows for a direct comparison of the respective results of the two models. In doing so, we have to keep in mind that for these parameter bounds $2.0 \geq D_{\lambda,33} \geq D_{\lambda,11}, D_{\lambda,22}$ the jets + \cancel{E}_T bounds exclude the lower DM masses for the largest couplings, see Figure 9.2b.

9.3 Flavour Constraints

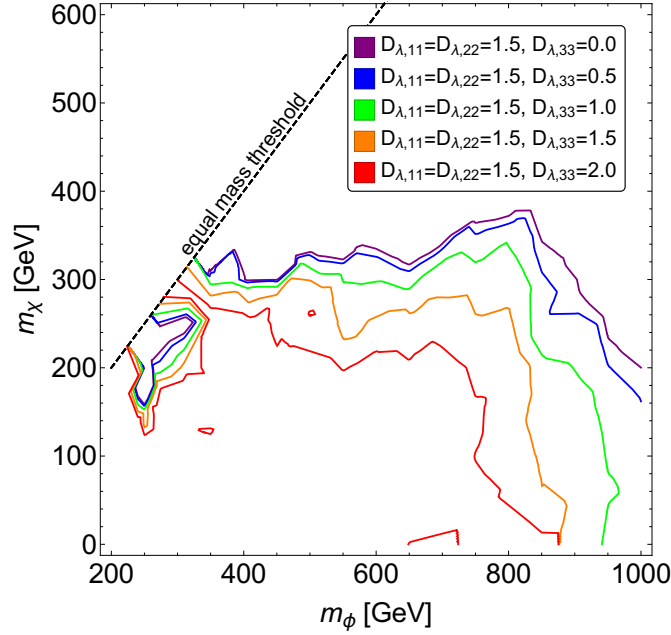
Since the NP particles in this model couple to all quark flavours, we have to consider not only constraints from $D^0 - \bar{D}^0$ mixing but also from $K^0 - \bar{K}^0$ mixing and $B_{d,s}^0 - \bar{B}_{d,s}^0$ mixing. The off-diagonal mass matrix elements can be calculated in the same way as was sketched for the $D^0 - \bar{D}^0$ mixing. We find

$$M_{12}^{K,\text{new}} = \frac{1}{384\pi^2 m_\phi^2} \eta_2 m_K f_K^2 \hat{B}_K \left((\tilde{\lambda}\tilde{\lambda}^\dagger)_{sd} \right)^2 \cdot L(x_i, x_j). \quad (9.5)$$

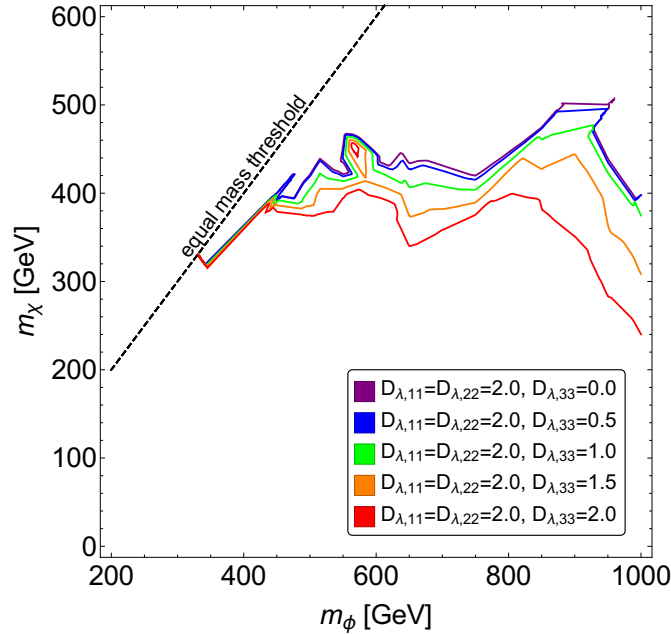
and

$$M_{12}^{B_q,\text{new}} = \frac{1}{384\pi^2 m_\phi^2} \eta_B m_{B_q} f_{B_q}^2 \hat{B}_{B_q} \left((\tilde{\lambda}\tilde{\lambda}^\dagger)_{bq} \right)^2 \cdot L(x_i, x_j) \quad (q = d, s). \quad (9.6)$$

The loop function $L(x_i, x_j)$ has been defined in (5.4). $M_{12}^{D,\text{new}}$ has been given in (5.7). Note that (9.5) and (9.6) include the coupling $\tilde{\lambda}$ and hence include V_{CKM} . As discussed in Chapter 5, the unitary matrices will only drop out in case of D_λ being proportional to the unity matrix, i.e. in the case of degenerate couplings. In any other case the CKM-matrix will affect the predicted contribution. This will change the effects of the flavour constraints on λ compared to the phenomenological analysis performed in [25].



(a) 95% C.L. exclusion contours of the quark-doublet DMFV model for various strength of third generation couplings, with fixed $D_{\lambda,11} = D_{\lambda,22} = 1.5$.



(b) 95% C.L. exclusion contours of the quark-doublet DMFV model for various strength of third generation couplings, with fixed $D_{\lambda,11} = D_{\lambda,22} = 2.0$.

Figure 9.2: Constraints on the jets + \cancel{E}_T final state from 8 TeV LHC run 1 data, obtained from bounds in [48].

$C_{\Delta M_K}$	1.10 ± 0.44
C_{ϵ_K}	$\in [0.83, 1.28]$
C_{B_d}	$\in [0.81, 1.28]$
ϕ_{B_d}	$\in [-5.2^\circ, 1.5^\circ]$
C_{B_s}	$\in [0.899, 1.252]$
ϕ_{B_s}	$\in [-1.848^\circ, 1.959^\circ]$

Table 9.1: Constraints on the $K^0 - \bar{K}^0$ and $B_{d,s}^0 - \bar{B}_{d,s}^0$ systems [56, 87, 88].

Defining

$$M_{12}^{B_q} = C_{B_q} e^{2i\phi_{B_q}} M_{12}^{B_q, \text{SM}} \quad (q = d, s), \quad (9.7)$$

as well as

$$\Re(M_{12}^K) = C_{\Delta M_K} \Re(M_{12}^{K, \text{SM}}), \quad (9.8)$$

$$\Im(M_{12}^K) = C_{\epsilon_K} \Im(M_{12}^{K, \text{SM}}). \quad (9.9)$$

we constrain our predictions for $C_{\Delta M_K}$, C_{ϵ_K} , C_{B_d} , ϕ_{B_d} , C_{B_s} and ϕ_{B_s} following the procedure in [25]. We impose the newest results [56] at the 2σ level. In lack of more recent constraints on $C_{\Delta M_K}$ we apply the same bounds [87, 88] used in [25]. The CKM input data is set to their central values given in [86], the remaining input parameters are set to their central values given in Table 3 of [89]. The applied constraints on the $K^0 - \bar{K}^0$ and $B_{d,s}^0 - \bar{B}_{d,s}^0$ systems are listed in Table 9.1. Of course we still need to constrain our prediction for the $D^0 - \bar{D}^0$ system. This is done in the same way as described in Chapter 5.

In Figure 9.3 we see the valid areas for the mixing angles θ_{ij} depending on the respective splitting $|D_{\lambda,ii} - D_{\lambda,jj}| = \Delta_{ij}$, having applied the combined constraints of $D^0 - \bar{D}^0$ mixing, $K^0 - \bar{K}^0$ mixing and $B_{d,s}^0 - \bar{B}_{d,s}^0$ mixing. No freeze-out conditions have been imposed on the couplings $D_{\lambda,ii}$. Furthermore, we neglected the mass-splitting of DM flavours in the numerical analysis, as discussed before.

We can see the impact of the significantly more stringent constraints from $K^0 - \bar{K}^0$ mixing and $B_{d,s}^0 - \bar{B}_{d,s}^0$ mixing data on the flavour mixing angles. Compared to the up-quark DMFV model we find significant effects on θ_{13} and θ_{23} as well. The effects on θ_{12} remain the most severe. The combination of constraints rejects any splitting Δ_{12} larger than approximately 0.5. The model is unable to satisfy both the $D^0 - \bar{D}^0$ and $K^0 - \bar{K}^0$ bounds for too large splitting Δ_{12} . This is due to the influence of the CKM-matrix. The large $|V_{us}| \approx 0.2$ can not be eliminated in both contributions, no matter which λ is chosen.

Comparing the valid areas in Figure 9.3 with the valid areas obtained in Figure 5 of [25], it appears as if our upper bounds on the flavour mixing angles are less severe - apart from the cut for a too large Δ_{12} . This comes as a surprise, since our model implements not just the same bounds as the down-quark DMFV model, but the limits from $D^0 - \bar{D}^0$ as well. The

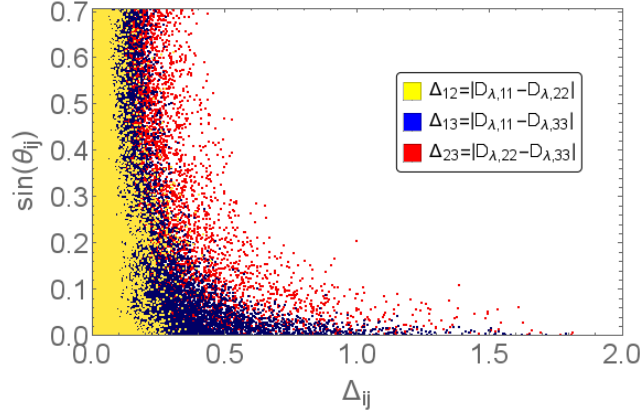


Figure 9.3: Valid ranges of flavour mixing angles θ_{ij} of the quark-doublet DMFV model in dependence of the splittings between couplings $D_{\lambda,ii}$ and $D_{\lambda,jj}$, for mediator mass $m_\phi = 850$ GeV and DM mass $m_\chi = 250$ GeV. The different colours correspond to the different mixing angles θ_{ij} and splittings $|D_{\lambda,ii} - D_{\lambda,jj}| = \Delta_{ij}$: $ij = 12$ in yellow, $ij = 13$ in blue, $ij = 23$ in red.

main reason for this difference is the different approaches in scanning the couplings $D_{\lambda,ii}$. In this study we scan all coupling independently, allowing each of them to take a random value in the interval $[0, 2]$. Opposed to this, the authors of [25] scan two parameters $\delta\lambda_1, \delta\lambda_2 \in [-1, 1]$ and subsequently identify $D_{\lambda,11} = 1 + \delta\lambda_1$, $D_{\lambda,22} = 1 + \delta\lambda_2$, $D_{\lambda,33} = 1 - \delta\lambda_1 - \delta\lambda_2$. They only keep the parameter set if $D_{\lambda,33} > 0$. Opposed to our scan procedure, this does not cover the whole parameter space, e.g. the case $D_{\lambda,11} = D_{\lambda,22} = D_{\lambda,33} = 0.5$ can not be realized in their scanning procedure, as can be easily checked. Since we cover the entire parameter space in this study, we find more valid areas than in [25]. This explanation has been tested by scanning the parameter space in the same way as in [25], which reproduces the results of the latter paper.

9.4 Relic Abundance Constraint

Compared to the up-quark DMFV model, the DM flavours can now also decay to members of the down-quark triplet. This increases the number of possible final states. The annihilation cross section is given as:

$$\langle\sigma v\rangle_{\text{eff}} = \langle\sigma v\rangle_{\text{eff}}^u + \langle\sigma v\rangle_{\text{eff}}^d \quad (9.10)$$

The contributions from up-quark and down-quark final states strictly decouple, no mixed final states are possible. The contribution for the up-quark final states is given in (6.7) in

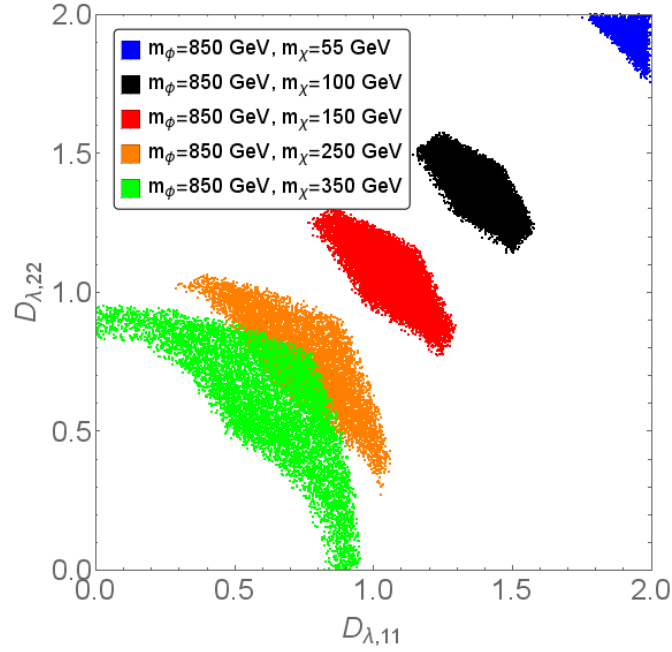


Figure 9.4: Valid regions of parameter space of the quark-doublet DMFV model in the QDF scenario (with $\eta = -0.01$) compatible with the relic abundance constraint, at different DM masses.

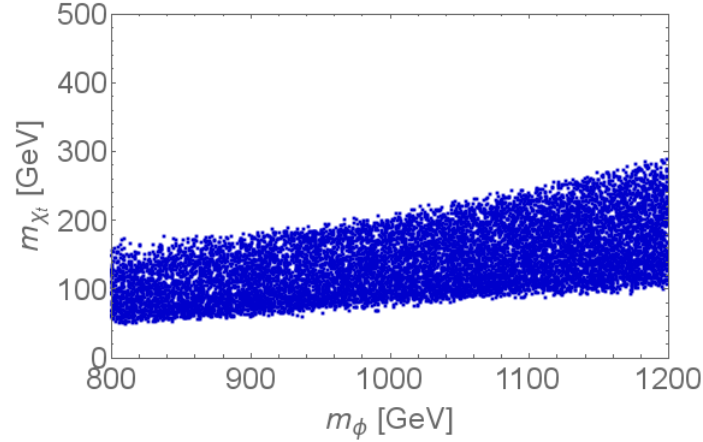


Figure 9.5: Valid DM mass ranges of the quark-doublet DMFV model in dependence on m_ϕ for SFF (at fixed $\eta = -0.075$) with relic abundance constraint applied. We observe both a lower and upper bound on the DM mass.

its most general form. The contribution for down-quark final states is given as

$$\langle\sigma v\rangle_{\text{eff}}^d = \frac{1}{18} \cdot \frac{3}{32\pi} \sum_{i,j=1}^3 \sum_{k,l=d,s,b} \frac{|\tilde{\lambda}_{ki}|^2 |\tilde{\lambda}_{lj}|^2 m_\chi^2}{(m_\chi^2 + m_\phi^2)^2}. \quad (9.11)$$

Since the masses of down-, strange- and bottom-quarks are way below the considered DM masses, we neglected them and hence the phase space factor in the formula. In case of SFF, formula (9.11) reduces to

$$\langle\sigma v\rangle_{\text{eff}}^d = \frac{1}{2} \cdot \frac{3}{32\pi} \sum_{k,l=d,s,b} \frac{|\tilde{\lambda}_{k3}|^2 |\tilde{\lambda}_{l3}|^2 m_\chi^2}{(m_\chi^2 + m_\phi^2)^2}. \quad (9.12)$$

The phenomenology stays quite similar to the one observed for the up-quark DMFV model in Chapter 6. The basic consequences for the parameters of λ in both the QDF and the SFF scenario remain unchanged. The significant differences are the following:

- Due to the larger number of final states, at a fixed mediator mass m_ϕ and fixed λ , the relic abundance constraint (6.3) demands a smaller DM mass in this model relative to the up-quark DMFV model. We can observe this in Figure 9.4 compared to Figure 6.2a. Therefore, the same bounds on the maximum coupling strength result in a lower value of the lower DM mass bound.
- Since the top-quark final state is less significant among the increased number of final states, the top mass threshold is of less consequence for the phenomenology.
- Figure 9.5 shows the allowed masses in the $m_\phi - m_{\chi t}$ plane for the SFF scenario. We observe that both the lower and upper DM mass bound has shifted to lower values.

We made the same assumptions and considered the same scenarios, that were discussed for the up-quark DMFV model in Chapter 6.

9.5 Direct Detection Constraint

Finally we need to consider the extra contributions to WIMP-nucleon scattering that arise from the couplings of DM to the down-quark triplet. The overall formula, considering natural xenon as target, is given as:

$$\sigma_{n,\text{nat-Xe}}^{SI} = \sum_{i=1}^9 \rho_i \cdot \frac{\mu_n^2}{\pi A_i^2} |Z(f_p^u + f_p^d) + (A_i - Z)(f_n^u + f_n^d)|^2. \quad (9.13)$$

The respective natural abundances ρ_i of the xenon isotopes with mass number A_i are given in Table 7.1. The contributions to WIMP-nucleon scattering resulting from the coupling

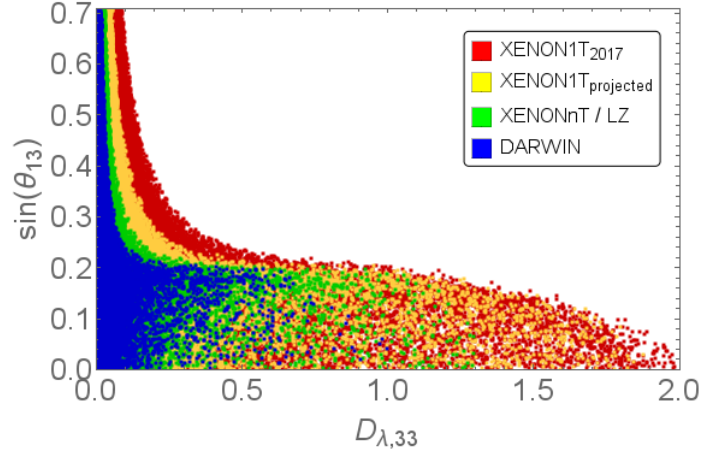


Figure 9.6: Valid areas of parameter space of the quark-doublet DMFV model, for different cross section limits, for DM mass $m_\chi = 250$ GeV and mediator mass $m_\phi = 850$ GeV. The current exclusion bounds of XENON1T [78], as well as the projected bounds of XENON1T [79], XENONnT [79], LUX-ZEPLIN (LZ) [80] and DARWIN [81] have been applied respectively.

of DM to the up-quark triplets f_p^u and f_n^u are presented in Section 7.2. The contributions to WIMP-nucleon scattering that arise from the couplings of the DM candidate to the down-quark triplet are given as:

$$2f_p^{\text{tree,d}} = f_n^{\text{tree,d}} = \frac{|\tilde{\lambda}_{ut}|^2}{4m_\phi^2}, \quad (9.14)$$

$$2f_p^{\text{box,d}} = f_n^{\text{box,d}} = \sum_{i,j} \frac{|\tilde{\lambda}_{ui}|^2 |\tilde{\lambda}_{jt}|^2}{32\pi^2 m_\phi^2} L\left(\frac{m_{q_i}^2}{m_\phi^2}, \frac{m_{\chi_j}^2}{m_\phi^2}\right), \quad (9.15)$$

$$f_p^{\text{photon,d}} = + \sum_i \frac{|\tilde{\lambda}_{it}|^2 e^2}{96\pi^2 m_\phi^2} \left[\frac{3}{2} + \log\left(\frac{m_{q_i}^2}{m_\phi^2}\right) \right]. \quad (9.16)$$

The Z-penguins with a down-quark flavour in the loop are negligible, due to the relatively small masses in the down-quark sector. Due to the opposite sign of the charge of ϕ_d , we find a negative photon-penguin contribution in the down-quark sector. Hence, compared to the up-quark DMFV model, we find an additional negative term, which opens up the possibility for more diverse cancellation patterns.

Figure 9.6 shows the allowed values of the flavour mixing angle θ_{13} in dependence of $D_{\lambda,33}$ for the quark-doublet DMFV model. We show the allowed regions for various strength of the direct detection bounds. The current XENON1T bounds [76], as well as the projected bounds from XENON1T [79], XENONnT [79], LUX-ZEPLIN (LZ) [80] and DARWIN [81] have been applied respectively.

For small coupling $D_{\lambda,33}$ we observe all θ_{13} values to be allowed. This is due to the overall

suppression by the small coupling, as discussed for the up-quark DMFV model. Also similar to the up-quark DMFV model, for larger $D_{\lambda,33}$, an upper bound on the θ_{13} can be observed, since the tree-level diagram has to be suppressed to some degree to allow for a sufficient interference between positive and negative contributions. For the same mediator mass and DM mass, we find the upper bound at a slightly lower value than in the up-quark DMFV model. The reason for this is the additional tree-level contributions from down-quark scattering. Since an average xenon isotope contains more neutrons than protons, the tree-level contribution to DM-xenon scattering from down-quark scattering is larger than the one from up-quark scattering. At the same time, the additional negative contribution from the photon-penguin with down-quark flavours in the loop are smaller in magnitude than the negative Z-penguin with top-quarks in the loop. Hence, the tree-level contributions need to be more suppressed compared to the up-quark DMFV model.

We should also mention that a significant part of the negative photon-penguin contribution does not depend on the flavour mixing angles. This can be understood by looking at the parametrization of λ in (3.10). Neglecting the influence of V_{CKM} , we can see that the sum over $|\tilde{\lambda}_{it}|^2$ in (9.16) would simplify to $D_{\lambda,33}^2$ - if not for the different masses of the down-quark flavours, which are present in the logarithm. Hence, only part of the contribution depends on θ_{ij} . Furthermore, the largest (in magnitude) negative contribution is the one with a down-quark in the loop, since this results in the smallest $\frac{m_{q_i}^2}{m_\phi^2}$ and hence the largest (in magnitude) $\log\left(\frac{m_{q_i}^2}{m_\phi^2}\right)$. This contribution is proportional to $\sin^2 \theta_{13}$. As a consequence, a small θ_{13} suppresses the large positive tree-level contribution, but at the same time decreases (in magnitude) one of the negative contributions.

This shifted balance between positive and negative contributions is also the reason, why we no longer find any range of $D_{\lambda,33}$, in which a lower bound on θ_{13} arises. Even if the tree-level contributions are close to completely suppressed, the increased number of positive contributions can still be large enough to sufficiently cancel the large (in magnitude) negative Z-penguin and the smaller (in magnitude) negative photon-penguin contribution.

In addition, we can see that this changed cancellation pattern allows for larger (compared to the up-quark DMFV model at comparable masses) $D_{\lambda,33}$ values for the more stringent projected bounds. This is favoured by the fact that in this model there is both a negative contribution to the proton-coupling and to the neutron-coupling, which should make it easier to achieve sufficient cancellation for multiple isotopes. Nevertheless, we still observe that more stringent bounds significantly constrain the valid $D_{\lambda,33}$ values.

For completeness, we need to mention that the top-flavoured DM case is still the preferred option in this model. The large negative neutron Z-penguin is the most efficient way to cancel the multitude of positive contributions and hence allows for the largest valid parameter space.

9.6 Combined Analysis

What remains to be done is to conduct a combined analysis. In contrast to the up-quark DMFV model the flavour constraints now provide the most serious limits on the parameter space. Hence, in the analysis we test the parameter sets first against them, before testing against the relic abundance constraint and finally against the direct detection constraint.

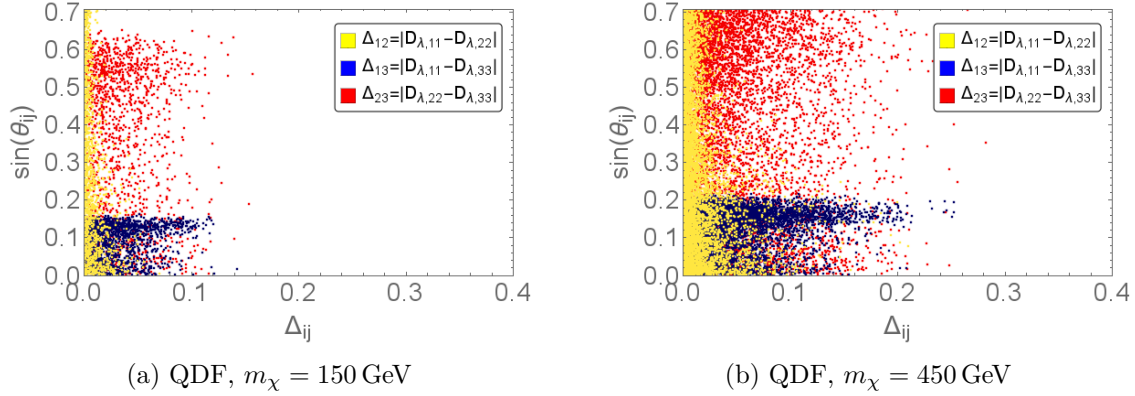


Figure 9.7: Valid regions of parameter space of the quark-doublet DMFV model, with combined flavour, relic abundance and direct detection constraints applied, for QDF scenario and different DM masses, with $m_\phi = 850$ GeV. Different colours correspond to the different mixing angles θ_{ij} and splittings $|D_{\lambda,ii} - D_{\lambda,jj}| = \Delta_{ij}$: $ij = 12$ in yellow, $ij = 13$ in blue, $ij = 23$ in red.

In Figure 9.7, we can see the valid areas in the combined analysis. We observe that the allowed splittings $|D_{\lambda,ii} - D_{\lambda,jj}|$ are extremely limited due to the combination of the strong flavour constraints and the freeze-out scenario splitting conditions. Compared to the splittings allowed by the relic abundance constraint - compare with Figure 9.4 - the allowed values are obviously way more limited due to the combined constraints. The θ_{13} flavour mixing angle is bounded from above, which is the consequence of the combination of relic abundance and direct detection constraints. We observe that for the largest allowed splittings Δ_{13} the mixing angle θ_{13} is required to take values close to the upper bound. The reason for this can be understood from the direct detection constraint. A larger splitting Δ_{13} in QDF with a top-flavoured DM candidate means a smaller $D_{\lambda,11}$ compared to $D_{\lambda,33}$. Hence, the positive box-diagram contributions are smaller compared to the absolute size of the negative Z-penguin. To still allow for a sufficient cancellation, the mixing angle θ_{13} has to be not too small, allowing for a relatively sizeable tree-level and not too large (in magnitude) Z-penguin contribution.

Figure 9.8 shows the valid points in the $m_\phi - m_{\chi_t}$ plane in the QDF scenario for different strengths of the direct detection bounds. We observe that the lower DM mass bounds are not as stringent as in the up-quark DMFV model. The reason for this is mostly the changed relic abundance phenomenology. Due to the larger number of possible final states in the annihilation process, the required DM mass for a fixed mediator mass and fixed coupling λ is smaller than in the up-quark DMFV model. This results in a relaxed lower bound

compared to the up-quark DMFV model.

Furthermore we find that the changed cancellation pattern in the direct detection cross section allows for larger (compared to the up-quark DMFV model) $D_{\lambda,33}$ for the more stringent future bounds. This (in addition to the previously explained relic abundance effect) explains, why the lower DM mass bound from the combined analysis is less stringent (compared to the up-quark DMFV model) for all strengths of direct detection bounds.

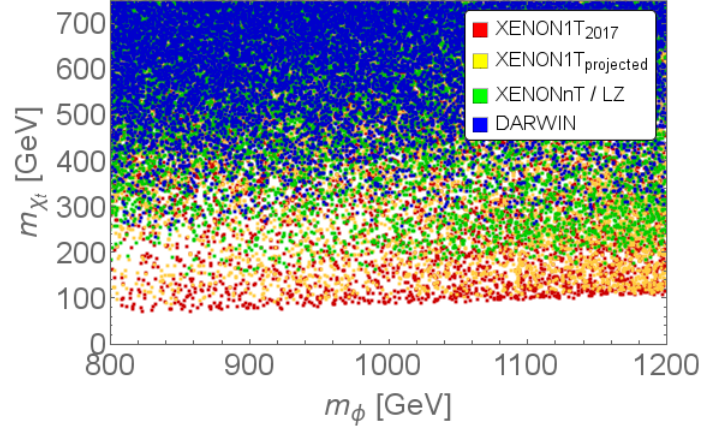


Figure 9.8: Valid area in the $m_\phi - m_{\chi_t}$ plane of the quark-doublet DMFV model with combined flavour, relic abundance and direct detection constraints applied in the QDF scenario. We show the valid area for different strengths of direct detection bounds. The current exclusion bounds of XENON1T [78] as well as the projected bounds of XENON1T [79], XENONnT [79], LUX-ZEPLIN (LZ) [80] and DARWIN [81] are applied respectively. The interference of relic abundance and direct detection effects results in a lower bound on the DM mass, increasing with more stringent direct detection bounds.

We show no valid areas for the SFF scenario, since the combined bounds completely reject this scenario for the quark-doublet model. The reason for this is the more stringent flavour constraints in combination with the direct detection constraints on θ_{13} . To realize the SFF scenario, a sufficiently large splitting between the coupling $D_{\lambda,33}$ and the other couplings is necessary. For a significant splitting between the couplings, the flavour constraints require small flavour mixing angles θ_{13} and θ_{23} . At the same time a large splitting between $D_{\lambda,33}$ and the other couplings results in a relatively small size of the direct detection box-diagram contributions compared to the absolute size of the negative Z-penguin contribution. As discussed before, this requires θ_{13} to be sufficiently large, which then is in conflict with the flavour constraints. To achieve a simultaneous compliance with both constraints, the splitting between $D_{\lambda,33}$ and $D_{\lambda,22} / D_{\lambda,11}$ has to be sufficiently small. By relaxing our upper bound on the magnitude of η we can allow for smaller splittings between the couplings to still realize the SFF scenario. This enables us to still find valid points for the SFF scenario even in the combined analysis. Nevertheless, for $\eta = -0.075$, which we chose as our benchmark in Subsection 6.3.2, the SFF scenario can not be realized for the quark-doublet DMFV model.

Considering the case of charm-flavoured DM, the extreme bounds on the $D_{\lambda,22}-D_{\lambda,11}$ splitting would result in an even stronger rejection of the SFF scenario, demanding even larger η .

9.6.1 Summary of Constraints

To conclude this analysis of the quark-doublet DMFV model, we want to give a summary of all observed constraints from the multitude of data. We focus mainly on the differences compared to the up-quark DMFV model. The following crucial differences have been identified:

- The collider bounds impose considerably stronger constraints, due to both additional production channels as well as the additional decay modes. To avoid constraints for the phenomenologically interesting parameter region, the couplings would have to be more strictly constrained than in the up-quark DMFV model.
- Since the NP particles in the quark-doublet model couple to all quark flavours of both up- and down-sectors, the model is affected by the considerably stronger constraints from meson mixing data from the down-sector in addition to the $D^0 - \bar{D}^0$ mixing data. This results in strong upper bounds on either the splitting between couplings or the related flavour mixing angle. In case of θ_{12} the case is even more serious. Since $D^0 - \bar{D}^0$ mixing bounds and $K^0 - \bar{K}^0$ mixing bounds have to be satisfied simultaneously, the splitting between $D_{\lambda,11}$ and $D_{\lambda,22}$ is strictly bounded from above, with no θ_{12} values valid for larger values.
- Due to the larger number of possible final states in DM annihilation, the required DM mass for fixed mediator mass and fixed coupling λ is lower than in the up-quark DMFV model. This relaxes the lower bound on the DM mass, which originated in the upper bound on the couplings $D_{\lambda,ii}$. In the SFF scenario it also decreases the upper bound on the DM mass.
- The cancellation pattern in the direct detection cross section is more complicated, due to the larger number of relevant scattering processes involved. Among the new processes, we find an additional negative contribution, the photon-penguin with down-quarks in the loop. The more involved cancellation pattern results in an upper bound on the flavour mixing angle θ_{13} for larger $D_{\lambda,33}$. We no longer observe a lower bound on θ_{13} for any $D_{\lambda,33}$.

In a combined analysis, we find the following effects:

- The stronger flavour bounds in combination with the relic abundance and direct detection bounds seriously constrain the splittings between the $D_{\lambda,ii}$.
- The combination of relic abundance and direct detection constraints result in the familiar lower bound on the DM mass in light of future direct detection data. Due to the lower DM masses required by the relic abundance, the lower bound is more relaxed compared to the up-quark DMFV model.
- SFF can not be realized with $\eta = -0.075$ for the quark-doublet DMFV model. This is a consequence of the interplay between the flavour and direct detection bounds.

- The two flavour freeze-out scenario with a top-flavoured DM relic is constrained in the same way as in the up-quark DMFV model. Since this freeze-out scenario would demand a significant splitting between $D_{\lambda,11}$ and $D_{\lambda,22}$ the flavour constraints pose very strong constraints, even more serious than in the up-quark DMFV model.
- Overall the DM mass range is less constrained than in the up-quark DMFV model, even in light of future bounds. Keeping in mind that the lowest valid DM masses demand the largest allowed couplings, we have to conclude that the collider bounds result in the most stringent limits for a large part of the phenomenologically interesting parameter space. LHC run 2 data will push the exclusion bounds even further. In contrast to the up-quark DMFV model, collider constraints prove to be the most efficient way to push exclusion bounds for a significant part of the parameter space of the quark-doublet DMFV model. Nevertheless, the combination of relic abundance and collider constraints still enables us to exclude low DM masses for all mediator masses, which remains an advantage over the collider bounds.

Conclusion and Outlook

To conclude this thesis, we present a short review of the main features and results of the analysis and an outlook on the future of the subject. In the course of this thesis we have studied two simplified models of flavoured dark matter, coupling a dark matter (DM) flavour triplet to the Standard Model (SM) up-quark flavour triplet and to the Standard Model left-handed quark-doublets respectively. The dark matter flavours have been chosen to be Dirac fermions in analogy to the SM flavour triplets. Furthermore, they have been chosen to be SM gauge singlets, to get a truly "dark"—under electroweak and QCD interactions—matter candidate in our model. To get a gauge invariant interaction we have introduced a new scalar doublet of mediators, carrying the QCD colour and hypercharge of the SM quarks. For the first time, we have studied such models in a framework allowing for a generic DM-quark coupling matrix beyond the limitations of Minimal Flavour Violation (MFV). The more general framework of Dark Minimal Flavour Violation (DMFV), which we have followed, had been introduced recently, studying a model of flavoured dark matter (FDM) coupling to the SM down-quark triplet. We have seen that such an interaction results in the lightest new particle being stable. To avoid a stable coloured particle we have demanded the mediator mass to be above the DM masses.

Taking the DM-quark coupling to be a generic 3×3 matrix, we have studied the phenomenology by applying all relevant constraints first separately and then in a combined analysis. We have started by studying the implications of new physics searches at the LHC. Bounds from jets + \cancel{E}_T final state searches have proven to result in the most stringent collider constraints on our model, excluding a significant part of the phenomenologically interesting parameter space. To avoid too stringent bounds on the DM mass, we have identified a safe parameter space for the further analysis. By demanding a sufficiently large mediator mass and an upper bound on the coupling strength, we made sure that collider bounds would not interfere with the further analysis. For the quark-doublet DMFV model the constraints have proven to be significantly stronger than for the up-quark DMFV model. Future bounds from LHC

run 2 data are expected to result in even considerably stronger constraints, excluding larger mediator masses and lower couplings.

Since a generic coupling matrix constitutes a new source of flavour and CP violation, we had to consider exclusion bounds from flavour experiments. Effects from rare decays impose negligible constraints analogously to the results found for the down-quark DMFV model. Bounds from neutral meson mixing data are the relevant source of flavour constraints for the model. For the up-quark DMFV model the $D^0 - \bar{D}^0$ mixing yields the only source of constraints, resulting mainly in an upper bound on the first-second generation flavour mixing angle of the coupling matrix. In contrast, the combined constraints from $D^0 - \bar{D}^0$, $K^0 - \bar{K}^0$ and $B_{d,s}^0 - \bar{B}_{d,s}^0$ mixing data, resulted in a serious upper bound on all flavour mixing angles for the doublet-quark DMFV model. Due to the influence of the CKM-matrix, the latter model is unable to satisfy the $D^0 - \bar{D}^0$ and $K^0 - \bar{K}^0$ for too large splittings in the first and second generation coupling, excluding all large splittings between the first and second generation coupling.

Of course, the cosmologically demanded DM relic abundance poses another constraint on the model. For the course of this study we have assumed the observed dark matter to be a thermal relic. Since the relic abundance constraint requires the DM annihilation cross section to acquire the correct value to reproduce the observed relic abundance, we have found a necessary correlation between the parameters of the model. Depending on the mass-splitting of the DM flavours, several freeze-out scenarios are possible. To understand the phenomenology, we have studied two benchmark freeze-out scenarios, i.e. quasi-degenerate freeze-out (QDF) and single flavour freeze-out (SFF). For fixed values of the mediator mass and coupling matrix, the relic abundance constraint demands a specific value of the DM mass. In case of the quark-doublet DMFV model the required DM mass (for a fixed mediator mass and coupling matrix) has in general been found to be lower than in the up-quark DMFV case, due to the increased number of possible final states. Since the collider constraints impose an upper bound on the couplings, we have observed a corresponding lower bound on the DM mass for both QDF and SFF. For SFF the necessary splitting in the DM masses furthermore results in an additional upper bound on the DM mass. The exact values of these bound depend on the mediator mass. In this analysis, we have focused on the case of top-flavoured DM as the relic, foreclosing the constraints of direct detection bounds. Hence, we have demanded the top-flavour of the DM triplet to acquire the smallest mass.

Finally, we have considered the exclusion bounds from direct detection experiments. The absence of any signal in those experiments is translated to an upper bound on the WIMP-nucleon cross section. We have found that for larger couplings, a cancellation of the different contributions to the scattering amplitude is necessary to fulfill the stringent exclusion bounds. The only negative contribution in the up-quark DMFV model, and the most relevant one in the quark-doublet DMFV model, is the neutron Z-penguin. Since a Z-penguin contribution is only relevant for a top-quark in the loop, this necessary cancellation clearly favours top-flavoured DM, i.e. a DM flavour as relic, which couples primarily to the top-quark. For the choice of top-flavoured DM, the necessary cancellation pattern has been found to result in an upper and—depending on the exact values of the couplings—lower bound on the flavour mixing angle between first and third generation. The exact shape

of this bound depends both on the DM mass and the mediator mass. We have observed that a sufficient cancellation is not possible for too large couplings. Furthermore, we had to consider the presence of multiple stable xenon isotopes. Since the relevant negative contribution originates from the coupling to the neutron, the perfect cancellation pattern is different for different isotopes. Especially in light of future, more stringent bounds on the WIMP-nucleon cross section, a sufficient simultaneous suppression of the scattering cross section for all isotopes is impossible for too large couplings. Hence, we have observed that such more stringent bounds result in a decreasing upper bound on the couplings.

After having studied the effects of all relevant constraints on their own, we have moved on to a combined analysis of flavour, relic abundance and direct detection constraints. We have observed a rich and non-trivial interplay of the multitude of effects. The most relevant discovered effect is the combination of relic abundance and direct detection constraints. Since, for a fixed set of mediator and DM mass, the relic abundance constraint is only fulfilled for a sufficiently large coupling strength, we only find a valid parameter set if the direct detection constraint allows for such a large coupling. Since the direct detection bounds exclude too large couplings, we have found a lower limit on the DM mass (in terms of the mediator mass). This lower bound increases with more stringent bound from future direct detection experiments. Hence, we conclude that such ongoing and scheduled direct detection experiments are well motivated, allowing to probe an increasing part of the phenomenologically interesting parameter space in an efficient way, hence raising the potential for discovery. Furthermore, we have also found the top-flavoured DM case to be favoured in the combined analysis.

To conclude this work, we want to emphasize that the combined analysis is essential for understanding the true exclusion bounds on dark matter models. We have identified valid areas in the parameter space, which are far different from the valid parameter space in the MFV limit. Therefore, going beyond MFV has proven to be well motivated, with DMFV as an excellent guidance. Simplified models of flavoured DM are a powerful tool and will continue to be a fruitful source of insight, helping to guide the physics community in our hunt for the dark matter particle.

Phenomenology of Couplings Beyond 2.0

During the course of the analyses we restricted all couplings by an upper bound $2.0 \geq D_{\lambda,33} \geq D_{\lambda,11}, D_{\lambda,22}$. This was mainly motivated by the jets + \cancel{E}_T final state bound from collider searches. Already for couplings as big as 2.0 a significant part of the phenomenologically interesting parameter space is found to be excluded. In this appendix, we want to further discuss the effects of larger couplings.

Figure A.1 shows exclusion areas from jets + \cancel{E}_T final state searches for several degenerate coupling strengths $D_{\lambda,11} = D_{\lambda,22} = D_{\lambda,33}$ beyond 2.0 in the up-quark DMFV model. As expected, the excluded area strictly increases with increasing $D_{\lambda,11} = D_{\lambda,22} = D_{\lambda,33}$. We conclude that such large couplings exclude too much of the phenomenologically interesting range of DM masses in the case of a mediator masses as low as $m_\phi = 850$ GeV. The limits $2.0 \geq D_{\lambda,33} \geq D_{\lambda,11}, D_{\lambda,22}$ are well justified for a benchmark case to study the impact of other constraints. As discussed in Chapter 9, even stronger bounds are necessary in the quark-doublet DMFV model to be safe from jets + \cancel{E}_T final state bounds in the case of a mediator masses as low as $m_\phi = 850$ GeV.

Apart from the collider constraints, the direct detection constraint also provide a natural upper bound on the couplings. Figure A.2 explicitly demonstrates this bound for the up-quark DMFV model in the QDF scenario with top-flavoured DM candidate. The plot shows valid areas for a scan over the range of coupling values as large as 4.0. The current XENON1T bounds have been applied. We observe that the upper bound on the mixing angle θ_{13} crosses the $\theta_{13} = 0$ line at $D_{\lambda,33} \approx 3.0$, hence excluding any larger couplings. This is a result of the increasing box-diagram contributions, which can no longer be sufficiently cancelled by the negative Z-penguin contribution. A more detailed discussion of this effect can be found in Subsection 7.3.1. We conclude that DD imposes a natural upper bound on the couplings, depending on the DM mass and the mediator mass.

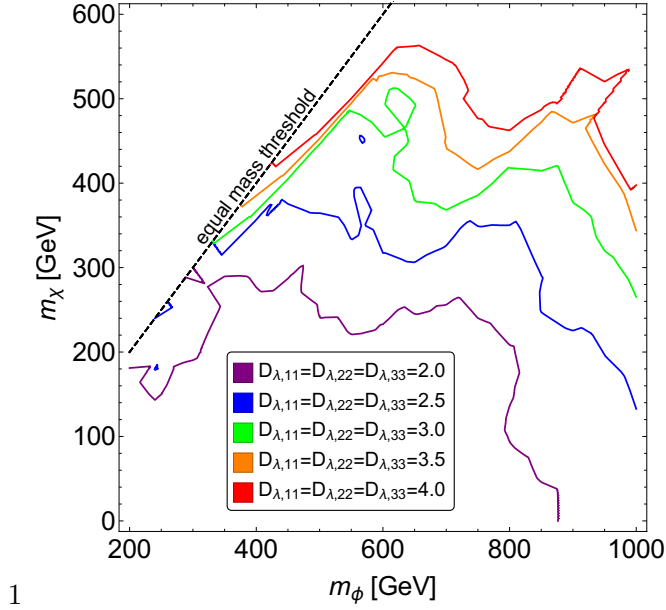


Figure A.1: Constraints on the jets + \cancel{E}_T final state from 8 TeV LHC run 1 data, obtained from bounds in [48]. We observe that the exclusion area strictly grows with increasing $D_{\lambda,11} = D_{\lambda,22} = D_{\lambda,33}$. For couplings $D_{\lambda,11} = D_{\lambda,22} = D_{\lambda,33}$ above 2.0 we observe a significant lower bound on the phenomenologically interesting range of DM masses for all mediator masses. We do not show the exclusion bounds for mediator masses larger than 1 TeV, since in this area numerical uncertainties from extrapolation of the exclusion data dominate.

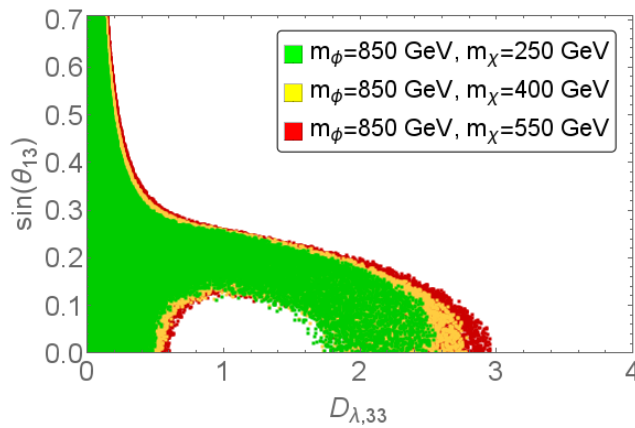


Figure A.2: Valid ranges of flavour mixing angle θ_{13} as function of $D_{\lambda,33}$ at various values of m_χ and fixed m_ϕ (in QDF) with current XENON1T direct detection bounds [78] applied. We observe that we no longer find any valid θ_{13} for too large $D_{\lambda,33}$. Hence, the direct detection bounds result on an upper bound on the couplings.

Phenomenology of Flexible η

In the analyses of both the up-quark DMFV model and the quark-doublet model, we focused on two benchmark freeze-out models—quasi-degenerate freeze-out and single flavour freeze-out. For each model we picked a fixed value of η , $\eta = -0.01$ in the QDF scenario and $\eta = -0.075$ in the SFF scenario. The parameter η depends on the specifics of a complete theory and is hence treated as a free parameter in the simplified models. In this appendix we want to discuss the influence of η on the phenomenology in more detail.

In the case of QDF, the effect of a different value of η is of minor importance. We picked the lowest reasonable absolute value in the benchmark model, therefore allowing the largest possible splittings in the couplings $D_{\lambda,ii}$. A larger (absolute) η would demand smaller splittings in the $D_{\lambda,ii}$, hence further limiting the valid parameter space. Such a lower splitting in the $D_{\lambda,ii}$ is of no interesting consequence in light of any of the constraints. On the contrary, the constraints from flavour experiments will be relaxed. We conclude that for QDF the lowest possible η allows for the largest possible valid parameter space.

In the SFF scenario the value of η is of far greater consequence. As discussed in Subsection 6.3.2, demanding a significant mass-splitting of at least 10% between the lightest DM flavour and the other flavours demands a sizeable splitting in the couplings. This results in a lower bound on $D_{\lambda,33}$ for which the threshold mass-splitting of 10% is realized for vanishing $D_{\lambda,11}, D_{\lambda,22}$. The exact value of this lower $D_{\lambda,33}$ bound depends on the value of η . The larger the absolute value of η , the smaller is the bound. We picked a fixed $\eta = -0.075$ for the benchmark scenario, which would not violate the convergence requirement (3.23) even for the largest allowed couplings in the identified safe parameter space. Nevertheless for smaller couplings, a larger (absolute) value of η , which does not violate the convergence requirement, can be found.

As discussed in Chapter 9, no valid points can be found for the quark-doublet DMFV model in the SFF scenario with $\eta = -0.075$. To understand this better, we conduct a special scan,

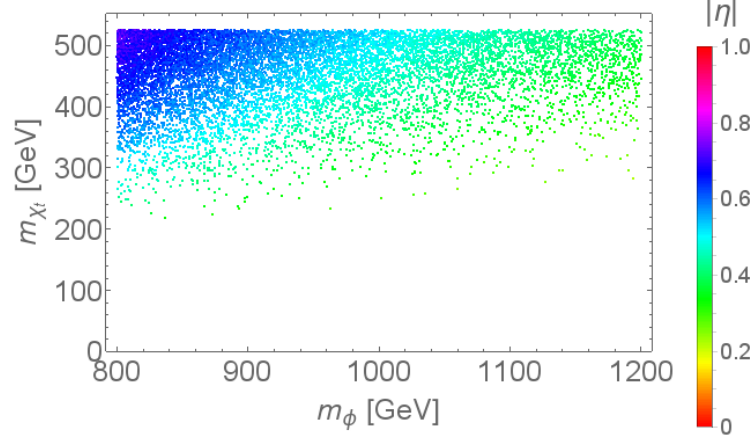


Figure B.1: Valid area in the $m_\phi - m_{\chi_t}$ plane of the quark-doublet DMFV model with combined flavour, relic abundance and direct detection constraints applied in the SFF scenario. We show the valid area for current exclusion bounds of XENON1T [78]. To find valid points in the SFF scenario, we allow η to take the largest (absolute) value which guarantees convergence of the mass corrections in dependence of the coupling $D_{\lambda,33}$. The absolute value $|\eta|$ of the respective valid point is shown in colour-coding.

allowing for a flexible η . After randomizing $D_{\lambda,33}$, we pick the largest absolute value of η which does not violate the convergence requirement (3.23). This then allows for the smallest possible splitting in the couplings. For such smaller splittings the combination of flavour and direction detection constraints can be fulfilled and we find valid areas in the parameter space.

Figure B.1 shows the valid areas in the $m_\phi - m_{\chi_t}$ plane. We observe that we find no longer an upper DM mass bound. This comes as no surprise, since even for the smallest possible $D_{\lambda,33}$ we always find a sufficiently large η which enables the SFF scenario. A pattern in the valid η values in dependence of the masses m_ϕ and m_{χ_t} is apparent. Since we always pick the largest allowed absolute value of η it directly corresponds to a $D_{\lambda,33}$ value. Remembering that the $D_{\lambda,33}$ value is essential in governing the size of the annihilation cross section, the pattern in valid η value in dependence of m_ϕ and m_{χ_t} comes as no surprise.

We observe in Figure B.1 that the minimum absolute value of η for which we find valid points is approximately 0.3. This means the largest valid $D_{\lambda,33}$ is approximately 1.0. Hence, this is the maximum splitting for which the combination of flavour and direct detection constraints on θ_{13} can simultaneously be fulfilled. We have to recall that the flavour constraints give rise to an upper bound on θ_{13} in dependence of the splitting Δ_{13} . At the same time large splittings Δ_{13} and Δ_{12} result in small box diagram contributions compared to the absolute value of the negative Z-penguin contribution to the WIMP-nucleon cross section. Therefore, the mixing angle θ_{13} needs to be sufficiently large to guarantee sufficiently large tree-level contributions which balance the Z-penguin contribution. Hence, for large splittings Δ_{13} and Δ_{12} we find a lower bound on θ_{13} from direct detection constraints. If the lower bound from direct detection constraints is above the upper bound from flavour constraints, no

valid points can be achieved. This is why a sufficiently small $D_{\lambda,33}$ and hence a sufficiently large $|\eta|$ is necessary to realize SFF in the quark-doublet model.

We can see that an understanding of the combined effects of flavour, relic abundance and direct detection constraints is necessary to understand the phenomenology in Figure B.1.

We conclude that a sufficiently large absolute value of η can always enable SFF. Nevertheless, we need to remember that depending on the details of the full theory fixed value of η is realized. For such a fixed value the results found in Subsection 6.3.2 are qualitatively true. Depending on the fixed value it is not guaranteed that SFF can be realized, as we have seen in Chapter 9.

Constraints on Large Masses

In our analysis we focused on the phenomenologically interesting DM mass range of $\mathcal{O}(10 \text{ GeV}-1 \text{ TeV})$. We studied associated mediator masses in the TeV range. To complete the analysis, we want to discuss possible extensions to larger masses both of the mediator and the DM particle. We observe that, as a result of the relic abundance constraint, a natural upper bound on the masses of the model exists, see Figure C.1.

To understand this, note that the couplings have to be constraint by some upper bound, to guarantee perturbativity of the model. At the same time, the DM mass may not exceed the mediator mass to avoid a stable coloured scalar. The annihilation cross section is approximately proportional to $\sigma \sim \lambda^4 \cdot \frac{m_\chi^2}{m_\phi^4}$, where λ is an estimate of the average coupling strength. In the threshold case of $m_\chi \approx m_\phi$ we then find $\sigma \sim \frac{\lambda^4}{m_\phi^2}$. From this, it is easy to see that the relic abundance constraint in combination with an upper bound on the coupling strength λ results in an upper bound on the mediator mass.

To get a feeling for the scale of this resulting bound, Figure C.1 shows the entire allowed parameter space of the up-quark DMFV model in the $m_\phi - m_{\chi_t}$ plane for the case of our usual bound $2.0 \geq D_{\lambda,33} \geq D_{\lambda,11}, D_{\lambda,22}$ on the couplings, with combined constraints applied. We observe that the mediator and hence DM mass is confined to a range below approximately 6 TeV. The current combined constraints probe the phenomenologically interesting part of the parameter space in the lower left corner of the plot.

We conclude that even though a large mediator mass naturally suppresses all NP contributions and hence relaxes the constraints from direct detection, flavour and collider bounds, the relic abundance constraint can not be fulfilled for an arbitrarily large mediator mass. This results in a natural limitation of the valid mass ranges in our model. Since this limitation constraint originates from the lower bound on the annihilation cross section, we can not relax it by assuming our DM candidate makes up for only part of the observed DM

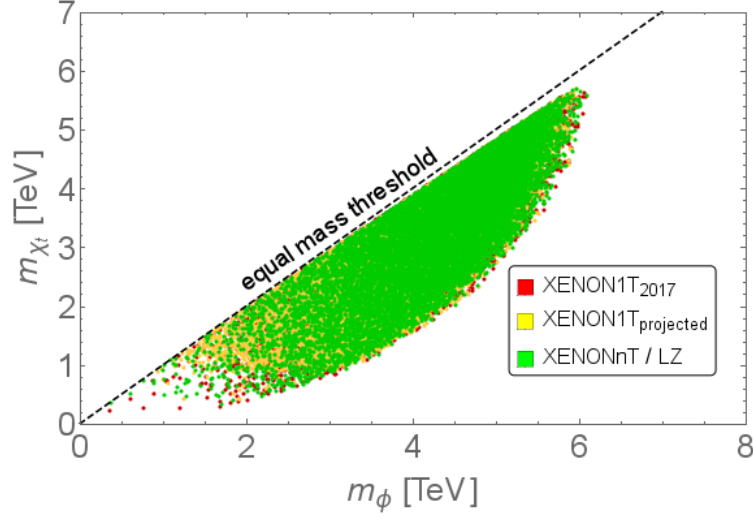


Figure C.1: Entire allowed parameter space of the up-quark DMFV model in the m_{ϕ} - m_{χ_t} plane in the QDF scenario with the usual “safe parameter space” constraints $2.0 \geq D_{\lambda,33} \geq D_{\lambda,11}, D_{\lambda,22}$ and combined flavour, relic abundance and direct detection constraints applied. The current exclusion bounds of XENON1T [78] as well as the projected bounds of XENON1T [79], XENONnT [79] and LUX-ZEPLIN (LZ) [80] are applied respectively. We observe upper bounds on the masses as a result of the relic abundance constraint. Please note that the deviation of valid points from the equal mass threshold for larger masses originates from the DM mass corrections. In our scan we demand $m_{\chi} < m_{\phi}$ but in the plot we show the corrected mass value m_{χ_t} .

relic, which would allow for a larger annihilation cross section.

Bibliography

- [1] P. Gorenstein and W. Tucker, “Astronomical Signatures of Dark Matter,” *Adv. High Energy Phys.* **2014** (2014) 878203.
- [2] G. B. Gelmini, “The Hunt for Dark Matter,” in *Proceedings, Theoretical Advanced Study Institute in Elementary Particle Physics: Journeys Through the Precision Frontier: Amplitudes for Colliders (TASI 2014): Boulder, Colorado, June 2-27, 2014*, pp. 559–616. 2015. arXiv:1502.01320 [hep-ph].
<http://inspirehep.net/record/1342951/files/arXiv:1502.01320.pdf>.
- [3] K. Garrett and G. Duda, “Dark Matter: A Primer,” *Adv. Astron.* **2011** (2011) 968283, arXiv:1006.2483 [hep-ph].
- [4] F. Zwicky, “Die Rotverschiebung von extragalaktischen Nebeln,” *Helv. Phys. Acta* **6** (1933) 110–127. [Gen. Rel. Grav.41,207(2009)].
- [5] V. C. Rubin and W. K. Ford, Jr., “Rotation of the Andromeda Nebula from a Spectroscopic Survey of Emission Regions,” *Astrophys. J.* **159** (1970) 379–403.
- [6] V. C. Rubin, N. Thonnard, and W. K. Ford, Jr., “Rotational properties of 21 SC galaxies with a large range of luminosities and radii, from NGC 4605 /R = 4kpc/ to UGC 2885 /R = 122 kpc/,” *Astrophys. J.* **238** (1980) 471.
- [7] D. Clowe, A. Gonzalez, and M. Markevitch, “Weak lensing mass reconstruction of the interacting cluster 1E0657-558: Direct evidence for the existence of dark matter,” *Astrophys. J.* **604** (2004) 596–603, arXiv:astro-ph/0312273 [astro-ph].
- [8] S. D. M. White and M. J. Rees, “Core condensation in heavy halos: A Two stage theory for galaxy formation and clusters,” *Mon. Not. Roy. Astron. Soc.* **183** (1978) 341–358.
- [9] **Planck** Collaboration, P. A. R. Ade *et al.*, “Planck 2015 results. XIII. Cosmological parameters,” arXiv:1502.01589 [astro-ph.CO].
- [10] G. Bertone, D. Hooper, and J. Silk, “Particle dark matter: Evidence, candidates and constraints,” *Phys. Rept.* **405** (2005) 279–390, arXiv:hep-ph/0404175 [hep-ph].
- [11] C. Kilic, M. D. Klimek, and J.-H. Yu, “Signatures of Top Flavored Dark Matter,” *Phys.Rev.* **D91** no. 5, (2015) 054036, arXiv:1501.02202 [hep-ph].

-
- [12] P. Agrawal, S. Blanchet, Z. Chacko, and C. Kilic, “Flavored Dark Matter, and Its Implications for Direct Detection and Colliders,” *Phys. Rev.* **D86** (2012) 055002, [arXiv:1109.3516 \[hep-ph\]](#).
- [13] K. Cheung, K. Mawatari, E. Senaha, P. Y. Tseng, and T. C. Yuan, “Top window for dark matter,” *Int. J. Mod. Phys.* **D20** (2011) 1413–1421.
- [14] J. Kile and A. Soni, “Flavored Dark Matter in Direct Detection Experiments and at LHC,” *Phys. Rev.* **D84** (2011) 035016, [arXiv:1104.5239 \[hep-ph\]](#).
- [15] B. Batell, J. Pradler, and M. Spannowsky, “Dark Matter from Minimal Flavor Violation,” *JHEP* **08** (2011) 038, [arXiv:1105.1781 \[hep-ph\]](#).
- [16] J. F. Kamenik and J. Zupan, “Discovering Dark Matter Through Flavor Violation at the LHC,” *Phys. Rev.* **D84** (2011) 111502, [arXiv:1107.0623 \[hep-ph\]](#).
- [17] A. Kumar and S. Tulin, “Top-flavored dark matter and the forward-backward asymmetry,” *Phys. Rev.* **D87** no. 9, (2013) 095006, [arXiv:1303.0332 \[hep-ph\]](#).
- [18] S. Chang, R. Edezhath, J. Hutchinson, and M. Luty, “Effective WIMPs,” *Phys. Rev.* **D89** no. 1, (2014) 015011, [arXiv:1307.8120 \[hep-ph\]](#).
- [19] J. Kile, “Flavored Dark Matter: A Review,” *Mod. Phys. Lett.* **A28** (2013) 1330031, [arXiv:1308.0584 \[hep-ph\]](#).
- [20] Y. Bai and J. Berger, “Fermion Portal Dark Matter,” *JHEP* **11** (2013) 171, [arXiv:1308.0612 \[hep-ph\]](#).
- [21] B. Batell, T. Lin, and L.-T. Wang, “Flavored Dark Matter and R-Parity Violation,” *JHEP* **01** (2014) 075, [arXiv:1309.4462 \[hep-ph\]](#).
- [22] P. Agrawal, Z. Chacko, and C. B. Verhaaren, “Leptophilic Dark Matter and the Anomalous Magnetic Moment of the Muon,” *JHEP* **08** (2014) 147, [arXiv:1402.7369 \[hep-ph\]](#).
- [23] P. Agrawal, B. Batell, D. Hooper, and T. Lin, “Flavored Dark Matter and the Galactic Center Gamma-Ray Excess,” *Phys. Rev.* **D90** no. 6, (2014) 063512, [arXiv:1404.1373 \[hep-ph\]](#).
- [24] M. A. Gomez, C. B. Jackson, and G. Shaughnessy, “Dark Matter on Top,” *JCAP* **1412** no. 12, (2014) 025, [arXiv:1404.1918 \[hep-ph\]](#).
- [25] P. Agrawal, M. Blanke, and K. Gemmler, “Flavored dark matter beyond Minimal Flavor Violation,” *JHEP* **1410** (2014) 72, [arXiv:1405.6709 \[hep-ph\]](#).
- [26] A. Hamze, C. Kilic, J. Koeller, C. Trenafileva, and J.-H. Yu, “Lepton-Flavored Asymmetric Dark Matter and Interference in Direct Detection,” *Phys. Rev.* **D91** no. 3, (2015) 035009, [arXiv:1410.3030 \[hep-ph\]](#).
- [27] C.-J. Lee and J. Tandean, “Lepton-Flavored Scalar Dark Matter with Minimal Flavor Violation,” *JHEP* **04** (2015) 174, [arXiv:1410.6803 \[hep-ph\]](#).

-
- [28] J. Kile, A. Kobach, and A. Soni, “Lepton-Flavored Dark Matter,” *Phys. Lett.* **B744** (2015) 330–338, [arXiv:1411.1407](#) [hep-ph].
- [29] P. Agrawal, Z. Chacko, E. C. F. S. Fortes, and C. Kilic, “Skew-Flavored Dark Matter,” *Phys. Rev.* **D93** no. 10, (2016) 103510, [arXiv:1511.06293](#) [hep-ph].
- [30] L. Lopez-Honorez and L. Merlo, “Dark matter within the minimal flavour violation ansatz,” *Phys. Lett.* **B722** (2013) 135–143, [arXiv:1303.1087](#) [hep-ph].
- [31] A. J. Buras, P. Gambino, M. Gorbahn, S. Jager, and L. Silvestrini, “Universal unitarity triangle and physics beyond the standard model,” *Phys. Lett.* **B500** (2001) 161–167, [arXiv:hep-ph/0007085](#) [hep-ph].
- [32] G. D’Ambrosio, G. F. Giudice, G. Isidori, and A. Strumia, “Minimal flavor violation: An Effective field theory approach,” *Nucl. Phys.* **B645** (2002) 155–187, [arXiv:hep-ph/0207036](#) [hep-ph].
- [33] A. J. Buras, “Minimal flavor violation,” *Acta Phys. Polon.* **B34** (2003) 5615–5668, [arXiv:hep-ph/0310208](#) [hep-ph].
- [34] M.-C. Chen, J. Huang, and V. Takhistov, “Beyond Minimal Lepton Flavored Dark Matter,” *JHEP* **02** (2016) 060, [arXiv:1510.04694](#) [hep-ph].
- [35] M. Blanke and S. Kast, “Top-Flavoured Dark Matter in Dark Minimal Flavour Violation,” *JHEP* **05** (2017) 162, [arXiv:1702.08457](#) [hep-ph].
- [36] M. Blanke, S. Das, and S. Kast, “Flavoured Dark Matter Turning Left,” - in preparation.
- [37] J. H. Christenson, J. W. Cronin, V. L. Fitch, and R. Turlay, “Evidence for the 2π Decay of the K_2^0 Meson,” *Phys. Rev. Lett.* **13** (1964) 138–140.
- [38] M. Kobayashi and T. Maskawa, “CP Violation in the Renormalizable Theory of Weak Interaction,” *Prog. Theor. Phys.* **49** (1973) 652–657.
- [39] **Particle Data Group** Collaboration, T. Gershon and Y. Nir, “CP VIOLATION IN THE QUARK SECTOR in Review of Particle Physics,” *Chin. Phys.* **C40** no. 10, (2016) 100001.
- [40] S. L. Glashow, J. Iliopoulos, and L. Maiani, “Weak Interactions with Lepton-Hadron Symmetry,” *Phys. Rev.* **D2** (1970) 1285–1292.
- [41] A. J. Buras, “Weak Hamiltonian, CP violation and rare decays,” in *Probing the standard model of particle interactions. Proceedings, Summer School in Theoretical Physics, NATO Advanced Study Institute, 68th session, Les Houches, France, July 28-September 5, 1997. Pt. 1, 2*, pp. 281–539. 1998. [arXiv:hep-ph/9806471](#) [hep-ph].
- [42] **Particle Data Group** Collaboration, C. Patrignani *et al.*, “Review of Particle Physics,” *Chin. Phys.* **C40** no. 10, (2016) 100001.

- [43] M. Blanke, A. J. Buras, A. Poschenrieder, S. Recksiegel, C. Tarantino, S. Uhlig, and A. Weiler, “Another look at the flavour structure of the littlest Higgs model with T-parity,” *Phys. Lett.* **B646** (2007) 253–257, [arXiv:hep-ph/0609284](#) [hep-ph].
- [44] W. R. Inc., “Mathematica, Version 11.2.” Champaign, IL, 2017.
- [45] J. Alwall, R. Frederix, S. Frixione, V. Hirschi, F. Maltoni, O. Mattelaer, H. S. Shao, T. Stelzer, P. Torrielli, and M. Zaro, “The automated computation of tree-level and next-to-leading order differential cross sections, and their matching to parton shower simulations,” *JHEP* **07** (2014) 079, [arXiv:1405.0301](#) [hep-ph].
- [46] M. Papucci, A. Vichi, and K. M. Zurek, “Monojet versus the rest of the world I: t-channel models,” *JHEP* **11** (2014) 024, [arXiv:1402.2285](#) [hep-ph].
- [47] **ATLAS** Collaboration, G. Aad *et al.*, “Search for top squark pair production in final states with one isolated lepton, jets, and missing transverse momentum in $\sqrt{s}=8$ TeV pp collisions with the ATLAS detector,” *JHEP* **11** (2014) 118, [arXiv:1407.0583](#) [hep-ex].
- [48] **ATLAS** Collaboration, G. Aad *et al.*, “Search for squarks and gluinos with the ATLAS detector in final states with jets and missing transverse momentum using $\sqrt{s}=8$ TeV proton–proton collision data,” *JHEP* **09** (2014) 176, [arXiv:1405.7875](#) [hep-ex].
- [49] T. Hurth and W. Porod, “Flavour violating squark and gluino decays,” *JHEP* **08** (2009) 087, [arXiv:0904.4574](#) [hep-ph].
- [50] M. Blanke, G. F. Giudice, P. Paradisi, G. Perez, and J. Zupan, “Flavoured Naturalness,” *JHEP* **06** (2013) 022, [arXiv:1302.7232](#) [hep-ph].
- [51] P. Agrawal and C. Frugiuele, “Mixing stops at the LHC,” *JHEP* **01** (2014) 115, [arXiv:1304.3068](#) [hep-ph].
- [52] M. Arana-Catania, S. Heinemeyer, and M. J. Herrero, “Updated Constraints on General Squark Flavor Mixing,” *Phys. Rev.* **D90** no. 7, (2014) 075003, [arXiv:1405.6960](#) [hep-ph].
- [53] M. Backović, A. Mariotti, and M. Spannowsky, “Signs of Tops from Highly Mixed Stops,” *JHEP* **06** (2015) 122, [arXiv:1504.00927](#) [hep-ph].
- [54] M. Blanke, B. Fuks, I. Galon, and G. Perez, “Gluino Meets Flavored Naturalness,” *JHEP* **04** (2016) 044, [arXiv:1512.03813](#) [hep-ph].
- [55] A. Alloul, N. D. Christensen, C. Degrande, C. Duhr, and B. Fuks, “FeynRules 2.0 - A complete toolbox for tree-level phenomenology,” *Comput. Phys. Commun.* **185** (2014) 2250–2300, [arXiv:1310.1921](#) [hep-ph].
- [56] Y. Amhis *et al.*, “Averages of b -hadron, c -hadron, and τ -lepton properties as of summer 2016,” [arXiv:1612.07233](#) [hep-ex].

- [57] M. E. Peskin and D. V. Schroeder, *An Introduction to quantum field theory*. Addison-Wesley, Reading, USA, 1995.
<http://www.slac.stanford.edu/~mpeskin/QFT.html>.
- [58] A. J. Buras, S. Jäger, and J. Urban, “Master formulae for $\Delta F = 2$ NLO QCD factors in the standard model and beyond,” *Nucl. Phys.* **B605** (2001) 600–624, [arXiv:hep-ph/0102316](https://arxiv.org/abs/hep-ph/0102316) [hep-ph].
- [59] S. Aoki, Y. Aoki, C. Bernard, T. Blum, G. Colangelo, *et al.*, “Review of lattice results concerning low-energy particle physics,” *Eur.Phys.J.* **C74** (2014) 2890, [arXiv:1310.8555](https://arxiv.org/abs/1310.8555) [hep-lat].
- [60] N. Carrasco, M. Ciuchini, P. Dimopoulos, R. Frezzotti, V. Gimenez, *et al.*, “ $D^0-\bar{D}^0$ mixing in the standard model and beyond from $N_f = 2$ twisted mass QCD,” *Phys.Rev.* **D90** no. 1, (2014) 014502, [arXiv:1403.7302](https://arxiv.org/abs/1403.7302) [hep-lat].
- [61] **LHCb** Collaboration, R. Aaij *et al.*, “Precision measurement of D meson mass differences,” *JHEP* **1306** (2013) 065, [arXiv:1304.6865](https://arxiv.org/abs/1304.6865) [hep-ex].
- [62] A. A. Petrov, “Long-distance effects in charm mixing,” [arXiv:1312.5304](https://arxiv.org/abs/1312.5304) [hep-ph].
- [63] **Belle-II** Collaboration, T. Abe *et al.*, “Belle II Technical Design Report,” [arXiv:1011.0352](https://arxiv.org/abs/1011.0352) [physics.ins-det].
- [64] G. Steigman, B. Dasgupta, and J. F. Beacom, “Precise Relic WIMP Abundance and its Impact on Searches for Dark Matter Annihilation,” *Phys.Rev.* **D86** (2012) 023506, [arXiv:1204.3622](https://arxiv.org/abs/1204.3622) [hep-ph].
- [65] J. D. Wells, “Annihilation cross-sections for relic densities in the low velocity limit,” [arXiv:hep-ph/9404219](https://arxiv.org/abs/hep-ph/9404219) [hep-ph].
- [66] K. Griest and D. Seckel, “Three exceptions in the calculation of relic abundances,” *Phys. Rev.* **D43** (1991) 3191–3203.
- [67] G. Servant and T. M. P. Tait, “Is the lightest Kaluza-Klein particle a viable dark matter candidate?,” *Nucl. Phys.* **B650** (2003) 391–419, [arXiv:hep-ph/0206071](https://arxiv.org/abs/hep-ph/0206071) [hep-ph].
- [68] P. Agrawal, *Flavored Dark Matter*. PhD thesis, Maryland U., 2012.
<http://drum.lib.umd.edu/handle/1903/13235>.
- [69] **AMS** Collaboration, M. Aguilar *et al.*, “Antiproton Flux, Antiproton-to-Proton Flux Ratio, and Properties of Elementary Particle Fluxes in Primary Cosmic Rays Measured with the Alpha Magnetic Spectrometer on the International Space Station,” *Phys. Rev. Lett.* **117** no. 9, (2016) 091103.
- [70] A. Cuoco, M. Krämer, and M. Korsmeier, “Novel dark matter constraints from antiprotons in the light of AMS-02,” [arXiv:1610.03071](https://arxiv.org/abs/1610.03071) [astro-ph.HE].

- [71] M.-Y. Cui, Q. Yuan, Y.-L. S. Tsai, and Y.-Z. Fan, “A possible dark matter annihilation signal in the AMS-02 antiproton data,” [arXiv:1610.03840](#) [[astro-ph.HE](#)].
- [72] J. D. Lewin and P. F. Smith, “Review of mathematics, numerical factors, and corrections for dark matter experiments based on elastic nuclear recoil,” *Astropart. Phys.* **6** (1996) 87–112.
- [73] J. Hisano, K. Ishiwata, and N. Nagata, “Gluon contribution to the dark matter direct detection,” *Phys. Rev.* **D82** (2010) 115007, [arXiv:1007.2601](#) [[hep-ph](#)].
- [74] F. D’Eramo and M. Procura, “Connecting Dark Matter UV Complete Models to Direct Detection Rates via Effective Field Theory,” *JHEP* **04** (2015) 054, [arXiv:1411.3342](#) [[hep-ph](#)].
- [75] T. Jubb, M. Kirk, and A. Lenz, “Charming Dark Matter,” [arXiv:1709.01930](#) [[hep-ph](#)].
- [76] D. S. Akerib *et al.*, “Results from a search for dark matter in the complete LUX exposure,” [arXiv:1608.07648](#) [[astro-ph.CO](#)].
- [77] **PandaX-II** Collaboration, A. Tan *et al.*, “Dark Matter Results from First 98.7 Days of Data from the PandaX-II Experiment,” *Phys. Rev. Lett.* **117** no. 12, (2016) 121303, [arXiv:1607.07400](#) [[hep-ex](#)].
- [78] **XENON** Collaboration, E. Aprile *et al.*, “First Dark Matter Search Results from the XENON1T Experiment,” [arXiv:1705.06655](#) [[astro-ph.CO](#)].
- [79] **XENON** Collaboration, S. Diglio, “XENON1T: the start of a new era in the search for Dark Matter,” *PoS DSU2015* (2016) 032.
- [80] **LZ** Collaboration, D. S. Akerib *et al.*, “LUX-ZEPLIN (LZ) Conceptual Design Report,” [arXiv:1509.02910](#) [[physics.ins-det](#)].
- [81] **DARWIN** Collaboration, J. Aalbers *et al.*, “DARWIN: towards the ultimate dark matter detector,” *JCAP* **1611** no. 11, (2016) 017, [arXiv:1606.07001](#) [[astro-ph.IM](#)].
- [82] J. L. Feng, J. Kumar, and D. Sanford, “Xenophobic Dark Matter,” *Phys. Rev.* **D88** no. 1, (2013) 015021, [arXiv:1306.2315](#) [[hep-ph](#)].
- [83] J. Schieck *et al.*, “Direct Dark Matter Search with the CRESST II Experiment,” *PoS ICHEP2016* (2016) 217, [arXiv:1611.02113](#) [[astro-ph.CO](#)].
- [84] **EDELWEISS** Collaboration, V. Kozlov, “Direct Dark Matter Search With Edelweiss-III: Recent Results and Future Prospects,” in *Proceedings, 17th Lomonosov Conference on Elementary Particle Physics: Moscow, Russia, August 20-26, 2015*, pp. 340–344. 2017.

-
- [85] **PICO** Collaboration, C. Amole *et al.*, “Dark Matter Search Results from the PICO-60 C₃F₈ Bubble Chamber,” *Phys. Rev. Lett.* **118** no. 25, (2017) 251301, [arXiv:1702.07666](#) [[astro-ph.CO](#)].
- [86] **UTfit** Collaboration, M. Bona, “Unitarity Triangle analysis beyond the Standard Model from UTfit,” *PoS ICHEP2016* (2016) 149.
- [87] **UTfit** Collaboration, M. Bona *et al.*, “The UTfit collaboration report on the status of the unitarity triangle beyond the standard model. I. Model-independent analysis and minimal flavor violation,” *JHEP* **03** (2006) 080, [arXiv:hep-ph/0509219](#) [[hep-ph](#)].
- [88] **UTfit** Collaboration, M. Bona *et al.*, “Model-independent constraints on $\Delta F = 2$ operators and the scale of new physics,” *JHEP* **03** (2008) 049, [arXiv:0707.0636](#) [[hep-ph](#)].
- [89] A. J. Buras, F. De Fazio, and J. Girrbach, “331 models facing new $b \rightarrow s\mu^+\mu^-$ data,” *JHEP* **02** (2014) 112, [arXiv:1311.6729](#) [[hep-ph](#)].